NASA TECHNICAL NOTE

NASA TN D-7398

NASA TN D-7398

EXPERIMENTAL STUDY OF SHARP- AND BLUNT-NOSE STREAMWISE CORNERS AT MACH 20

by Ralph D. Watson

Langley Research Center
Hampton, Va. 23665

NATIONAL AERONAUTICS AND SPACE ADMINISTRATION • WASHINGTON, D. C. • APRIL 1974

For sale by the National Technical Information Service, Springfield, Virginia 22151

1. Report No.	2. Government Accession No.	3. Recipient's Catalog No.
NASA TN D-7398		

4. Title and Subtitle	5. Report Date
EXPERIMENTAL STUDY OF SHARP- AND BLUNT-NOSE STREAMWISE CORNERS AT MACH 20	April 1974
	6. Performing Organization Code

7. Author(s)	8. Performing Organization Report No.
Ralph D. Watson	L-8830
	10. Work Unit No.
9. Performing Organization Name and Address	501-06-08-01
NASA Langley Research Center Hampton, Va. 23665	11. Contract or Grant No.
	13. Type of Report and Period Covered
12. Sponsoring Agency Name and Address	Technical Note
National Aeronautics and Space Administration Washington, D.C. 20546	14. Sponsoring Agency Code

15. Supplementary Notes

16. Abstract

Extensive heat-transfer and pressure-distribution data and oil-flow studies on sharp- and blunt-nose streamwise corners at Mach 20 in helium are presented. The far-corner boundary layers on the wedge surfaces forming the corners are laminar for most test conditions. Analysis of the data indicates that the corner flow-field geometry can be described in terms of the inviscid shock pattern on the two-dimensional surfaces forming the corner. Parameters used to correlate blunt shock growth can be used to correlate features of the flow field observed in oil-flow photographs in addition to the measured pressure and heat-transfer distributions on the models. The flow-field structure is described from available experimental data. Regions of the flow in which the structure still is not known are discussed and the need for further research on unsymmetrical corners is emphasized.

17. Key Words (Suggested by Author(s))	18. Distribution Statement
Hypersonic flow Corner flow Shock—boundary-layer interaction	Unclassified – Unlimited STAR Category 12

19. Security Classif. (of this report)	20. Security Classif. (of this page)	21. No. of Pages	22. Price
Unclassified	Unclassified	77	$4.00

Page Intentionally Left Blank

EXPERIMENTAL STUDY OF SHARP- AND BLUNT-NOSE STREAMWISE CORNERS AT MACH 20

By Ralph D. Watson
Langley Research Center

SUMMARY

Extensive heat-transfer and pressure-distribution data and oil-flow studies on sharp- and blunt-nose streamwise corners at Mach 20 in helium are presented. The far-corner boundary layers on the wedge surfaces forming the corners are laminar for most test conditions. Analysis of the data indicates that the corner flow-field geometry can be described in terms of the inviscid shock pattern on the two-dimensional surfaces forming the corner. Parameters used to correlate blunt shock growth can be used to correlate features of the flow field observed in oil-flow photographs in addition to the measured pressure and heat-transfer distributions on the models. The flow-field structure is described from available experimental data. Regions of the flow in which the structure still is not known are discussed and the need for further research on unsymmetrical corners is emphasized.

INTRODUCTION

Interactions, both viscous and inviscid, within the flow field of a vehicle in supersonic flight affect its aerodynamic characteristics and heating load. Efficient vehicle design requires a knowledge of different types of flow patterns which may be encountered and the basic features characteristic of each type. One such interaction flow field is produced when two surfaces intersect in a streamwise direction to form a longitudinal corner. This geometry is known to produce peaks in heating near the corner caused by vortices, or a system of vortices, approximately parallel to the corner. It is, of course, desirable to minimize these heating peaks, and in view of the success which has been obtained in alleviating lee-side heating on delta wings (ref. 1), it is assumed that a reduction in corner heating can be achieved when the factors controlling vortex development are better understood.

Theoretical predictions of the flow field are very limited at present. One method described in reference 2 calculates the complete flow field from the body to the free stream through the use of equations encompassing the whole viscous-inviscid region. The limitations to this method are the large computer storage and long calculation times required. Calculations by this method are presented in reference 3; unfortunately, no solutions are obtained for values of the hypersonic viscous interaction parameter $\overline{\chi}$ greater than 30, and the experimental details of the flow field found at $\overline{\chi} = 5$ are not predicted.

The corner flow field in most cases is dominated by the shock structure caused by the intersection of shocks from the surfaces forming the corner. For sharp-nose "symmetrical" corners, that is, corners composed of wedges with equal angle to the flow, the wedge shocks may or may not intersect at a bisector plane of the configuration. Calculations presented in reference 4 show the limiting conditions for which intersection is possible. Appendix A of this report presents more complete results along with the details of the calculation procedure.

When the shocks cannot intersect, the two-shock method described in reference 5 has been extended in reference 6 to determine the location of a corner or fillet shock as well as the extent of an internal shock within the flow field. Since the major peak in surface heating lies beneath the internal shock, this method is useful in predicting peak-heating location as well as shock location.

In contrast to the theoretical work on the overall shock structure of the corner flow field, solution to the problem of the boundary layer in a corner has received considerably more attention. A solution for incompressible flow can be found in reference 7; for compressible flow, in reference 8.

The structure of the internal flow field determined from detailed pitot surveys has been measured only on symmetrical configurations. Intuitively, the same flow-field details will be found in unsymmetrical corners; however, important parameters such as the pressure level in the corner and the extent of lateral disturbances away from the corner cannot be extrapolated from symmetrical-corner results. Further discussion of the previous experimental studies of the corner flow problem is given in the "Description of the Flow Field" section in the present report.

The present study is a continuation of reference 4, which considered the flow over corners formed by sharp-nose wedges intersecting symmetrically at 90°. Noses of various drag coefficients and thicknesses were added to the basic models of reference 4 to determine whether bluntness effects on simple symmetrical corners could be analyzed. Data of reference 4, tabulated and plotted in more general parameters than in the conical coordinates originally used, are included in this report.

SYMBOLS

A,B	parameters defined in equation (1)
C	Chapman-Rubesin constant
C_D	nose-drag coefficient

c_p	specific heat at constant pressure
G	parameter describing displacement-thickness growth in compressible flow (see eq. (2))
$\overline{G}$	parameter in equation (4)
h	film coefficient of heat transfer
M	Mach number
p	pressure
q	heat-transfer rate
R	Reynolds number
r	nose thickness defined in figure 1(c)
T	temperature
T_{aw}	adiabatic wall temperature
t	nose thickness (see fig. 1)
u	velocity
x,y,z	Cartesian coordinates
y_I	coordinate of point where internal shock intersects model surface (see fig. 12)
y_s	coordinate of wedge-shock location
α	wedge angle or symmetrical corner model angle (see fig. 1)
β	effective nose angle (see fig. 1)

γ ratio of specific heats

ϵ physical nose angle (see fig. 1)

ρ density

ϕ intersection angle of wedges forming the corner (see fig. 1)

$\overline{\chi}$ hypersonic viscous interaction parameter, $\frac{M_\infty{}^3\sqrt{C'}}{\sqrt{R_{\infty,x}}}$

Subscripts:

e conditions at the same x-location undisturbed by corner interference effects

t total condition

w wall condition

x based on x-location

∞ free-stream conditions

Primes denote values at reference temperature.

MODEL DESCRIPTION AND TEST TECHNIQUES

The data of this report were measured on the model shown in figure 1. The horizontal wedge surface consisted of a sharp-leading-edge steel plate mounted on a pivot near the nose so that it could be set at desired angles to the flow. Corners composed of two wedges of equal angle intersecting at 90° were formed by constructing three different vertical sections for mounting on the lower wedge surface. The horizontal surface contained 37 pressure orifices 0.15 cm in diameter. The vertical steel wedge was coated with a white layer of fiberglass-impregnated resin for oil-flow studies. After oil-flow tests were completed, the vertical surfaces were machined for installation of a thin-skin inconel plate instrumented with 37 iron-constantan thermocouples. Locations of the pressure orifices and thermocouples are listed in tables I and II; dimensions of the thermocouple plate are shown in figure 1(b). End plates extending downward to produce an exterior corner were attached to the horizontal and vertical wedges to minimize outflow effects. Noses having various thicknesses and drag coefficients were attached to the

leading edge of the model for blunt-nose tests. Nose dimensions and drag coefficients are shown in figure 1(c).

Model surface pressures were measured with Alphatrons and variable-capacitance transducers; pitot pressures were measured with diaphragm-strain-gage transducers; and tunnel stagnation pressures were measured with calibrated Bourdon tube gages. Data were recorded on a high-accuracy Beckman analog-to-digital recorder.

Heat-transfer data were reduced by means of a technique described in appendix B except for the sharp-nose wedges ($\alpha \neq 0^{\circ}$). These data were reduced for reference 4 by the curve-fit technique, and were not reduced again for this report by the method of appendix B. All data contain some conduction errors due to the effect of a backing material bonded to the thin-skin heat-transfer insert. (See fig. 1(b).) Two levels of heating from a radiant heat source covering approximately the range encountered in the tests were used to calibrate the thermocouple plate. The ratio of instantaneous to initial heating rate for seven thermocouple outputs is shown in figure 2. The ratio decreases with time and is independent of the heat input level during the first 2 seconds, the time within which data reduction was completed. Thus, the heating at each point should be low by the same amount, and in fact, the backing material should minimize lateral conduction effects due to localized high heating rates.

A mixture of Dow Corning 200 silicone oil and lampblack was used for the oil-flow studies. A stiff brush was used to spatter the mixture onto the surface to produce a dense pattern of small oil drops. The resulting random pattern was found to give better definition of the surface patterns than larger oil drops placed in a regular pattern. Photographs of the flow patterns were enhanced by use of a novel dodging technique developed by Leonard M. Weinstein, of Langley Research Center. This technique brought out details in regions of glare, but caused a slightly mottled appearance in some photographs.

A 10-tube pitot rake described in reference 4 was used to traverse a plane perpendicular to the upper surface of the 5° wedge corner in reference 4. Data from the resulting pitot survey are included in this report.

TEST FACILITY

Tests were conducted in the Langley 22-inch helium tunnel, a blowdown tunnel having a run time of about 60 seconds. The free-stream Mach number is between 18 and 22, dependent on stagnation pressure, when a contoured nozzle with a throat diameter of 1.58 cm is used. A calibration for unheated flow conditions can be found in reference 9 along with a description of the facility. Calibrations in hot flow for T_t up to 478 K were found to be essentially the same as for unheated flow in reference 10. During the present series of tests the tunnel calibration was checked and found to be unchanged from that of figure 2 in reference 10. Nominal test conditions are given in the following table:

$p_{t,\infty}$, N/cm^2	M_∞	R_∞/m at T_t of –	
		305 K	450 K
345	19.0	7.3×10^6	4.7×10^6
690	20.3	13.0	8.4
1380	21.5	24.0	15.0

A cross-section view of the 55.4-cm-diameter test section showing the 5° wedge corner model in place is shown in figure 3. Both the vertical and horizontal wedge surfaces extend into the tunnel boundary layer. In the lower part of the figure are listed the pressure orifices and thermocouples within the tunnel boundary layer at various unit Reynolds numbers. Data points at these instrumentation locations are omitted.

DESCRIPTION OF THE FLOW FIELD

Details of the flow structure over sharp-nose symmetrical corners will be summarized before presentation and analysis of the data are made. The description relies basically on the data and analyses presented in references 4, 5, and 11. A plane perpendicular to the x-axis and designated a "base plane" will be used in discussing cross-section characteristics of the flow field; a plane of symmetry simplifies discussion since details need be considered in only half of a base plane view. The angle at which the surfaces intersect is designated ϕ. Most data on symmetrical corner flows, including the present data, are for an intersection angle of 90°; however, theoretical viscous and inviscid solutions and some data (refs. 5, 12, and 13) have been obtained at other angles.

In reference 5, the shock structure and surface features characteristic of supersonic corner flows were first described from data on a 12.2° wedge corner at Mach 3. The wedge boundary layers were laminar. The same basic details were later found at Mach 20 on 5° and 10° wedge corners in reference 4. Figure 4, a base plane view, shows the features of the flow typical of the data of references 4 and 5. The following details can be noted: (a) Shocks from the tip of each wedge do not interesect at the plane of symmetry, but are joined by an intermediate corner or fillet shock; (b) from the intersection of the corner shock and wedge shock, internal flow-field shocks extend inward toward the wedge surface; (c) slip lines extend from the triple-shock point toward the corner, converging at the plane of symmetry; (d) a vortex lies beneath the internal shock, producing a pattern of S-shaped lines in the oil flow and localized high heating; and (e) an outer oil-accumulation line marks the extent of lateral separation of the wedge boundary layer.

The distinct corner shock found at both Mach 3 and Mach 20 in references 4 and 5 is evidently characteristic of the case in which wedge shocks cannot intersect at the plane

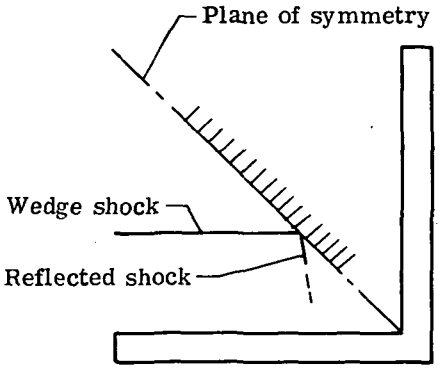

Sketch A

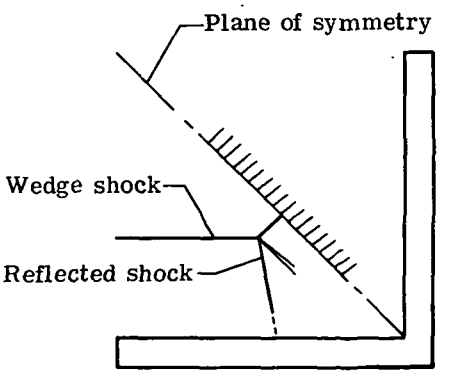

Sketch B

of symmetry. Conditions for which shock intersection can and cannot occur have been calculated by Richard D. Wagner, of Langley Research Center, by considering the problem to be that of shock reflection at the plane of symmetry, as shown in sketch A. (See refs. 14 and 15.) Selected results of Wagner's calculations were presented in reference 4; more complete results are shown in appendix A of this report along with a description of the calculation method.

When shock reflection cannot occur, a Mach reflection occurs, as shown in sketch B. According to reference 14 (p. 558): "When regular crossing of waves . . . is impossible, a Mach reflection occurs . . . . Waves . . . do not meet, but are bridged rather by a nearly normal shock." Slip lines occur at the triple-shock point, as indicated in the sketch. For unsymmetrical cases, the intersection problem is much more complicated than the case considered herein. (See ref. 16.)

The outer shock structure is unaffected by the state of the boundary layers on the surfaces forming the corner. Phenomena close to the surface such as the vortex near the corner and the extent of lateral separation are strongly influenced, however. Reference 11 shows that transition causes the extent of lateral separation to be reduced and the pressure distribution to change as the boundary layer changes from laminar to turbulent. For laminar flow over sharp-nose corners with $\phi = 90^{\circ}$, measured heat-transfer and pressure distributions at Mach 3.2 and Mach 20.3 are shown in figure 5. In the immediate corner region the surface pressure is higher than undisturbed wedge pressure. The heat-transfer distribution shows a definite peak near the corner much higher than would be expected on the basis of the interference pressure rise alone. Early experimental work in reference 17 tentatively attributed the heating on $\alpha = 0^{\circ}$ corners at Mach 5 to the presence of vortices in the flow. Later work by the same author confirmed the presence of these vortices for $\alpha = 0^{\circ}$ symmetrical corners (ref. 18) and on asymmetrical and blunt configurations (ref. 13). Additional visual evidence of strong vortices is found in reference 4 on symmetrical corners at Mach 20 from oil-flow patterns, a pitot survey, and electron-beam flow-visualization photographs.

Some interesting characteristics of the vortex-induced peak heating deserve comment here. It has been found in references 13 and 17 that peak heating, relative to the undisturbed value, is higher for laminar boundary layers than for turbulent. The location of peak heating appears to be only weakly influenced by the state of the boundary layer, at least for fin-plate corners in reference 19. This is not true for the outward extent of disturbed flow, as will be discussed later. Laminar peak heating for 5° and 10° symmetrical corners at Mach 8 is constant in the streamwise direction, within the range of measurements in reference 13.

The only cases for which the flow-field structure has been measured by pitot survey when inviscid shock reflection (or crossing) is possible are those of reference 12 for flat plates intersecting at 60° and 90° at Mach 11.2. Figure 7 of reference 12 is reproduced as figure 6 in this report. At $\phi = 90^{\circ}$ a shock pattern of the Mach reflection type is measured. On the basis of the calculations in appendix A of this report, at $M = 11.2$, $\gamma = 1.4$, and $\phi = 90^{\circ}$ (see fig. 20), a deflection angle of only about 3.5° is necessary before it is impossible for shock intersection to take place. Thick boundary layers could easily produce an effective flow deflection of this magnitude. For the same free-stream conditions but $\phi = 60^{\circ}$, an angle of about 22° must be reached before intersection is impossible. The case shown in figure 6(b) indicates a very small corner shock and an internal flow field quite different from that in figure 6(a). This may be a case in which shock intersection is imminent.

Visualization of the base-plane flow on a 10° sharp-nose corner model from reference 4 is shown in figure 7. The flow is illuminated by a swept electron beam (see ref. 20 for details of the method) which causes the flow to glow with intensity related to the static density. Further flow-field visualization was obtained by using a three-dimensional pitot-pressure plot. The pitot survey on a 5° symmetrical wedge corner was transformed into a plaster model for reference 4, and photographs of the model are shown in figure 8. The wedge shocks, corner shock, slip lines, and vortices can clearly be seen. Note that the internal shock appears to reflect off the vortex and intersect the slip lines.

The region in which the details of the flow are still uncertain lies between the vortex and the outer oil-accumulation line. West and Korkegi in reference 11 refer to the outer oil-accumulation line as the boundary of a separation caused by the impingement of the internal shock on the boundary layer. Their oil-flow photographs show that the outward extent of the line undergoes a marked change as the wedge boundary layers become turbulent. If the outer oil-accumulation line is viewed as the boundary of a separation, it would appear to be of the free-vortex type rather than the bubble type. Both types of separation are discussed in reference 21. Unfortunately, the details of the flow between the vortex and the oil-accumulation line cannot at present be determined from oil-flow patterns, existing pitot surveys, or electron-beam photographs. One possible flow structure which might produce the oil-flow patterns of references 4 and 11 is shown in figure 9.

The feather pattern is shown to be caused by the action of a secondary vortex and the action of the separation vortex sheet which may or may not touch the surface. (See fig. 5 of ref. 13.)

RESULTS AND DISCUSSION

In the following presentation of data, oil-flow photographs are discussed first, with the salient features of the surface flow patterns noted. Next, flow-field development in terms of appropriate shock parameters is discussed, and finally, heat-transfer and pressure data are presented as functions of these parameters.

The data are divided into two basic groups, classified as to whether the corner was formed by the intersection of two plates ($\alpha = 0^{\circ}$) or by the intersection of two wedges ($\alpha \neq 0^{\circ}$). These groups are further classed as flow dominated by viscous effects or by nose-bluntness effects.

Previously, it was found that the flow over corners formed of sharp plates and wedges was basically conical in nature. In reference 4, surface pressures and heat-transfer distributions were found to be similar when plotted in the coordinates y/x or z/x. In the present study, blunting the leading edge of the surfaces forming the corner displaced the flow field outward (away from the corner) in the same way that blunting the leading edge of plates and wedges displaces the shock away from the body. Thus, if the outer two-dimensional shock pattern dominates the flow-field development in the blunted-corner case, then the features observed in the oil-flow patterns should correlate in terms of parameters used in predicting blunt-shock growth. The present oil-flow results show this to be true.

Transition on sharp flat plates and 5° wedges does not occur within the Reynolds number range and model lengths of the present tests. No indication of transition, either from oil-flow studies or in pressure and heat-transfer data, is found for corners composed of intersecting flat plates or 5° wedges. However, on sharp 10° wedges tested in the Langley 22-inch helium tunnel, transition occurs at the locations documented in references 10, 22, and 23. For the unit Reynolds number at which the oil-flow studies were run, the beginning of transition should occur about 21.1 cm from the leading edge. This location is noted in the oil-flow photographs, and discussion of the effects of transition on oil patterns and heat-transfer and pressure data is included elsewhere in this report.

Oil-Flow Photographs

The set of oil-flow photographs for corners formed of 0°, 5°, and 10° wedges having various nose bluntnesses is shown in figure 10. These photographs show the patterns obtained on the vertical fiberglass-coated wedge at a Reynolds number of 1.3×10^{7} per meter in unheated flow. Lines with an arrowhead pointing upstream on the model were

artist-aid transfer marks placed on the model as reference marks 2.5 and 5.1 cm from the corner juncture.

At $\alpha = 0^{\circ}$ (figs. 10(a), (b), (c), and (d)) the patterns are not as distinct as those obtained at $\alpha = 5^{\circ}$ or 10° because of the lower surface shear at this angle; however, a pattern of S-shaped lines defining the area where the vortex scrubs the surface is clearly visible as well as the initial development of an outer oil-accumulation line. These oil-flow studies were made without end plates, so that lateral outflow is usually evident. Between the vortex and the corner, the flow appears almost parallel to the surface, and in the immediate vicinity of the corner, the lack of oil movement indicates the low shear associated with corner boundary layers. (See ref. 24.)

At $\alpha = 5^{\circ}$ (figs. 10(e), (f), and (g)) the pronounced outward displacement of the flow field by nose bluntness is evident when figure 10(e) is compared with figure 10(f). Note the appearance in figure 10(f) of a featherlike pattern adjacent to the vortex. As noted previously, the exact nature of the phenomenon producing this feature is not known. In reference 4, a region characterized by a local peak in pitot pressure extending into the boundary layer from the approximate intersection of the internal shock with the boundary-layer edge was interpreted as the branching of the shock, that is, as one leg of a lambda shock touching the surface at the feather pattern. Other types of flow patterns cannot be discounted, however, and another possibility is shown in figure 9.

The flow-field details observed at 5° are repeated at $\alpha = 10^{\circ}$. Two significant differences can be seen in the flow patterns at $\alpha = 5^{\circ}$ and 10°. In the region between the corner and the vortex, the surface flow appears almost parallel to the corner at $\alpha = 5^{\circ}$, whereas at $\alpha = 10^{\circ}$ there is significant lateral flow away from the corner. The second feature which appears most clearly in the oil-flow pattern for the sharp-nose model at $\alpha = 10^{\circ}$ is a disturbance in the oil-accumulation line. This disturbance coincides with the region where the tunnel-wall boundary layer intersects the surface of the vertical wedge and is assumed to be responsible for the wavy appearance in the oil-accumulation line.

Reference 11 has shown similar results when boundary-layer transition occurs on the model surface. (See, e.g., fig. 4 of ref. 11.) Thus the disturbance in the oil-accumulation line of figure 10(h) may be due to natural transition on the model or to disturbance by the tunnel-wall boundary layer. At these test conditions transition occurs on sharp 10° wedges 21.1 cm from the leading edge, and is the probable cause of the blurring, or washing out, of the feather pattern on $\alpha = 10^{\circ}$ corners. Feather patterns on $\alpha = 5^{\circ}$ corners are still distinct at the base of the model, indicating that transition does not occur for this wedge angle.

Correlation of Oil-Flow Patterns

From the oil-flow photographs, measurements of the beginning and end of the S-shaped pattern (vortex location), feather pattern, and oil-accumulation line were made at different longitudinal locations. The locations of these features were correlated in terms of shock-growth parameters developed for two-dimensional slender bodies in hypersonic flow.

A method for predicting shock shape, surface heating rate, and pressure distribution was developed in reference 25 and modified in reference 26 to provide better agreement with oblique-shock pressure predictions at high Mach numbers. An equation for shock shape for the general case of a two-dimensional planar body at arbitrary angle of attack, with finite nose bluntness, and subject to boundary-layer displacement effects is given in reference 26. For the four special cases of the general case, that is, (1) sharp wedges dominated by viscous effects, (2) wedges dominated by nose-bluntness effects, (3) sharp plates dominated by viscous effects, and (4) plates dominated by nose-bluntness effects, simpler parameters for describing shock development can be used.

The following discussion divides the oil-flow correlations into the above four cases, depending on the geometry of the basic two-dimensional body which was used to form the corner.

Sharp wedges.- From reference 26, the relation describing shock development over sharp wedges subject to boundary-layer displacement effects can be shown to be

$$\frac{B}{A^2}\frac{4M_\infty{}^4\alpha^3 y_s}{(G\bar{\chi})^2 x} = f\left[4\left(\sqrt{\frac{B}{A}}\frac{M_\infty{}^2\alpha^3}{G\bar{\chi}}\right)^2\right] \tag{1}$$

where

$$B = \begin{cases} \gamma & \text{(ref. 26)} \\ 1 & \text{(ref. 25)} \end{cases} \qquad A = \begin{cases} \dfrac{\gamma+1}{2} & \text{(ref. 26)} \\ 1 & \text{(ref. 25)} \end{cases}$$

and y_s is the shock coordinate measured from the x-axis. The term $G\bar{\chi}$ in equation (1) is equivalent to $\frac{\gamma+1}{2}\chi_\epsilon$ in references 25 and 26. For helium, the following equation for G from reference 27 was used:

$$G = \frac{\gamma-1}{2}\left(2.075\frac{T_w}{T_t} + 0.594\right) \tag{2}$$

where for helium the Prandtl number is assumed to be 0.688 and the laminar recovery factor, $\sqrt{0.688}$. The Monaghan equation for laminar reference temperature (see ref. 27) was used in evaluating the C' term in $\bar{\chi}$.

Figure 11 shows the vortex location, oil-accumulation line, and feather-pattern location for sharp-wedge corners plotted in parameters specified by the functional relationship of equation (1). No feather pattern could be seen for $\alpha = 5^{\circ}$. Also plotted are the two-dimensional shock location from hypersonic small-disturbance theory

$$\frac{y_s}{x} = \frac{\gamma + 1}{2} \alpha \tag{3}$$

and that from reference 28 which includes viscous effects:

$$\frac{y_s}{\alpha x} = \frac{\gamma + 1}{4} \left[1 + \sqrt{\frac{4\bar{G}\bar{\chi}}{(M_\infty \alpha)^2} + 1} \right] \tag{4}$$

where $\bar{G} = \sqrt{\frac{2}{\gamma(\gamma + 1)}}\, G$, or B in reference 28. The shock locations are shown for reference since the shock from one surface does not extend through the corner flow field to touch the other surface. The vortex begins very close to the point where the shock from one wedge could be projected through the corner flow field onto the surface of the other wedge, a conclusion reached in reference 4.

In order to determine whether this trend might occur in air as well as helium and over what range of Mach number it occurs, the location of the internal shock was determined by the method of reference 6. The ratio of the internal shock coordinate to the sharp-wedge shock coordinate for $\alpha = 2^{\circ}$, 5°, and 10° and Mach numbers up to 20 is plotted in figure 12. The effect of wedge angle on this ratio is greater in helium than in air; however, in both cases, it can be seen that the internal shock will lie very close to a projected wedge-shock location for the supersonic and hypersonic regimes.

For the data shown in figure 11, a simple power-law variation of $y/\alpha x$ with $(M_\infty \alpha)^2/G\bar{\chi}$ was found to fit the outer oil-accumulation line, feather pattern at $\alpha = 10^{\circ}$, and outer extent of the vortex. The relation is shown in the figure, and the power-law variation was used in correlating heat-transfer data.

Blunt wedges.- The shock shape on blunt wedges in hypersonic flow is described by the following parameters from reference 26:

$$\frac{\alpha^2}{\epsilon C_D} \frac{y_s}{r} = f\left(\frac{A\alpha^3}{\epsilon C_D} \frac{x}{r} \right) \tag{5}$$

In reference 29 an equation for the shock shape on blunt slender bodies in hypersonic flow is derived. For helium the relation is

$$\frac{\alpha^2}{C_D}\frac{y_s}{r} = 1.183\left(\frac{\alpha^3}{C_D}\frac{x}{r}\right)^{2/3} + 0.244\,\frac{\alpha^3}{C_D}\frac{x}{r} \tag{6}$$

The present data in terms of these parameters are correlated in figure 13. The outer oil-accumulation line does not correlate as well as the vortex region, perhaps because of the edge bleed-off effects. (See fig. 10.) The vortex location and feather pattern are correlated, and as for sharp wedges, the vortex location appears to begin just outside the projected blunt-shock location.

In correlating heat-transfer data, a power-law variation is assumed. Within the range of $\frac{\alpha^3}{C_D}\frac{x}{r}$ for the present data, the 2/3 power of the first term in equation (6) dominates the theoretical prediction. A 2/3-power-law equation is shown in figure 13 with constants which adequately fit the oil-accumulation line, feather pattern, and outer edge of the vortex.

Sharp plates. - *No oil-flow data were obtained for sharp-plate corners; however, the* correlation for sharp- and blunt-wedge corners indicated that shock parameters could be used to correlate sharp-plate data also. From reference 26, the shock development on sharp plates for viscous-dominated flow in helium is described by

$$M_\infty \frac{y_s}{r} = 1.44\sqrt{G\bar{\chi}}\,\frac{x}{r} \tag{7}$$

This relation is used to correlate sharp-corner pressures and heating at $\alpha = 0^\circ$.

Blunt plates. - The shock shape on blunt-plate corners is given by the following equation from reference 26:

$$M_\infty \frac{y_s}{x} = A^{2/3}1.313\left(\frac{2\epsilon M_\infty{}^3 C_D}{x/r}\right)^{1/3} \tag{8}$$

For helium, this becomes

$$\frac{y_s}{r} = 1.262 C_D{}^{1/3}\left(\frac{x}{r}\right)^{2/3} \tag{9}$$

Oil-flow data are shown in figure 14 with the shock-shape prediction of equation (9). In general, the same trends found for sharp and blunt wedges are found; that is, shock parameters correlate the position of the outer oil-accumulation line and the vortex location. No feather patterns could be discerned for blunt-plate corners.

Heat-Transfer and Pressure Distribution Data

Heat-transfer and pressure distributions are divided into the four groups used in discussing correlations of oil-flow patterns. Pressure measurements were made in unheated flow; however, the free-stream Mach number is the same as for hot-flow heat-transfer runs at the same tunnel stagnation pressure. Data at each x-location of instrumentation are nondimensionalized by either theoretical or experimental values which would be obtained at the same x-location on the basic configuration forming the corner (i.e., undisturbed by corner interference effects). In some cases closed-form solutions for surface pressures were used in calculating theoretical pressure levels; otherwise, the method of reference 26 was used.

The theory of reference 25 for blunt, slender bodies, derived assuming $\gamma \to 1$, was modified in reference 26 to better predict pressures on sharp wedges in helium. It was noted in reference 26 that as bluntness effects became more significant, the modified theory gave surface pressures that were increasingly too high, while the unmodified theory gave increasingly more correct values. This effect was attributed to the neglect of certain pressure-gradient terms in the modified theory. For corners formed of blunt plates, the nondimensional pressure distributions approach a value less than 1 as the undisturbed edge of the flow field is approached; calculated pressures are evidently too high.

In plotting pressure data, different symbols were used for each x-location to demonstrate the similarity of the flow field at different longitudinal positions. Pressure tubes were arranged in rows parallel to the leading edge. Heat-transfer data are plotted as one symbol since the thermocouple plate at angle of attack produced a different x-location for each thermocouple. Flagged symbols denote reruns. For all the heat-transfer and pressure plots, the case number gives the tunnel conditions, as listed in table III. Table IV lists the heat-transfer and pressure data.

Sharp wedges.- Heat-transfer and pressure data on corners constructed of intersecting sharp 5° and 10° wedges are shown in figure 15 for three different tunnel stagnation pressures at each wedge angle α.

Pressures are nondimensionalized by theoretical pressures on sharp wedges with self-induced boundary-layer effects. The following equation from reference 28 was used in calculating the theoretical pressure level:

$$\frac{1}{\gamma(M_\infty\alpha)^2}\frac{p_e}{p_\infty} = \frac{\gamma+1}{2}\left[\frac{1}{2}+\frac{1}{2}\sqrt{\frac{4\overline{G\chi}}{(M_\infty\alpha)^2}+1}+\frac{\overline{G\chi}}{(M_\infty\alpha)^2}\right]\left[1-\frac{\overline{G\chi}/(M_\infty\alpha)^2}{\sqrt{\frac{4\overline{G\chi}}{(M_\infty\alpha)^2}+1}+\frac{4\overline{G\chi}}{(M_\infty\alpha)^2}+1}\right] \tag{10}$$

Heat-transfer rates q are nondimensionalized by experimental undisturbed edge values, as in reference 4.

Shown in figure 15 are the values of the parameter $\frac{y}{\alpha x}\left[\frac{(M_\infty \alpha)^2}{G\bar{\chi}}\right]^{1/4}$ at which the edge of the vortex, the feather pattern (for $\alpha = 10^\circ$ only), and the oil-accumulation line are located. The data for all six cases show the distinct discontinuity in surface pressure characteristic of the corner flow field with nonintersecting shocks. (See refs. 4 and 5.) Peak heating lies between the corner juncture and the vortex edge, while a dip in heating occurs between the vortex edge and oil-accumulation line. Outside the oil-accumulation line, the heating approaches the undisturbed edge value.

Heating rates should approach zero in the corner, as found in reference 18. The data of figure 15 show a continual increase in heating toward the corner, and the highest measured heating does not appear to be located beneath the vortex, as subsequent discussion will show that it is for blunt-nose corners. For sharp-nose corners, the vortex is relatively much closer to the corner than for blunt-nose corners; thus, the heat-transfer insert may not have provided sufficient resolution to determine accurately the location of peak heating. As can be seen in figure 11, the parameter used to plot heat-transfer data does not correlate the flow field well between the corner and the outer extent of the vortex development.

Boundary-layer transition may influence heating rates on the 10° sharp corner; however, no distinct trend associated with this effect can be found in the data. Maximum measured heating rates on the order of 10 times the undisturbed value are found, while interference pressures are less than 4 times the undisturbed edge values.

Blunt wedges.- Pressures and heating rates on 5° and 10° wedge corners are shown in figure 16. At each wedge angle, data are shown for three different nose bluntnesses at constant stagnation pressure. Pressures and heating rates are nondimensionalized by theoretical values from the modified theory of reference 26. Values of q were calculated from theoretical Stanton numbers defined as

$$N_{St} = \frac{q}{\rho u c_p (T_{aw} - T_w)} \tag{11}$$

where T_{aw} was found by using the laminar recovery factor of reference 30 for helium flow.

Correlation of the flow field in shock parameters appears to be better as relative nose bluntness decreases. (Compare figs. 16(a) with 16(b) and (c), and 16(d) with 16(e) and (f).) Also, for $\alpha = 10^\circ$, transition effects degrade the correlation achieved.

At $\alpha = 5^{\circ}$ peak heating occurs near the outer edge of the vortex, just beneath the discontinuity in surface pressure. Between the vortex edge and the oil-accumulation line, a dip is evident with possibly a second, lower peak occurring at the feather pattern. Since no oil-flow data were obtained for 20° noses, correlated locations of the vortex edge, feather pattern, or oil accumulation are not shown in figures 16(a) and 16(d). It is evident that the basic pattern is the same as that for the other blunt wedges, however. The ratio of peak to undisturbed edge values of pressure are between 2 and 4, while peak heating ratios are between 5 and 9.

Sharp plates.- As for corners formed of blunt plates and wedges and for sharp wedges, shock parameters defined in equation (7) were used to correlate the heat-transfer data for sharp-plate corners. Heating rates were not nondimensionalized by their edge values but by a theoretical value obtained from the method of reference 26. Pressures were nondimensionalized by the viscous-induced flat-plate value from the equation

$$\frac{p_e}{p_\infty} = 0.83 + \frac{3}{4}\sqrt{\frac{\gamma(\gamma + 1)}{2}}\, G\bar{\chi} \tag{12}$$

which, except for notation, is the same as equation (18) in reference 31. The resulting data are shown in figure 17 along with the location of the strong interaction shock from equation (7).

Good correlation of data is not achieved for either the pressure data or the heat-transfer data. On intersecting sharp plates the initial growth of the boundary layer can generate strong shocks, but these rapidly decrease in strength downstream. It is possible that shocks initially unable to cross because of flow deflection by the boundary layer or vortex may at some downstream location be able to cross and thus change the interaction flow pattern. As a complicating factor, the initial growth pattern of the vortices is unknown at this time.

The data of reference 18 correlate in terms of boundary-layer-growth parameters but only after a finite distance along the plate is reached. This is probably a case of shock crossing in view of the fact that $\bar{\chi}$ is less than 1 for most of the data. For the present data values of $\bar{\chi}$ are relatively large; thus, a changing shock pattern may account for the poor correlation.

Blunt plates.- Data for blunt-plate corners are shown in figure 18 for one stagnation pressure and four nose bluntnesses. Blunt-shock parameters provide adequate similarity in pressure and heat-transfer distributions for all four cases; however, the correlation appears to be slightly better as the range of the parameter $C_D{}^{1/3}\left(\frac{x}{r}\right)^{2/3}$ decreases, as shown in the oil-flow correlation of figure 14.

Pressure and heat-transfer distributions are similar to those obtained on sharp and blunt wedges. No feather patterns could be observed in the oil-flow photographs, and no second peak in heating is evident in any of the four heat-transfer distributions on blunt plates. It is evident that the distinct second peak in heating observed in reference 5 on a 12.2° sharp-leading-edge corner at $M \approx 3$ is associated with the appearance of the feather pattern. Whether or not the feather pattern is observed is obviously associated with the state of the boundary layer, that is, whether laminar, transitional, or turbulent, and the strength of the shock structure.

The ratio of measured to calculated undisturbed pressure varies from about 0.6 to a maximum of about 1.5 in figure 18. Since calculated pressures are known to be high for these cases, it is probable that the true value of interference pressure should be between 2 and 3 when the undisturbed edge values approach 1. Heating rates, on the other hand, appear to be more nearly correct, giving heating peaks of about 8 and approaching undisturbed edge values of about 1.

CONCLUSIONS

The effect of nose bluntness on the flow field of symmetrical, streamwise corners formed of 0°, 5°, and 10° wedges has been examined at Mach 20 in helium. Heat-transfer and pressure distributions have been measured and oil-flow studies made to determine the factors controlling similarity in the flow field. The following conclusions are drawn from the results of this study:

1. Heat-transfer and pressure distributions on the surface of the corner models show similarity in terms of two-dimensional blunt-shock parameters. The similarity is demonstrated by correlation of the vortex location, feather pattern, and oil-accumulation line on corners having noses of different drag coefficients and thicknesses. In general, the data show good correlation for sharp-nose corners and for corners having low nose bluntness. The correlation degrades as nose bluntness increases and as the angle of the wedges forming the corner increases. On the 10° corner, transition effects reduce the correlation.

2. The existence of a secondary peak in heating, observed in other studies at supersonic Mach numbers in air, is related to a feather pattern appearing in some of the oil-flow photographs. In laminar flow for the present test conditions, the feather pattern does not appear unless surface shear rates are sufficiently high. In turbulent flow, the pattern appears to disappear completely. Thus, the magnitude of the second peak in heating is probably a strong function of the strength of the interference flow field as well as the state of the boundary layer.

3. The cause of the feather pattern is not clear, although it may be due to a vortex-sheet type of separation. Details of the three-dimensional flow between the vortex and outer line of separation are needed. Existing pitot surveys and flow-visualization results are not sufficient to clarify details of the flow in this region.

4. Peak heating rates are usually about 8 times the undisturbed edge value. For the sharp-plate (0° wedge) corners, the measured ratio is about 1.5. Ratios of interference pressures to undisturbed edge values in the immediate corner range from about 1.5 on sharp plates to 4 on sharp wedges. Blunted plates and wedges show interference pressures between these values.

Langley Research Center,
National Aeronautics and Space Administration,
Hampton, Va., October 30, 1973.

APPENDIX A

LIMITING CONDITIONS FOR SHOCK INTERSECTION ON SYMMETRICAL SHARP-NOSE CORNERS

The objective of the following analysis is to determine under what conditions the shock waves produced by two intersecting wedges can intersect with plane refraction, as illustrated in sketch C. Only symmetrical intersections will be considered, and hence the xz'-plane is a plane of symmetry.

The following symbols are defined differently than in the body of the paper:

z' coordinate in plane of symmetry, see sketch C

ϵ shock angle relative to free-stream velocity vector

ϕ one-half the angle between wedge leading edges

ω shock angle relative to plane of symmetry

Subscripts:

1 incident value, also free-stream component normal to line of intersection of wedge shocks (fig. 19)

2 value behind oblique shock (fig. 19)

The geometry of the problem about the plane of symmetry is shown in spherical coordinates in sketch D. When the plane of symmetry is viewed as a solid boundary, the present shock intersection problem reduces to the simple problem of an oblique shock wave reflected from a wall. From spherical geometry, the incident shock angle relative to the plane of symmetry is

$$\cos \omega = \cos \phi \cos \epsilon \tag{A1}$$

where ϵ is the two-dimensional wedge shock angle and 2ϕ is the angle between wedge leading edges. The Mach number component of the free stream normal to the line of intersection of the wedge shocks in the plane of symmetry is

$$\frac{M_1}{M_\infty} = \frac{\sin \epsilon}{\left(1 - \cos^2\phi \cos^2\epsilon\right)^{1/2}} \tag{A2}$$

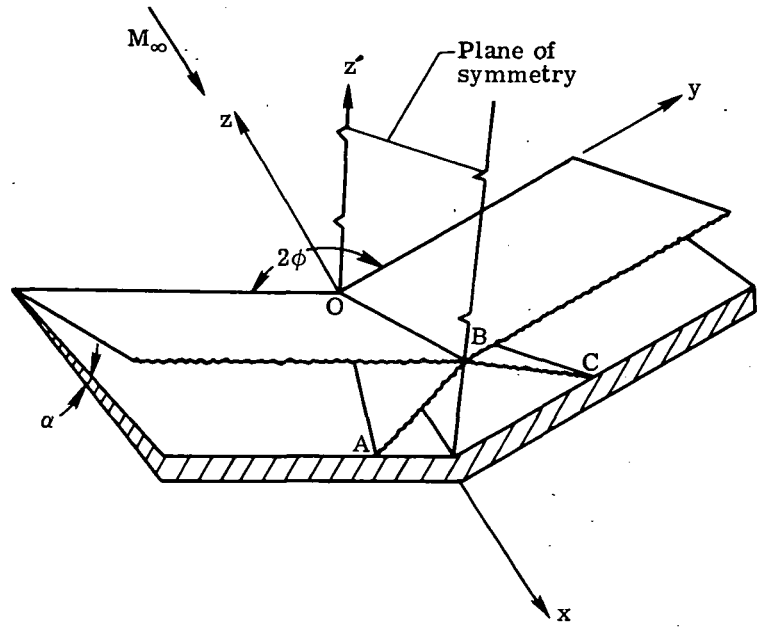

Sketch C

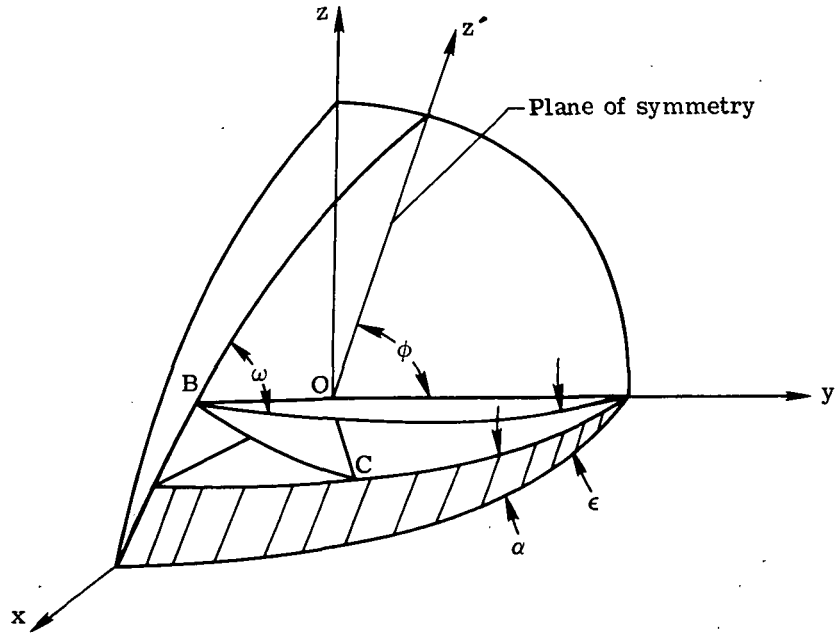

Sketch D

The solution of the problem of the plane reflection of an oblique shock from a solid wall is given in reference 15, where it is shown that plane reflections can occur only for a limited set of incident shock angles ω and Mach numbers M_1. The boundaries of possible plane reflections obtained in reference 15 for $\gamma = 1.4$ and calculations made for $\gamma = 1.667$ are shown in figure 19. The limiting incident shock angles are shown for shock strengths p_1/p_2 from 0 to 1 $(M_1 = \infty$ to 1, respectively$)$. The shock strength is related to ω, M_1, and γ by the oblique-shock equation from reference 32:

$$\frac{p_2}{p_1} = \frac{2\gamma M_1^2 \sin^2\omega - (\gamma - 1)}{\gamma + 1} \tag{A3}$$

By using equations (A1) to (A3) and the relations of figure 19, it is possible to determine whether wedge shocks can intersect for a given geometry and flow condition. A simple computer program was written to calculate the limiting wedge angle α at which shock intersection can occur as a function of free-stream Mach number for fixed values of ϕ and γ.

The results for $\gamma = 1.4$ are shown in figure 20(a), and for $\gamma = 1.667$ in figure 20(b). Above a line of constant ϕ, intersection is impossible from a shock-reflection standpoint; below the line, possible. (Note that 2ϕ is the physical wedge-intersection angle.) It must be emphasized that the possibility of planar intersection and refraction does not suggest that such a shock system will occur: the flow must ultimately satisfy the surface boundary conditions on each wedge, which may or may not be incompatible with the flow established behind the refracted shocks, shock planes OBA and OBC.

This analysis was made by Richard D. Wagner, of Langley Research Center, who also performed the calculations and supplied the results to the author for inclusion in this report.

APPENDIX B

REDUCTION OF HEAT-TRANSFER DATA

Heating on thin-skinned models is often calculated by taking a second-order least-squares curve fit to each temperature-time thermocouple output. The temperature-time derivative can be calculated at each data point, and the heat-transfer rate q calculated from the following equation:

$$q = \rho c_p \tau \frac{dT_w}{dt} \tag{B1}$$

Here, ρ is the density of the skin material; c_p, the specific heat of the material; and τ, the skin thickness. The film coefficient of heat transfer h is defined by the equation

$$h \equiv \frac{q}{T_{aw} - T_w} \tag{B2}$$

Combining equations (B1) and (B2) gives

$$h\,dt = \rho c_p \tau \frac{dT_w}{T_{aw} - T_w}$$

Assuming h, ρ, and c_p to be constant (within the range of temperature variation encountered in the data reduction), and integrating the above equation yields

$$h = \frac{\rho c_p \tau}{t} \int \frac{dT_w}{T_{aw} - T_w} \tag{B3}$$

and if T_t, and thus T_{aw}, is not time dependent,

$$h = \frac{\rho c_p \tau}{t} \ln\left(\frac{T_{aw} - T_{w,i}}{T_{aw} - T_w}\right) \tag{B4}$$

where $T_{w,i}$ is the initial value of wall temperature.

Film coefficients were calculated by equations (B2) and (B3) for one channel of a typical heat-transfer run, test 327, run 5. Stagnation conditions for this run are shown in figure 21. Starting transients in the Langley 22-inch helium tunnel usually last from 3/4 to 1 sec, and in figure 21, constant total temperature is reached at frame 28. Values of h calculated by equations (B2) and (B3) for test 327, run 5, are listed in the following table:

Point	Time, sec	T_w, K	T_t, K	h, mW/cm^2-K, from –	
				Eq. (B2)	Eq. (B3)
1	0	309.46	424.07	1.251	----
2	.05	309.57	424.24	1.264	1.647
3	.1	309.63	423.35	1.310	1.240
4	.15	309.69	423.36	1.268	1.248
5	.2	309.80	424.07	1.324	1.250
6	.25	309.85	424.52	1.330	1.331
7	.3	309.96	424.80	1.338	1.315
8	.35	309.96	424.85	1.355	1.245
9	.4	310.13	425.02	1.370	1.346
10	.45	310.19	425.24	1.379	1.288

In calculating q, a quadratic equation for T_w against t was found by the least-squares method. Instantaneous derivatives were found from the coefficients. For equation (B3), the trapezoidal rule was used to perform the integration using instantaneous values of T_t.

In view of the good agreement between equations (B2) and (B3), equation (B3) was used to reduce most of the heat-transfer data in this report. Data on corners formed by intersecting sharp wedges were reduced in reference 4 by the curve-fit method. The point at which data reduction was begun was chosen in a manner similar to that of reference 33. Instead of plotting $\ln\left(\frac{T_{aw} - T_{w,i}}{T_{aw} - T_w}\right)$ against time, however, $\ln(T_{aw} - T_w)$ was plotted against time, as shown in figure 22. A straight line indicates constant h.

REFERENCES

1. Whitehead, Allen H., Jr.; and Bertram, Mitchel H.: Alleviation of Vortex-Induced Heating to the Lee Side of Slender Wings in Hypersonic Flow. AIAA J., vol. 9, no. 9, Sept. 1971, pp. 1870-1872.

2. Rubin, S. G.; Lin, T. C.; Pierucci, M.; and Rudman, S.: Hypersonic Interactions Near Sharp Leading Edges. AIAA J., vol. 7, no. 9, Sept. 1969, pp. 1744-1751.

3. Cresci, R. J.; Rubin, S. G.; Nardo, C. T.; and Lin, T. C.: Hypersonic Interaction Along a Rectangular Corner. AIAA J., vol. 7, no. 12, Dec. 1969, pp. 2241-2246.

4. Watson, Ralph D.; and Weinstein, Leonard M.: A Study of Hypersonic Corner Flow Interactions. AIAA J., vol. 9, no. 7, July 1971, pp. 1208-1286.

5. Charwat, A. F.; and Redekopp, L. G.: Supersonic Interference Flow Along the Corner of Intersecting Wedges. Mem. RM-4863-PR (Contract No. AF 49(638)-1700), RAND Corp., July 1966.

6. Watson, Ralph D.: Corner Pressures and Fillet Shock Locations for Symmetrical Corners by an Approximate Method. J. Spacecraft & Rockets, vol. 10, no. 1, Jan. 1973, pp. 90-92.

7. Rubin, Stanley G.: Incompressible Flow Along a Corner. Pt. I – Boundary Layer Solutions and Formulation of Corner Layer Problem. AFOSR-65-1420, U.S. Air Force, May 1965. (Available from DDC as AD 621 987.)

8. Libby, Paul A.: Secondary Flows Associated With a Supersonic Corner Region. AIAA J., vol. 4, no. 6, June 1966, pp. 1130-1132.

9. Arrington, James P.; Joiner, Roy C., Jr.; and Henderson, Arthur, Jr.: Longitudinal Characteristics of Several Configurations at Hypersonic Mach Numbers in Conical and Contoured Nozzles. NASA TN D-2489, 1964.

10. Arrington, James P.: Heat-Transfer and Pressure Distributions Due to Sinusoidal Distortions on a Flat Plate at Mach 20 in Helium. NASA TN D-4907, 1968.

11. West, John W.; and Korkegi, Robert H.: Supersonic Interaction in the Corner of Intersecting Wedges at High Reynolds Numbers. AIAA J., vol. 10, no. 5, May 1972, pp. 652-656.

12. Cresci, R. J.; Rubin, S. G.; and Nardo, C. T.: Hypersonic Flow in Rectangular and Non-Rectangular Corners. Hypersonic Boundary Layers and Flow Fields, AGARD CP No. 30, May 1968.

13. Stainback, P. Calvin; and Weinstein, Leonard M.: Aerodynamic Heating in the Vicinity of Corners at Hypersonic Speeds. NASA TN D-4130, 1967.

14. Shapiro, Ascher H.: The Dynamics and Thermodynamics of Compressible Fluid Flow, Vol. 1. Ronald Press Co., c.1953.

15. Von Mises, Richard: Mathematical Theory of Compressible Fluid Flow. Academic Press, Inc., 1958.

16. Keldysh, V. V.: Intersection of Two Plane Shock Waves in Space. Appl. Math. & Mech. (Translation of PMM), vol. 30, no. 1, 1966, pp. 232-237.

17. Stainback, P. Calvin: An Experimental Investigation at a Mach Number of 4.95 of Flow in the Vicinity of a 90° Interior Corner Alined With the Free-Stream Velocity. NASA TN D-184, 1960.

18. Stainback, P. Calvin: Heat-Transfer Measurements at a Mach Number of 8 in the Vicinity of a 90° Interior Corner Alined With the Free-Stream Velocity. NASA TN D-2417, 1964.

19. Neumann, Richard D.; and Burke, Gerald L.: The Influence of Shock Wave-Boundary Layer Effects on the Design of Hypersonic Aircraft. AFFDL-TR-68-152, U.S. Air Force, Mar. 1969. (Available from DDC as AD 686 738.)

20. Weinstein, Leonard M.; Wagner, Richard D., Jr.; Henderson, Arthur, Jr.; and Ocheltree, Stewart L.: Electron Beam Flow Visualization in Hypersonic Helium Flow. ICIASF '69 Record, IEEE Publ. 69-C-19 AES, pp. 72-78.

21. Wang, K. C.: Separation Patterns of Boundary Layer Over an Inclined Body of Revolution. AIAA J., vol. 10, no. 8, Aug. 1972, pp. 1044-1050.

22. Maddalon, Dal V.: Effect of Varying Wall Temperature and Total Temperature on Transition Reynolds Number at Mach 6.8. AIAA J., vol. 7, no. 12, Dec. 1969, pp. 2355-2357.

23. Wagner, R. D., Jr.; Maddalon, D. V.; and Weinstein, L. M.: Influence of Measured Freestream Disturbances on Hypersonic Boundary-Layer Transition. AIAA J., vol. 8, no. 9, Sept. 1970, pp. 1664-1670.

24. Bloom, Martin H.; and Rubin, Stanley: High-Speed Viscous Corner Flow. J. Aerosp. Sci., vol. 28, no. 2, Feb. 1961, pp. 145-157.

25. Cheng, H. K.; Hall, J. Gordon; Golian, T. C.; and Hertzberg, A.: Boundary-Layer Displacement and Leading-Edge Bluntness Effects in High-Temperature Hypersonic Flow. J. Aerosp. Sci., vol. 28, no. 5, May 1961, pp. 353-381, 410.

26. Kemp, Joseph H., Jr.: Hypersonic Viscous Interaction on Sharp and Blunt Inclined Plates. AIAA J., vol. 7, no. 7, July 1969, pp. 1280-1289.

27. Bertram, Mitchel H.: Hypersonic Laminar Viscous Interaction Effects on the Aerodynamics of Two-Dimensional Wedge and Triangular Planform Wings. NASA TN D-3523, 1966.

28. Feldhuhn, Robert H.: An Experimental Investigation of the Effects of Leading Edge Reynolds Number and Angle of Attack on the Flow of Helium Over a Flat Plate at M = 16.35. Gas Dyn. Lab. Intern. Memo. 8, Princeton Univ., July 1965.

29. Mirels, Harold; and Thornton, Philip R.: Effect of Body Perturbations on Hypersonic Flow Over Slender Power Law Bodies. NASA TR R-45, 1959.

30. Nicoll, K. M.: Investigation of the Laminar Boundary Layer on a Flat Plate in Helium Using the Crocco Method. ARL 62-345, U.S. Air Force, May 1962.

31. Bertram, Mitchel H.; and Blackstock, Thomas A.: Some Simple Solutions to the Problem of Predicting Boundary-Layer Self-Induced Pressures. NASA TN D-798, 1961.

32. Ames Research Staff: Equations, Tables, and Charts for Compressible Flow. NACA Rep. 1135, 1953. (Supersedes NACA TN 1428.)

33. Haslett, Robert A.; Kaufman, Louis G., II; Romanowski, Richard F.; and Urkowitz, Michael: Interference Heating Due to Shock Impingement. AFFDL-TR-72-66, U.S. Air Force, July 1972.

TABLE I.- PRESSURE-ORIFICE LOCATIONS AT $\alpha = 0^{\circ}$

Orifice	x, cm	z, cm
1	4.445	[a]0.381
2		1.143
3		1.905
4		3.175
5		4.445
6		5.715
7	6.985	[b].381
8		[a]1.143
9		1.905
10		3.175
11		4.445
12		5.715
13		6.985
14	11.811	[b].381
15		[a]1.143
16		[a]1.905
17		3.175
18		4.445
19		5.715
20		6.985
21		8.255
22		9.525
23	16.510	[b].381
24		[b]1.143
25		[a]1.905
26		3.175
27		4.445
28		5.715
29		6.985
30		8.255
31		9.525
32	21.590	[a]3.175
33		4.445
34		8.255
35		9.525
36		10.795
37		12.065

[a]Covered at $\alpha = 10^{\circ}$.

[b]Covered at $\alpha = 5^{\circ}$ and 10°.

TABLE II.- THERMOCOUPLE LOCATIONS AT $\alpha = 0^{o}$

Thermocouple	x, cm	y, cm
1	21.590	12.065
2	16.510	10.795
3	21.590	10.795
4	11.811	9.525
5	16.510	↓
6	21.590	↓
7	6.985	8.255
8	11.811	↓
9	16.510	↓
10	21.590	↓
11	6.985	6.985
12	11.811	↓
13	16.510	↓
14	21.590	↓
15	6.985	5.715
16	11.811	↓
17	16.510	↓
18	21.590	↓
19	6.985	4.445
20	11.811	↓
21	16.510	↓
22	21.590	↓
23	6.985	3.175
24	11.811	↓
25	16.510	↓
26	21.590	↓
27	6.985	1.905
28	11.811	↓
29	16.510	↓
30	21.590	↓
31	6.985	.635
32	9.271	↓
33	11.811	↓
34	14.300	↓
35	16.510	↓
36	19.050	↓
37	21.590	↓

TABLE III.- TEST CONDITIONS

Case	α, deg	Nose (a)	Pressure-distribution tests			Heat-transfer tests			
			$p_{t,\infty}$, MN/m^2	T_t, K	M_∞	$p_{t,\infty}$, MN/m^2	T_t, K	T_w/T_t	M_∞
1	5	Sharp	3.53	305.6	18.9	3.55	411	0.73	19.0
2	↓	↓	6.99	↓	20.3	6.96	423	.72	20.3
3	↓	↓	13.93	↓	21.5	13.96	473	.65	21.5
4	10	↓	3.58	↓	19.0	3.56	334	.71	19.0
5	10	↓	7.08	↓	20.3	7.00	360	.69	20.3
6	10	Sharp	13.98	305.6	21.5	13.96	380	0.70	21.5
7	5	1	6.99	↓	20.3	7.00	490	.62	20.3
8	↓	2	↓	↓	↓	6.96	490	.62	↓
9	↓	4	↓	↓	↓	7.00	493	.65	↓
10	10	1	7.00	↓	↓	7.00	464	.66	↓
11	10	2	7.01	305.6	20.3	6.98	507	0.62	20.3
12	10	4	6.98	↓	20.3	7.01	499	.64	20.3
13	0	Sharp	3.55	↓	18.9	3.60	424	.72	19.0
14	↓	↓	7.03	↓	20.3	7.00	445.5	.70	20.3
15	↓	↓	13.93	↓	21.5	12.86	426	.72	21.5
16	0	1	7.00	305.6	20.3	7.10	463	0.65	20.3
17	↓	2	7.03	↓	↓	6.98	495	.62	↓
18	↓	3	7.01	↓	↓	7.05	429	.71	↓
19	↓	4	7.01	↓	↓	7.01	454	.67	↓

[a]See figure 1(c).

TABLE IV.- PRESSURE AND HEAT-TRANSFER DATA

(a) Pressures

Orifice	p/p_∞ for –									
	Case 1	Case 2	Case 3	Case 4	Case 5	Case 6	Case 7	Case 8	Case 9	Case 10
1	----	----	----	-----	-----	----	----	----	----	-----
2	21.11	20.85	19.98	115.70	128.14	----	56.59	77.49	61.91	118.67
3	18.43	18.33	17.42	76.48	46.15	44.61	35.12	68.84	56.57	102.92
4	16.43	16.55	15.63	42.70	43.45	42.16	29.69	61.45	40.02	51.07
5	15.12	15.22	14.43	38.02	38.77	37.37	27.48	47.16	35.68	48.42
6	----	14.42	13.69	34.13	35.21	34.69	24.08	40.40	30.33	43.23
7	----	----	----	-----	-----	----	----	----	----	-----
8	25.59	25.30	24.00	-----	-----	----	45.18	57.93	47.09	-----
9	18.31	18.35	17.41	84.23	83.02	83.72	49.20	59.23	48.06	107.32
10	16.66	16.85	15.97	44.70	45.65	43.54	24.58	58.75	46.87	46.73
11	15.39	15.53	14.88	42.18	43.25	41.74	25.33	41.59	32.42	46.46
12	14.30	14.33	13.77	38.32	39.05	37.81	23.45	37.69	29.86	44.55
13	13.57	13.84	13.38	35.73	36.44	35.71	21.78	35.26	27.60	42.53
14	----	----	----	-----	-----	----	----	----	----	-----
15	----	37.86	38.66	-----	-----	----	39.76	48.41	39.97	-----
16	24.54	22.82	20.47	-----	-----	----	39.81	48.79	40.47	-----
17	16.47	16.53	15.98	95.70	92.08	92.07	42.22	47.78	39.33	103.68
18	16.24	16.43	15.97	-----	-----	----	21.62	49.16	39.83	-----
19	14.87	15.15	14.72	41.52	43.06	42.67	20.95	46.45	25.55	45.31
20	14.19	14.35	14.05	39.54	40.55	39.20	20.20	29.84	25.41	43.27
21	----	----	----	37.07	39.55	40.35	----	----	24.36	42.13
22	13.10	13.50	13.31	35.38	37.94	38.59	17.72	25.68	23.16	41.11
23	----	----	----	-----	-----	----	----	----	----	-----
24	----	----	----	-----	-----	----	----	----	----	-----
25	32.48	36.51	36.04	-----	-----	----	34.05	38.27	35.45	-----
26	15.38	15.74	14.77	119.8	139.7	----	36.56	40.23	36.19	109.40
27	15.63	15.93	15.46	77.58	73.07	68.81	34.12	39.52	34.87	107.50
28	14.63	15.09	14.44	39.80	45.98	49.17	17.95	37.80	32.80	76.13
29	14.58	14.76	14.25	39.82	43.59	44.62	----	34.10	22.64	47.24
30	13.87	14.34	13.76	38.89	42.25	44.01	17.94	24.28	22.79	43.22
31	13.16	13.69	13.23	37.32	40.64	41.30	17.12	23.40	21.76	41.83
32	27.58	28.80	25.40	-----	-----	----	33.84	35.58	33.30	-----
33	14.26	15.01	14.38	117.3	140.3	----	34.13	35.39	31.86	111.00
34	13.39	14.01	13.50	-----	45.44	51.65	16.73	31.40	20.65	47.19
35	----	----	----	37.56	43.22	49.38	16.22	21.03	20.39	44.97
36	12.55	13.18	12.78	37.56	41.96	45.92	15.98	20.98	18.99	41.78
37	----	12.76	12.31	-----	39.66	39.88	15.28	19.51	18.14	40.45

TABLE IV.- PRESSURE AND HEAT-TRANSFER DATA – Continued

(a) Pressures – Concluded

Orifice	p/p_∞ for –								
	Case 11	Case 12	Case 13	Case 14	Case 15	Case 16	Case 17	Case 18	Case 19
1	-----	-----	7.879	6.94	5.584	21.10	37.64	22.56	19.82
2	122.93	115.62	7.748	6.91	5.566	25.73	40.38	25.34	21.12
3	110.08	-----	6.663	5.95	4.785	18.95	37.53	20.12	16.96
4	109.30	61.57	6.202	5.53	4.464	15.92	32.76	17.85	14.99
5	65.53	61.54	6.034	5.40	4.341	14.36	29.64	15.75	13.80
6	59.42	54.76	5.804	5.22	4.187	12.36	24.95	14.54	13.05
7	-----	-----	----	---	----	----	----	----	----
8	-----	-----	6.028	5.37	4.305	18.29	29.04	17.39	14.93
9	105.74	101.30	6.070	5.38	4.328	19.62	30.26	18.31	14.35
10	100.99	-----	5.611	5.01	4.057	13.26	32.16	14.89	12.80
11	85.27	54.98	5.289	4.68	3.840	13.15	24.68	13.80	11.77
12	55.37	54.31	5.194	4.59	3.730	12.10	22.57	12.53	10.82
13	54.79	52.23	5.118	4.54	3.678	11.32	20.80	11.86	10.45
14	-----	-----	6.136	5.09	4.42	13.76	21.59	12.74	10.98
15	-----	-----	5.594	4.66	4.08	14.11	22.09	13.01	11.24
16	-----	-----	5.620	4.56	4.19	14.89	22.34	13.36	11.57
17	98.83	94.23	5.587	4.57	4.29	13.78	22.81	12.57	10.12
18	-----	-----	5.660	4.56	4.39	10.75	24.68	11.67	9.99
19	87.93	-----	5.290	4.21	4.18	10.26	17.74	10.54	9.11
20	50.53	50.95	----	4.07	4.14	9.89	17.15	10.04	8.63
21	49.37	47.82	4.636	4.06	3.38	8.98	15.52	9.09	7.09
22	47.95	46.27	5.015	4.01	3.34	8.60	14.70	8.70	7.36
23	-----	-----	5.387	5.28	4.61	11.56	17.42	10.65	8.22
24	-----	-----	5.304	4.67	3.98	11.56	17.39	10.60	8.35
25	-----	-----	5.182	6.30	5.28	13.03	17.37	12.55	8.52
26	96.73	100.30	5.092	4.18	3.48	12.38	17.42	10.67	7.72
27	94.10	92.29	5.385	4.18	3.47	8.29	18.18	9.06	7.07
28	84.63	72.61	----	3.86	3.25	8.14	17.66	8.46	6.65
29	80.32	67.34	5.147	4.75	3.30	8.31	13.88	8.52	6.70
30	58.84	49.79	5.185	3.83	3.19	7.98	13.50	----	6.43
31	50.17	48.91	4.853	3.68	3.08	7.60	12.73	7.66	6.08
32	-----	-----	6.267	3.81	3.17	10.45	14.69	9.16	7.57
33	94.22	99.46	6.460	3.82	3.16	10.04	15.09	9.27	6.31
34	76.47	64.49	----	3.48	2.90	6.85	11.03	6.96	5.73
35	68.55	51.42	----	3.47	2.90	6.72	10.94	6.76	5.60
36	47.32	47.99	----	3.52	2.93	6.58	10.46	5.59	----
37	45.85	43.38	5.799	3.57	2.92	6.34	9.86	6.32	5.36

TABLE IV.- PRESSURE AND HEAT-TRANSFER DATA – Continued

(b) Heat-transfer data from reference 4

Thermocouple	q/q_e for –					
	Case 1	Case 2	Case 3	Case 4	Case 5	Case 6
1	----	-----	----	----	0.748	1.036
2	----	-----	0.970	----	----	1.718
3	----	-----	----	----	----	.414
4	----	-----	.987	----	----	.858
5	0.736	-----	.907	----	----	1.374
6	.640	0.512	.755	----	----	-----
7	.847	1.050	.968	1.070	.984	.928
8	1.035	1.070	.897	.835	----	.922
9	.543	.809	.922	----	----	-----
10	.170	.153	.660	1.419	----	1.380
11	.838	.958	1.027	.975	1.016	.928
12	.867	-----	1.090	.797	.884	.754
13	----	-----	.754	.473	.708	.532
14	.486	-----	----	----	----	-----
15	.712	.975	.962	1.072	1.038	.846
16	----	.698	.783	.599	.740	.468
17	----	.273	----	.604	.924	.824
18	----	-----	----	----	----	-----
19	1.040	-----	0.977	.877	.970	.814
20	----	-----	.774	4.800	.758	.480
21	----	-----	----	2.917	3.196	3.132
22	2.378	2.271	1.578	3.226	4.096	4.282
23	.769	.895	.868	.722	.822	.642
24	.636	.583	.833	2.793	2.852	3.432
25	2.640	2.514	2.068	3.423	3.560	4.304
26	2.016	-----	2.630	2.520	3.382	4.488
27	----	-----	1.118	2.247	2.586	2.764
28	3.215	-----	1.669	2.515	3.100	3.260
29	4.133	-----	2.380	4.678	4.850	4.734
30	5.691	-----	3.730	6.762	6.766	8.114
31	4.928	-----	3.604	5.870	.314	-----
32	5.054	7.073	4.365	4.946	----	6.662
33	----	8.085	4.338	5.499	6.550	12.00
34	7.816	-----	5.242	5.088	6.814	11.50
35	7.204	-----	5.943	6.471	9.436	13.08
36	----	11.65	6.593	7.661	9.792	11.22
37	----	-----	----	----	----	-----

TABLE IV.- PRESSURE AND HEAT-TRANSFER DATA – Continued

(c) *Heat-transfer data from present tests*

Thermocouple	h, W/m^2-K, for –						
	Case 7	Case 8	Case 9	Case 10	Case 11	Case 12	Case 13
1	13.506	7.569	0.528	11.415	54.420	38.507	42.86
2	19.546	5.627	10.106	24.697	43.900	31.112	----
3	1.517	8.964	3.383	6.478	17.877	12.710	----
4	31.786	37.567	28.395	89.515	120.525	63.674	----
5	17.693	14.669	8.120	117.808	84.654	34.401	----
6	11.466	48.905	24.943	------	------	------	----
7	35.606	51.785	46.535	72.479	79.873	65.247	----
8	22.001	19.523	14.778	38.262	25.494	5.630	----
9	1.059	6.135	6.594	------	------	------	----
10	17.650	51.519	50.682	31.377	20.358	2.886	----
11	35.586	46.964	39.978	66.718	75.890	60.937	8.71
12	20.071	33.032	.323	27.108	59.466	23.982	9.49
13	14.690	58.731	49.374	60.140	146.387	65.043	16.13
14	35.892	120.34	11.652	------	------	------	11.06
15	31.623	30.826	27.231	55.891	44.227	32.950	6.67
16	17.335	58.077	37.976	51.846	174.884	78.954	----
17	38.078	169.84	47.046	134.682	134.600	18.295	31.38
18	------	------	------	------	------	------	30.72
19	23.431	76.993	3.751	41.326	110.781	57.239	28.54
20	38.670	202.99	102.589	116.358	246.975	90.435	7.61
21	35.402	106.45	106.552	150.330	145.692	53.828	14.52
22	74.583	65.145	5.940	92.008	72.989	------	9.63
23	54.849	276.391	134.335	131.556	399.776	165.426	4.64
24	159.216	122.098	85.328	107.656	138.461	119.483	----
25	136.030	73.643	31.051	211.226	100.199	30.335	----
26	102.712	62.060	7.117	174.477	110.086	55.217	15.41
27	------	------	------	------	------	------	29.36
28	120.362	80.180	60.835	246.566	156.009	137.092	13.86
29	84.041	66.064	25.412	144.835	155.947	135.581	18.25
30	69.905	57.382	21.470	132.230	175.395	153.659	5.75
31	117.767	88.739	85.655	350.749	12.706	196.456	5.06
32	74.480	63.388	53.521	189.797	119.953	156.172	----
33	58.424	53.419	33.808	212.860	115.153	153.149	6.69
34	46.637	41.734	32.501	194.638	94.316	123.406	7.88
35	51.376	44.084	6.169	228.181	96.502	86.022	12.72
36	49.640	35.851	------	225.525	80.854	37.567	17.33
37	48.517	27.782	------	226.955	65.880	31.806	----

TABLE IV.- PRESSURE AND HEAT-TRANSFER DATA – Concluded

(c) Heat-transfer data from present tests – Concluded

Thermocouple	h, W/m^2-K, for –					
	Case 14	Case 15	Case 16	Case 17	Case 18	Case 19
1	----	66.60	------	------	------	------
2	8.71	-----	13.726	10.518	18.559	13.527
3	10.37	7.26	------	3.667	3.526	------
4	9.00	14.40	13.421	22.818	25.494	8.743
5	12.32	9.54	5.328	6.596	12.692	13.356
6	6.55	12.75	2.075	22.593	8.282	6.020
7	12.82	13.29	27.332	40.488	44.287	35.238
8	38.89	109.02	14.522	14.837	23.819	25.290
9	----	-----	9.268	26.985	9.887	11.045
10	12.87	14.69	11.709	49.885	21.756	6.461
11	8.84	9.68	22.470	38.343	39.487	31.582
12	7.91	13.19	11.846	18.802	21.204	16.418
13	3.39	10.94	15.529	51.458	24.023	7.761
14	3.31	4.19	14.796	107.369	40.979	12.861
15	8.50	11.38	27.374	23.329	40.795	34.666
16	----	-----	23.982	74.092	15.989	7.182
17	31.28	40.28	------	------	.995	19.991
18	25.90	46.35	35.708	59.936	21.204	44.267
19	14.91	18.20	23.431	69.067	27.231	24.554
20	1.67	10.19	24.697	135.193	84.817	27.925
21	----	-----	66.085	71.396	102.099	68.454
22	----	18.58	73.786	47.087	56.422	75.788
23	7.05	8.47	46.024	203.299	103.938	32.542
24	----	-----	108.350	77.872	111.087	120.81
25	----	-----	68.761	45.228	60.446	79.444
26	4.87	7.84	48.986	28.660	40.182	44.819
27	33.13	44.41	------	------	------	------
28	14.62	32.97	63.286	52.091	57.546	69.659
29	18.74	18.07	38.139	30.376	45.636	------
30	.08	8.92	29.825	24.493	8.089	27.333
31	3.85	21.82	75.277	72.029	76.830	------
32	----	----	49.497	47.761	53.991	49.048
33	1.59	7.63	31.838	31.888	44.043	29.559
34	8.71	11.07	26.373	26.107	29.702	26.516
35	9.70	10.97	24.105	19.104	29.212	16.700
36	5.28	8.76	14.678	8.892	46.126	20.301
37	----	-----	12.277	6.367	7.644	3.873

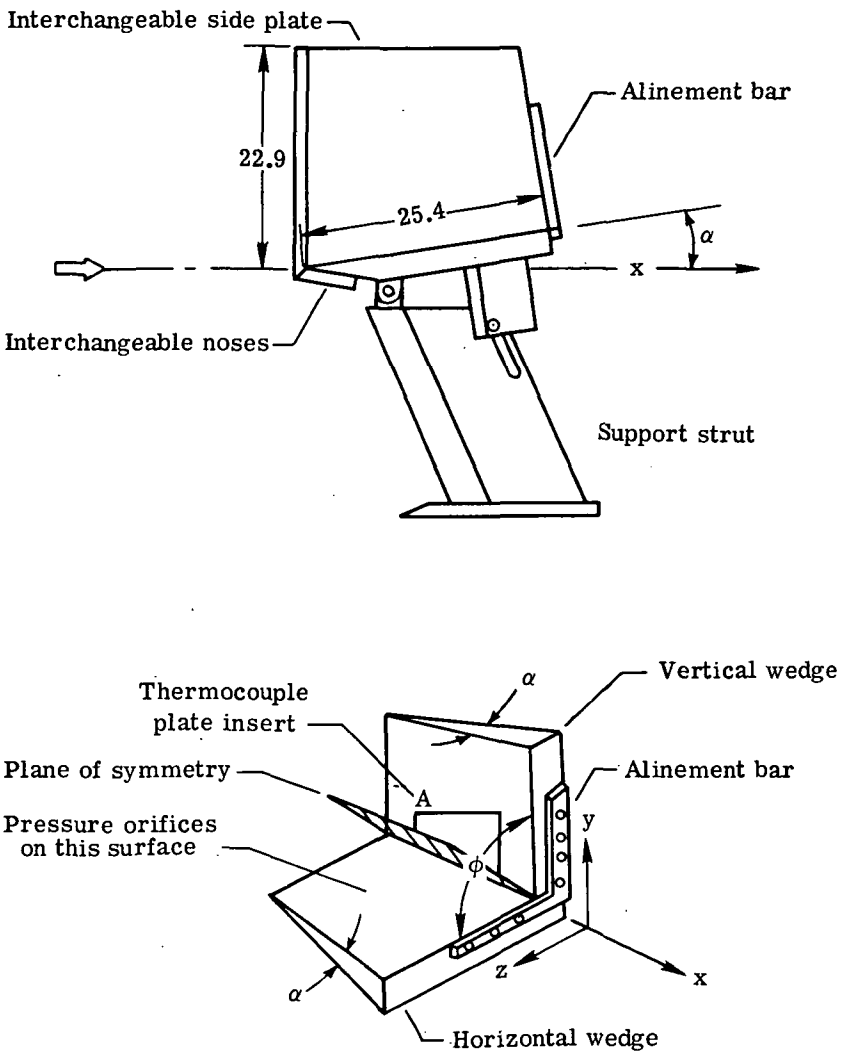

(a) Model sketch showing dimensions and coordinate system.

Figure 1.- Model. (Linear dimensions are in cm.)

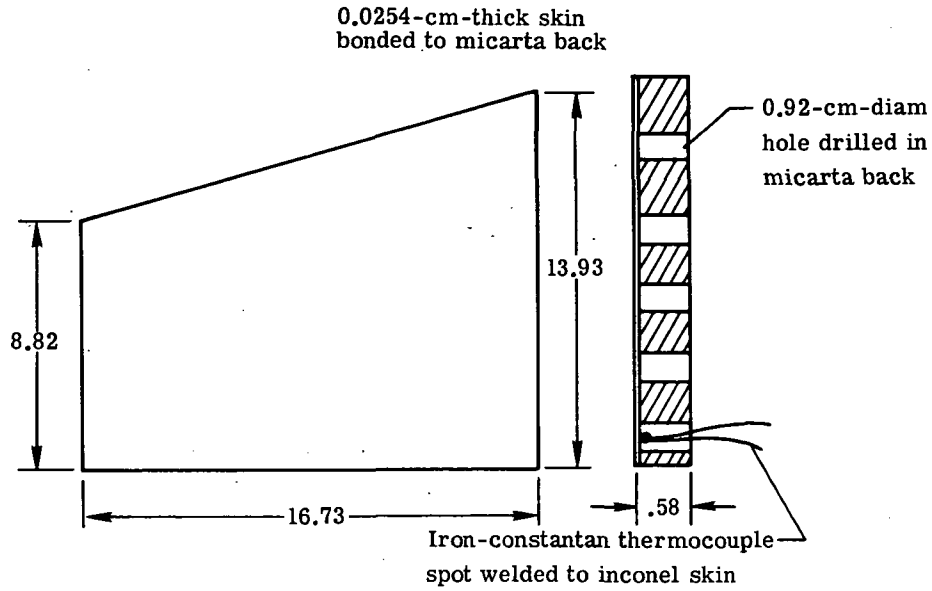

(b) Heat-transfer insert. (See table II for thermocouple locations.)

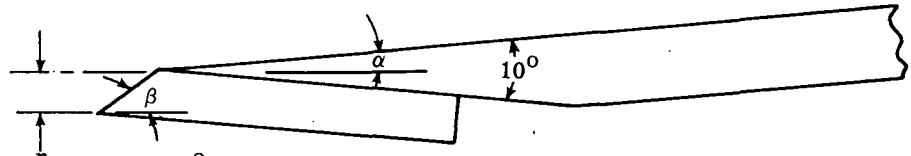

Nose	β, deg	r, cm	C_D
1	20	0.30	0.37
2	36	0.30	1.08
3	90	0.08	1.76
4	90	0.15	1.76

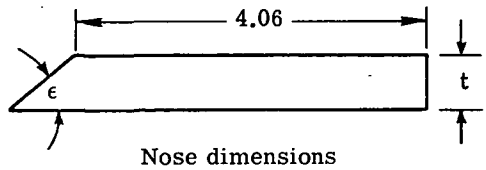

α, deg	Dimension	Nose			
		1	2	3	4
0	t, cm	0.44	0.37	0.15	0.30
	ϵ, deg. . . .	30	46	100	100
5	t, cm	0.38	0.34	0.15	0.30
	ϵ, deg	25	41	95	95
10	t, cm. . . .	0.30	0.30	0.15	0.30
	ϵ, deg. . . .	20	36	90	90

(c) Noses.

Figure 1.- Concluded.

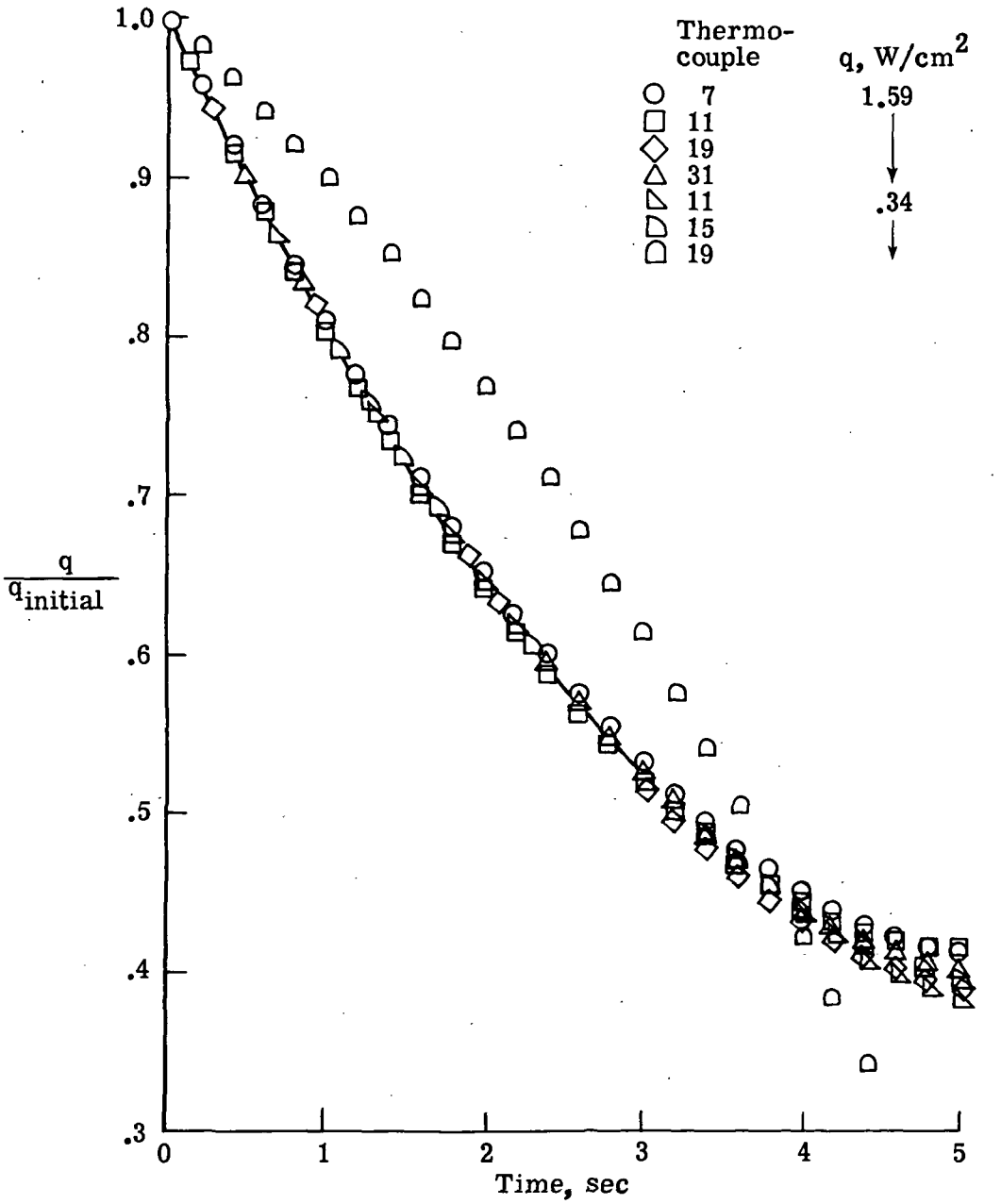

Figure 2.- Thermocouple-plate calibration.

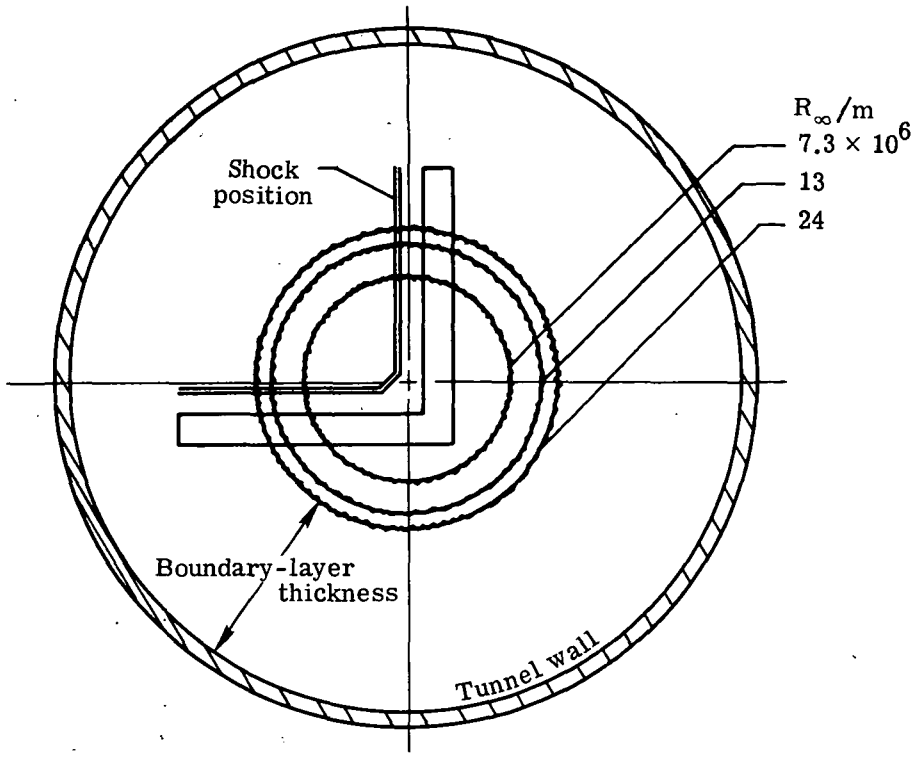

5^o wedge model to scale in tunnel

Instrumentation within tunnel boundary layer

α, deg	R_∞/m	Orifice	Thermocouple
0	7.3×10^6	None	1,2,3,4,5,6,7,8,9,10
	13		1
	24		None
5	7.3×10^6	37	1, 2, 3
	13	None	None
	24	None	None
10	7.3×10^6	37	1,2,3,4,5,6
	13	None	None
	24	None	None

Figure 3.- Tunnel-wall boundary-layer influence on models in Langley 22-inch helium tunnel.

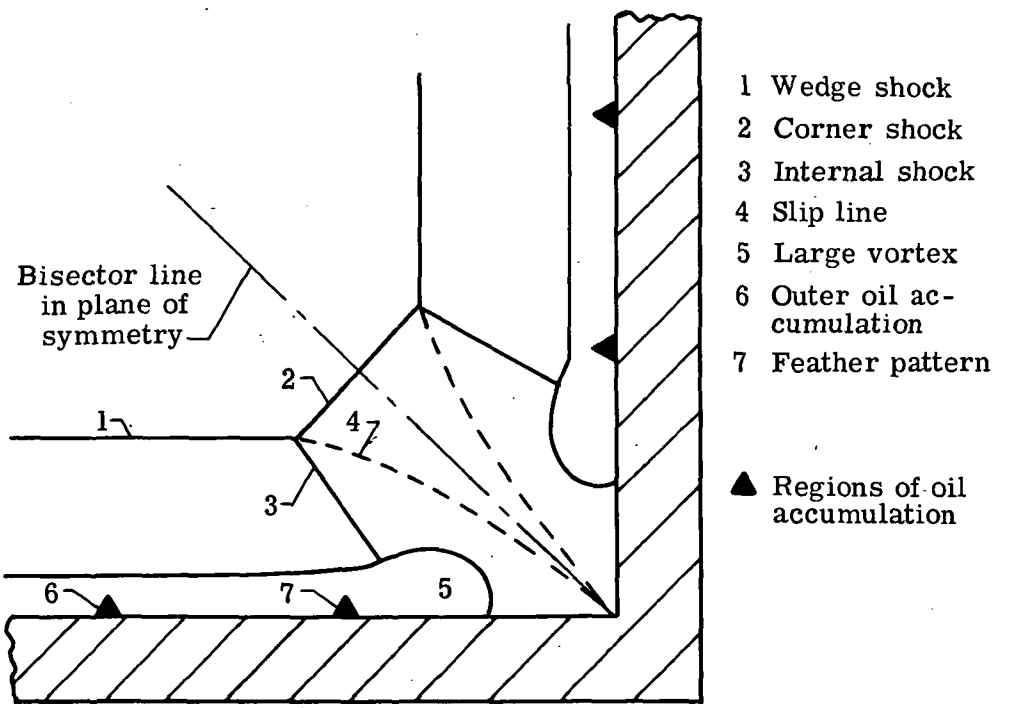

Figure 4.- Flow field in the base plane.

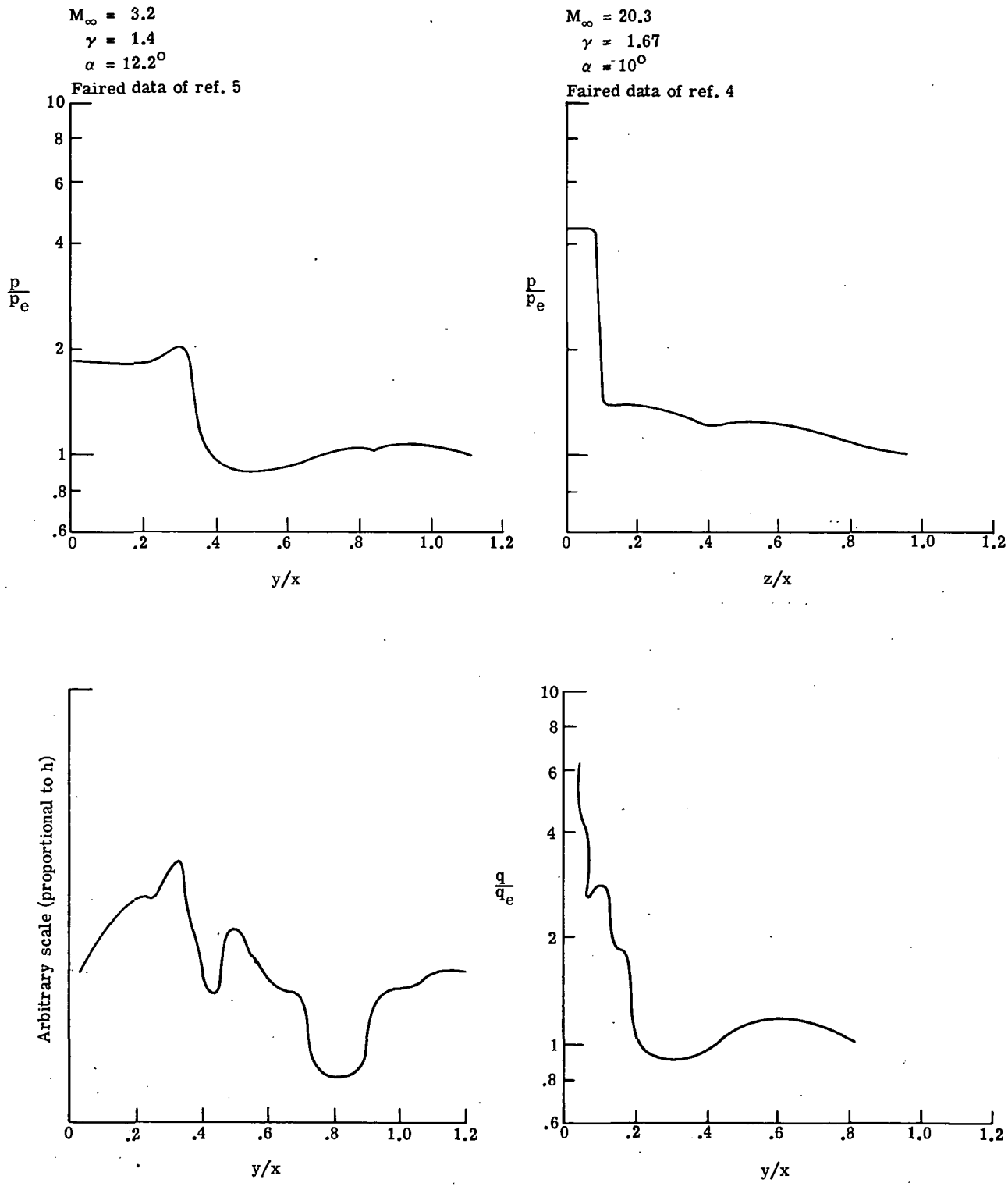

Figure 5.- Corner pressures and heat transfer at Mach 3.2 and Mach 20.3.

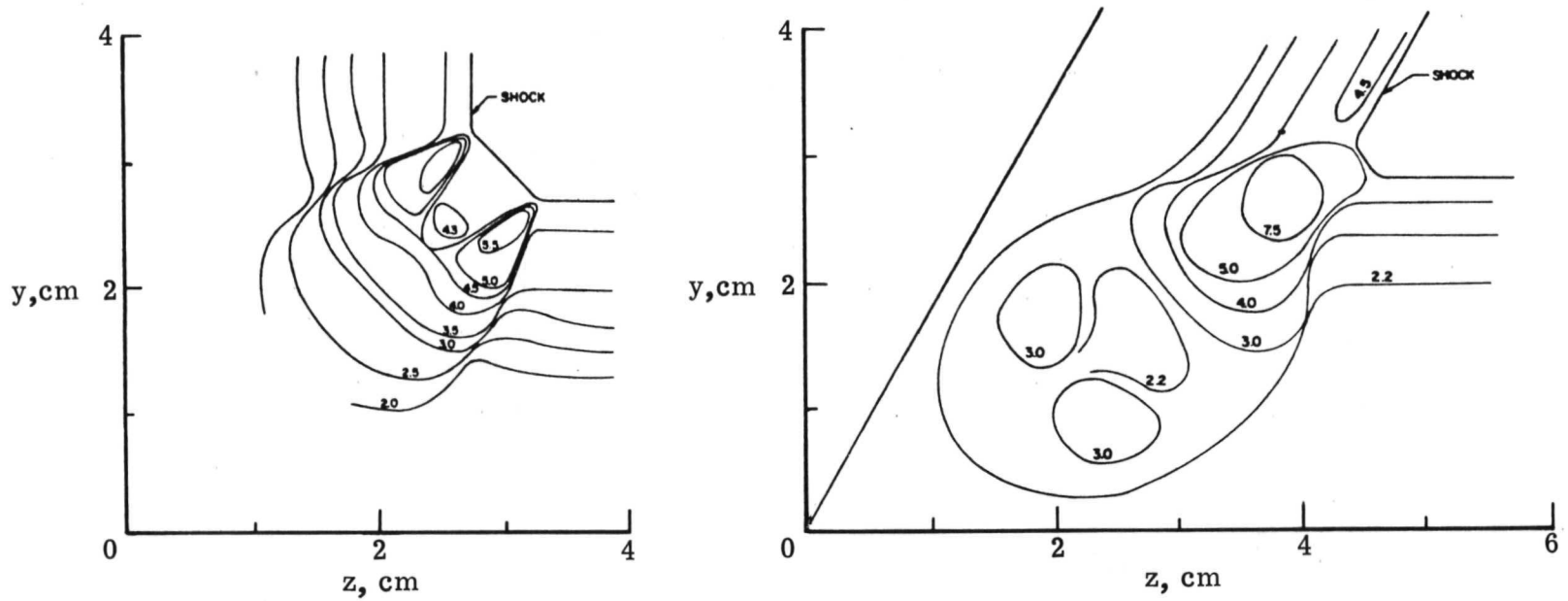

(a) $\phi = 90^{o}$; $\overline{\chi} = 5$.

(b) $\phi = 60^{o}$; $\overline{\chi} = 5$.

Figure 6.- Flow-field surveys on intersecting plates at Mach 11.2 – data of reference 12. (Numbers denote ratio of pitot to stagnation pressure × 1000.)

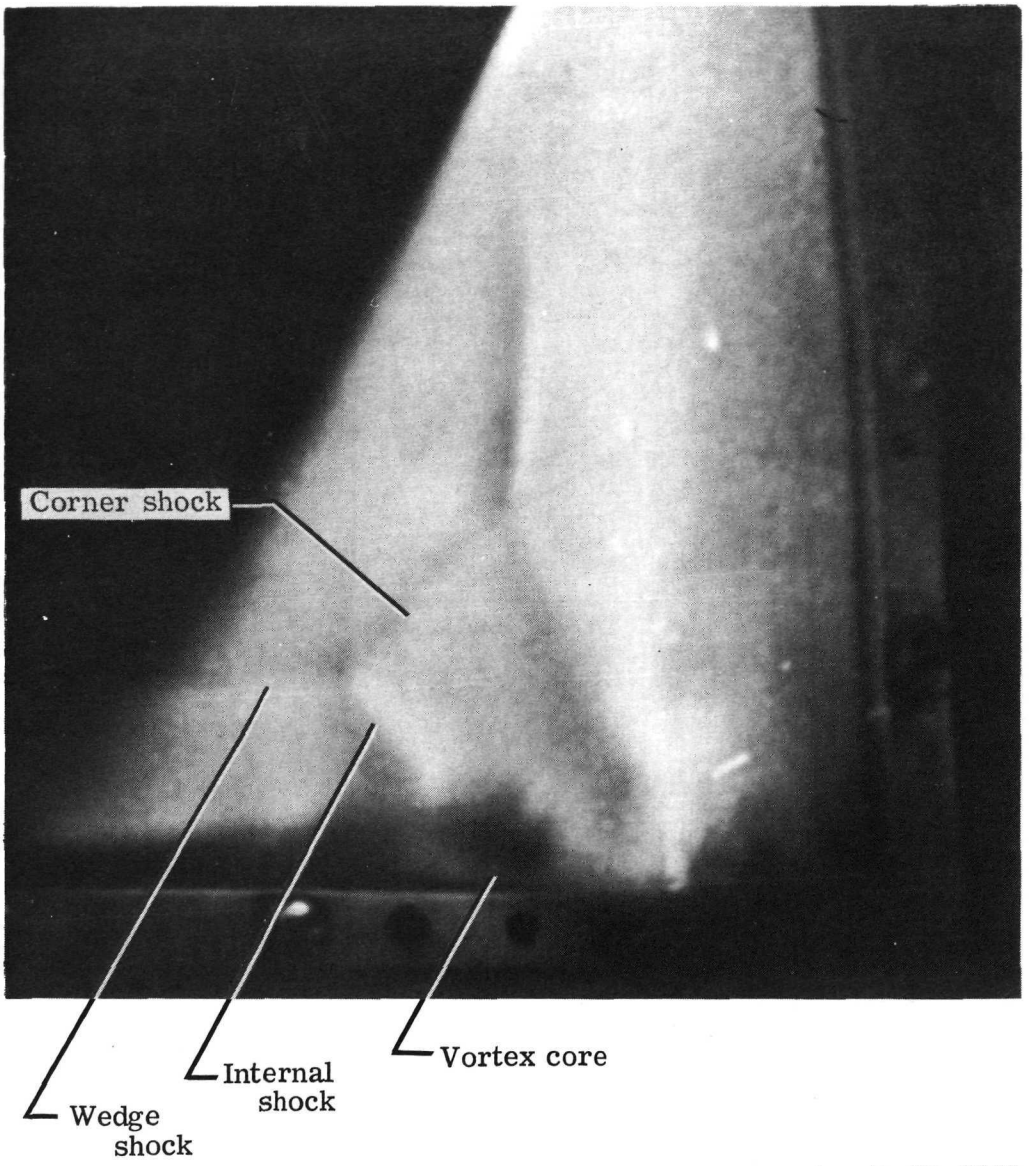

L-73-8010

Figure 7.- Electron-beam visualization of flow on 10^{o} wedge corner at Mach 20 (from ref. 4). $R_{\infty}/m = 1.3 \times 10^{7}$.

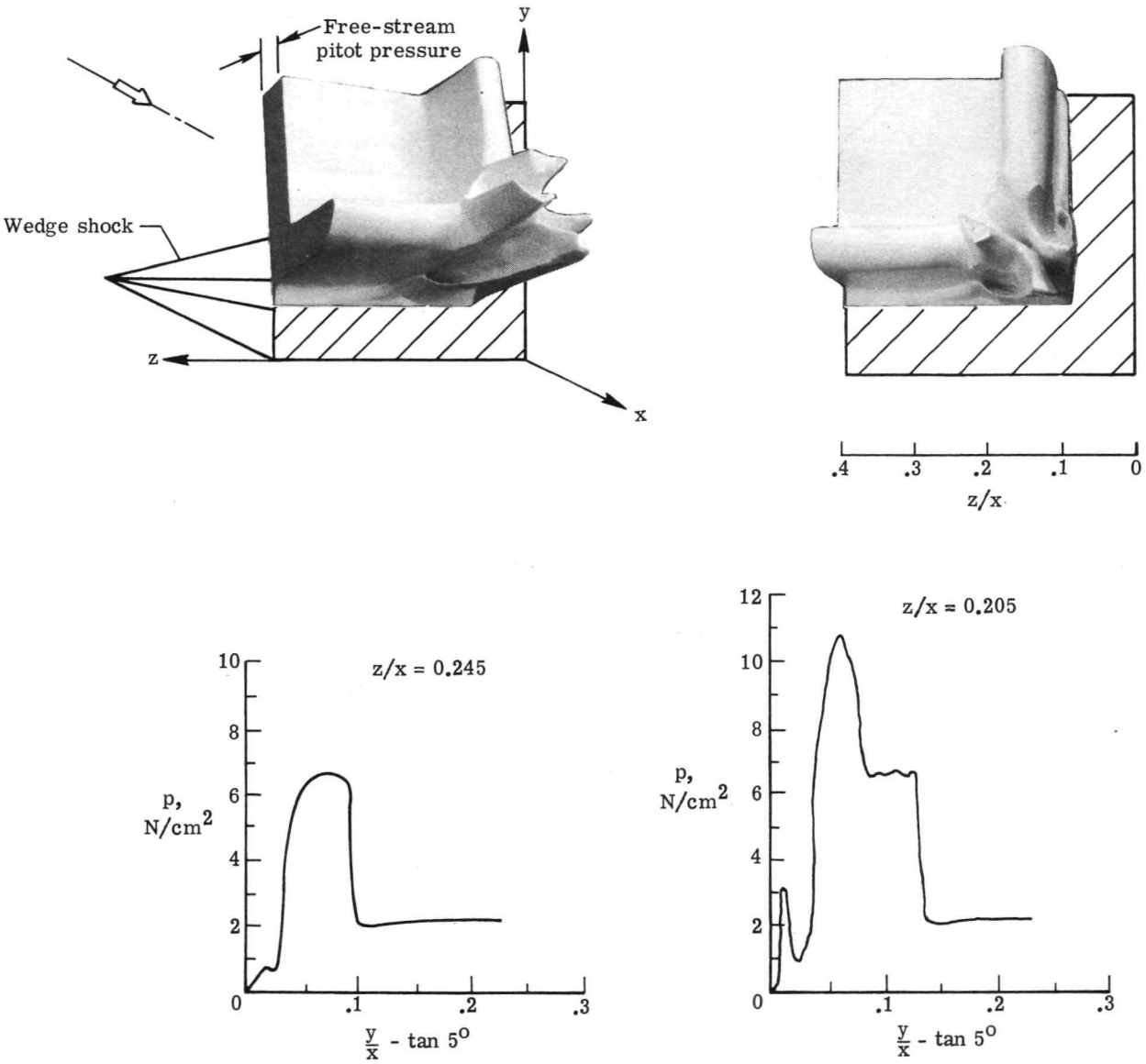

L-73-8011

Figure 8.- Model of pitot-pressure distribution in flow field of 5° wedge corner (data of ref. 4).

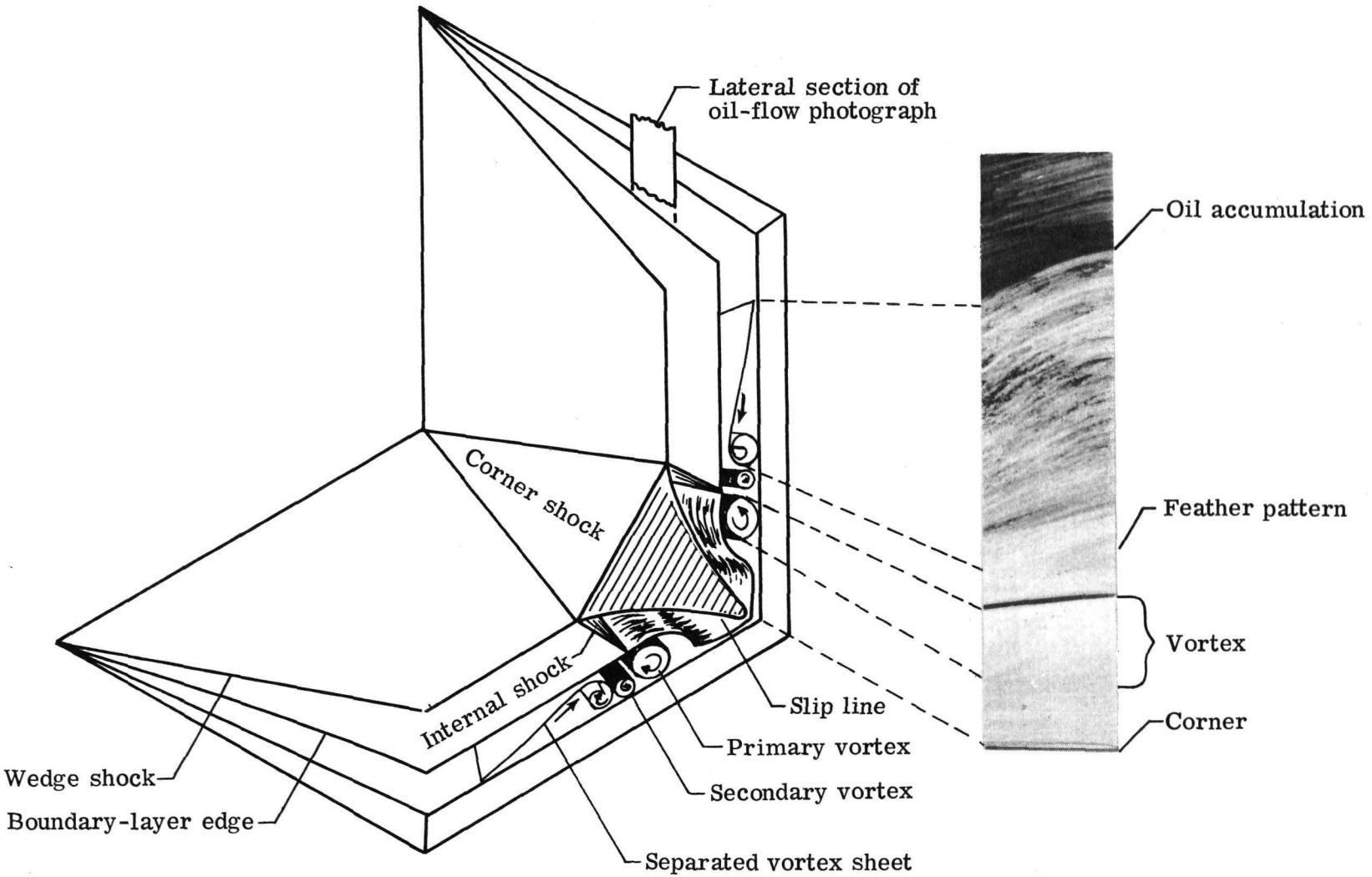

L-73-8012

Figure 9.- Possible flow structure within viscous region.

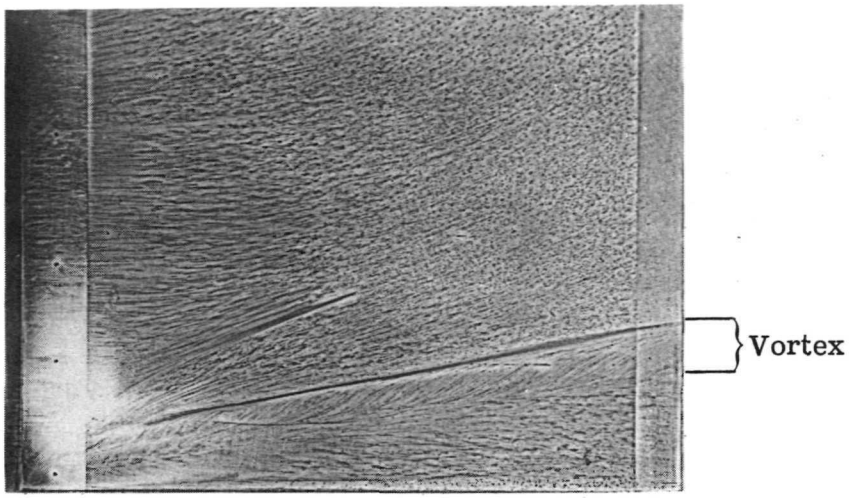

(a) $\alpha = 0^{o}$; 20^{o} nose.

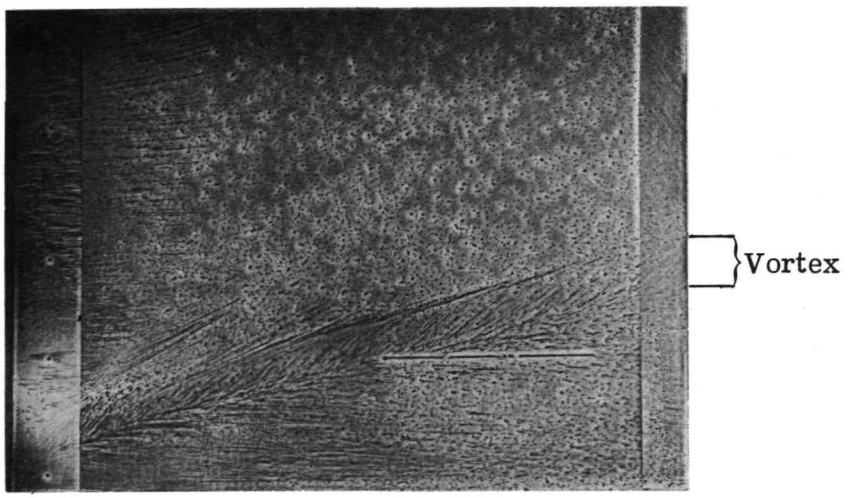

(b) $\alpha = 0^{o}$; 36^{o} nose.

L-73-8013

Figure 10.- Oil-flow photographs. $M_{\infty} = 20.3$; $R_{\infty}/m = 1.3 \times 10^{7}$.

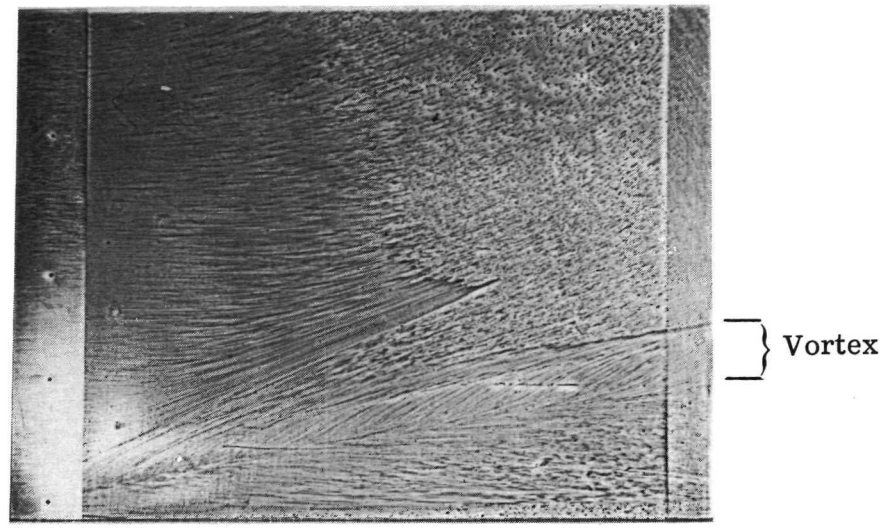

(c) $\alpha = 0^{o}$; flat nose; r = 0.08 cm.

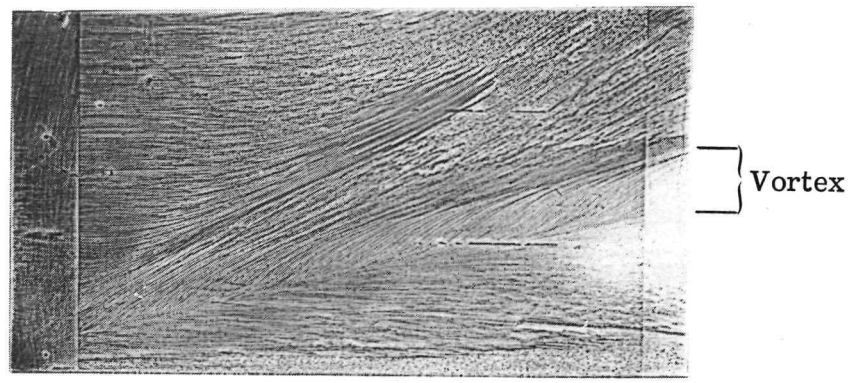

(d) $\alpha = 0^{o}$; flat nose; r = 0.15 cm.

L-73-8014

Figure 10.- Continued.

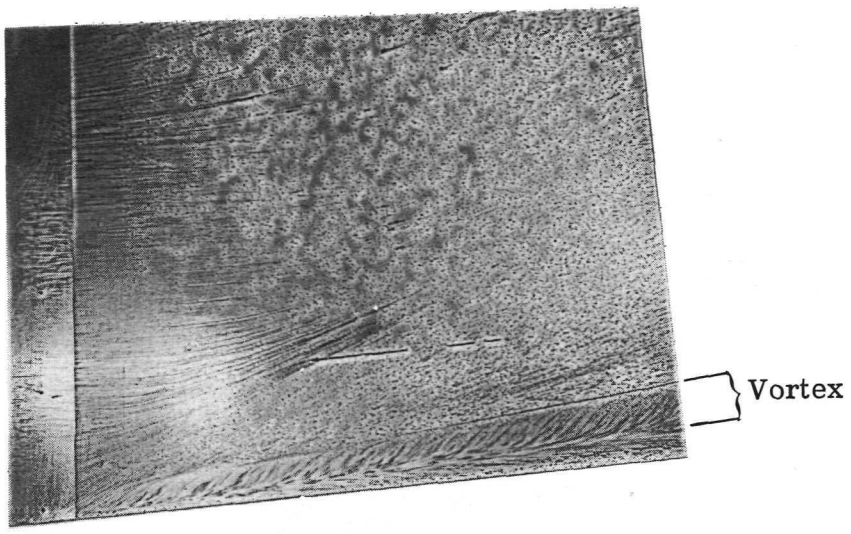

(e) $\alpha = 5^{o}$; sharp nose.

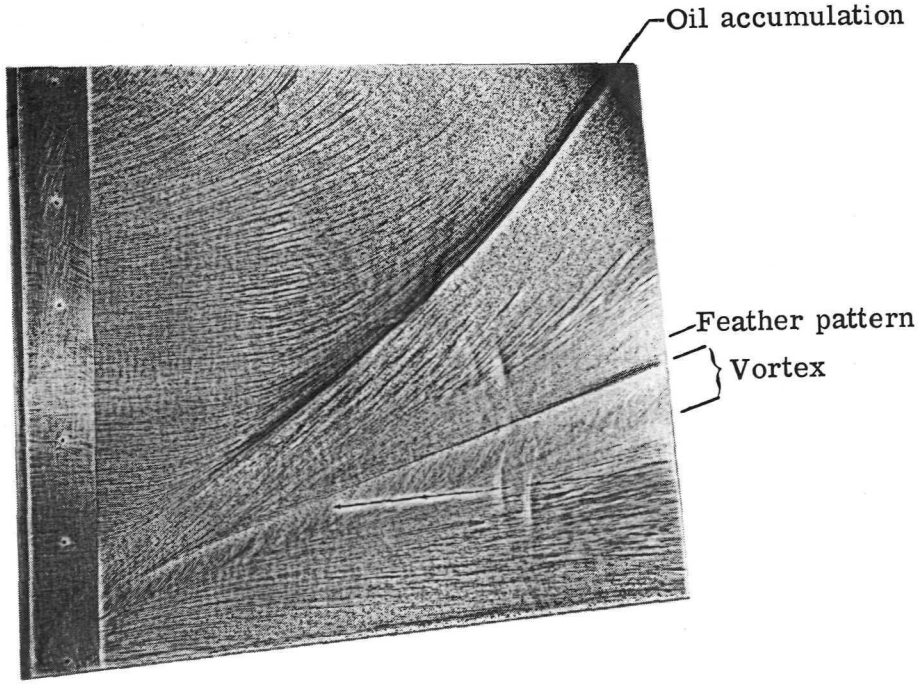

(f) $\alpha = 5^{o}$; 36^{o} nose.

L-73-8015

Figure 10.- Continued.

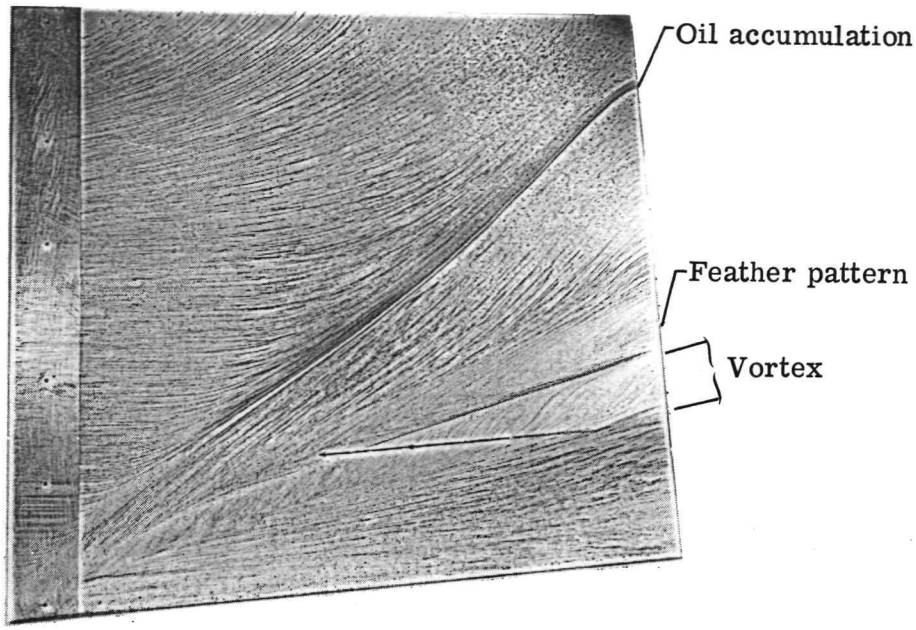

(g) $\alpha = 5^{o}$; flat nose; r = 0.15 cm.

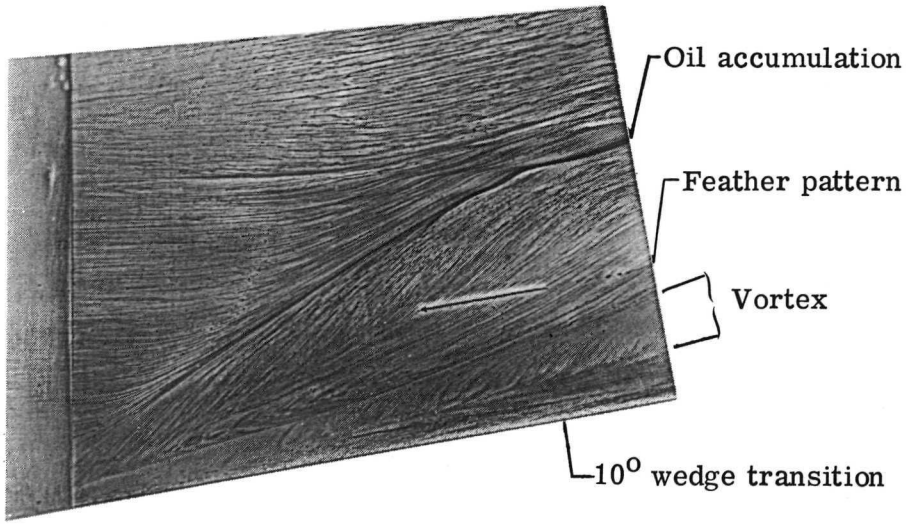

(h) $\alpha = 10^{o}$; sharp nose.

L-73-8016

Figure 10.- Continued.

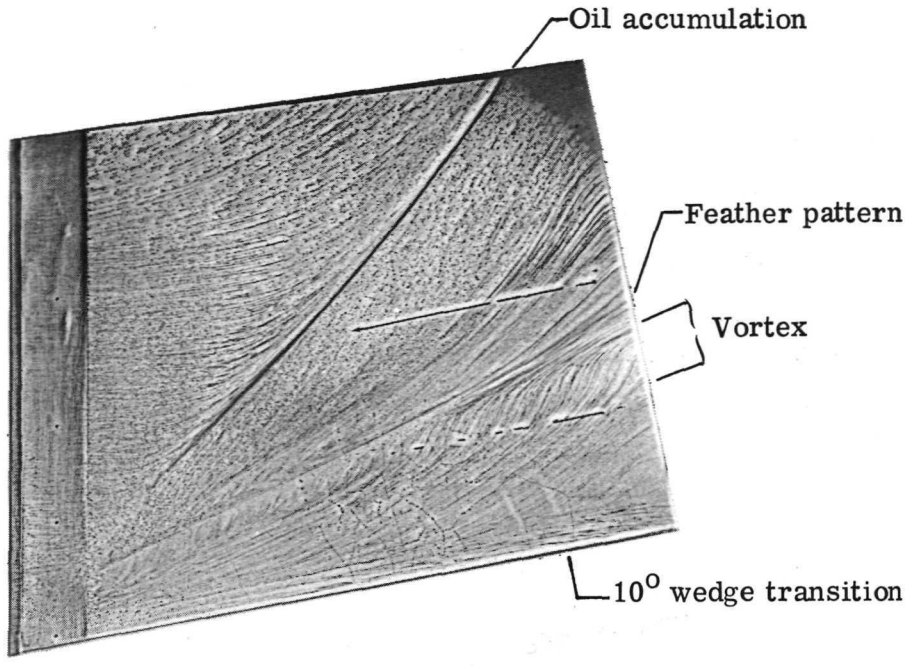

(i) $\alpha = 10^{\circ}$; 36° nose.

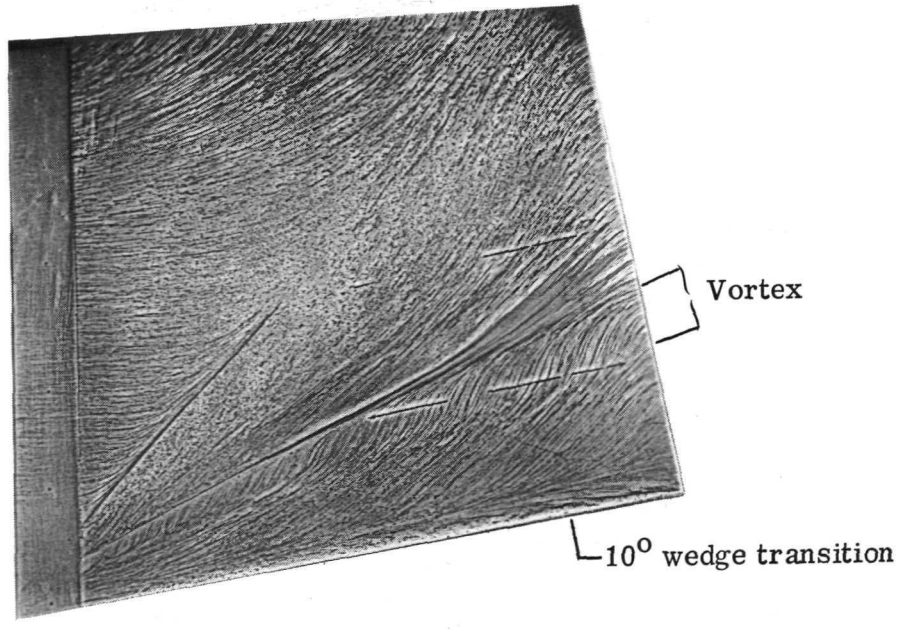

(j) $\alpha = 10^{\circ}$; flat nose; r = 0.15 cm.

L-73-8017

Figure 10.- Concluded.

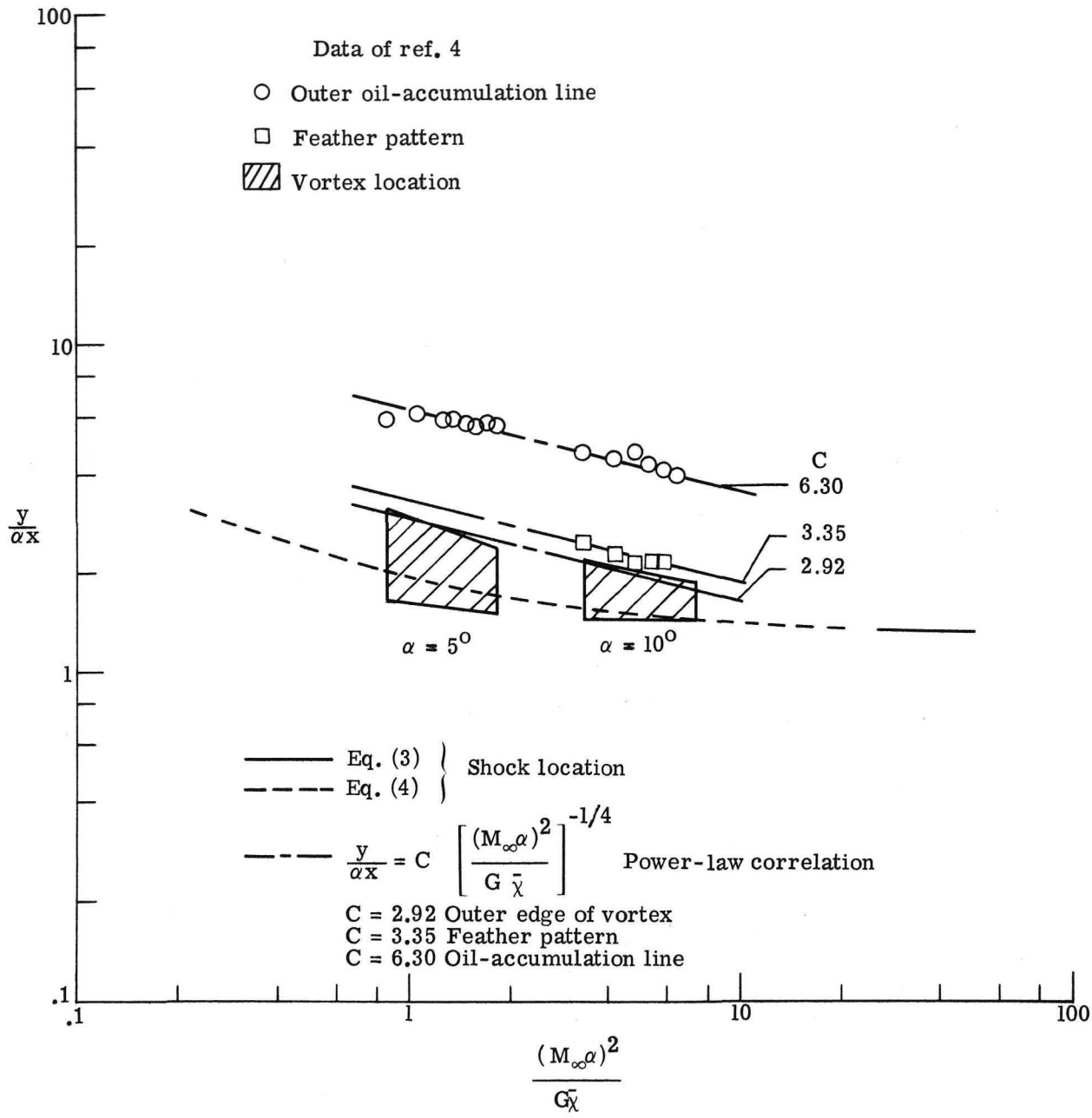

Figure 11.- Oil-flow correlation for sharp-wedge corners.

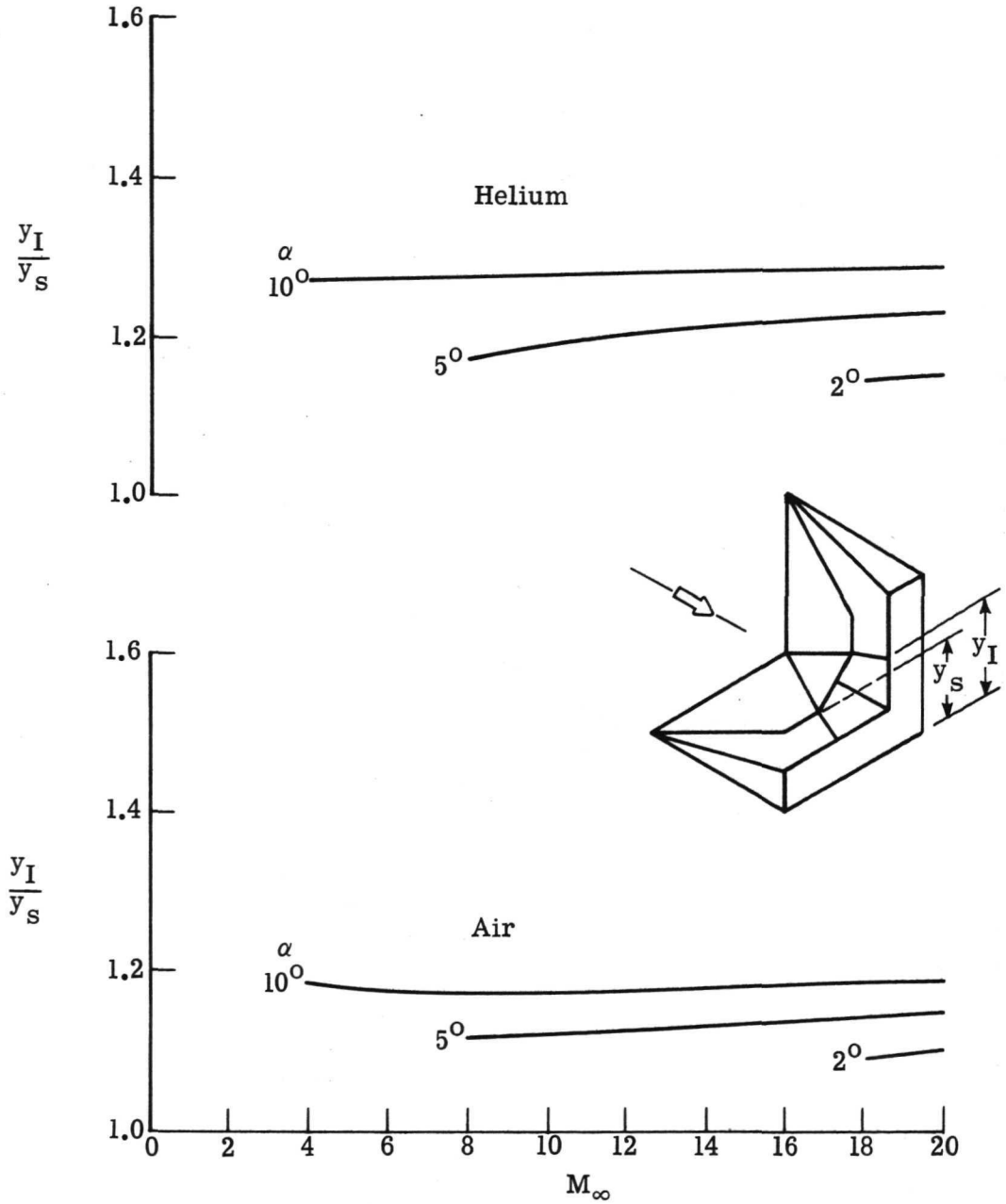

Figure 12.- Location of internal shock from two-shock method.

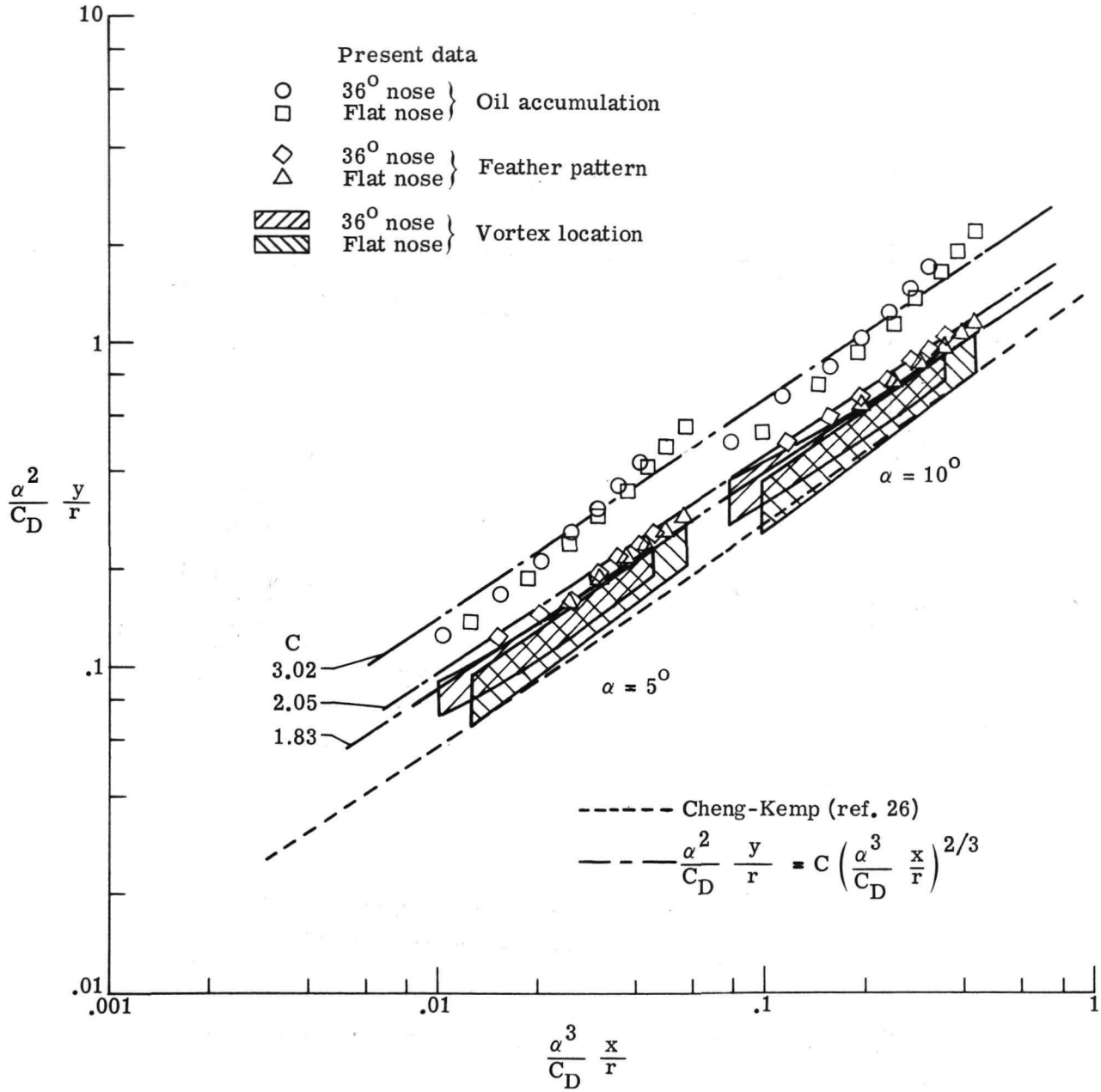

Figure 13.- Oil-flow correlation for blunt-wedge corners.

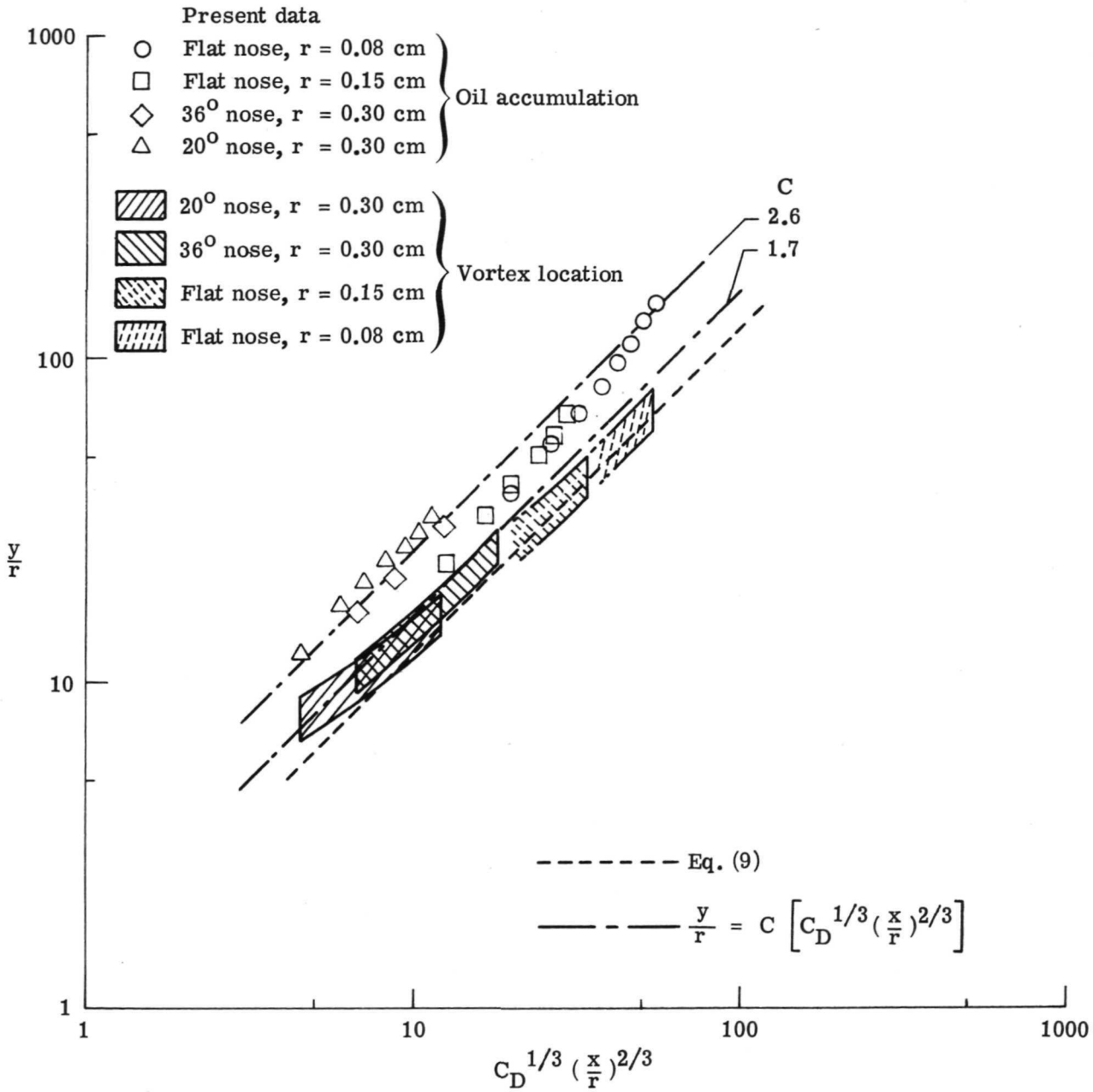

Figure 14.- Oil-flow correlation for blunt-plate corners.

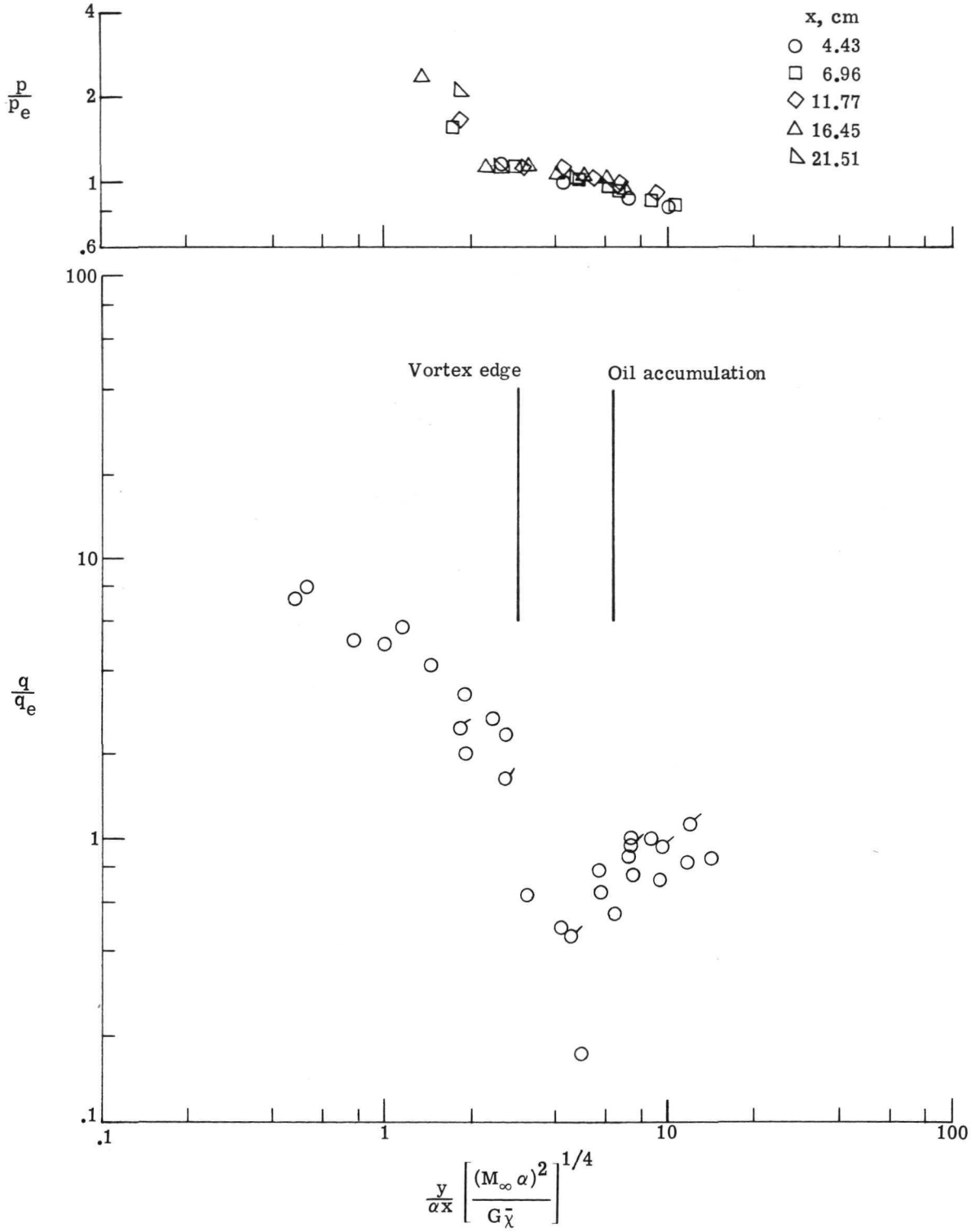

(a) Case 1; $\alpha = 5^{o}$; sharp nose.

Figure 15.- Pressures and heat transfer on sharp-wedge corners. (Flagged symbols denote reruns.)

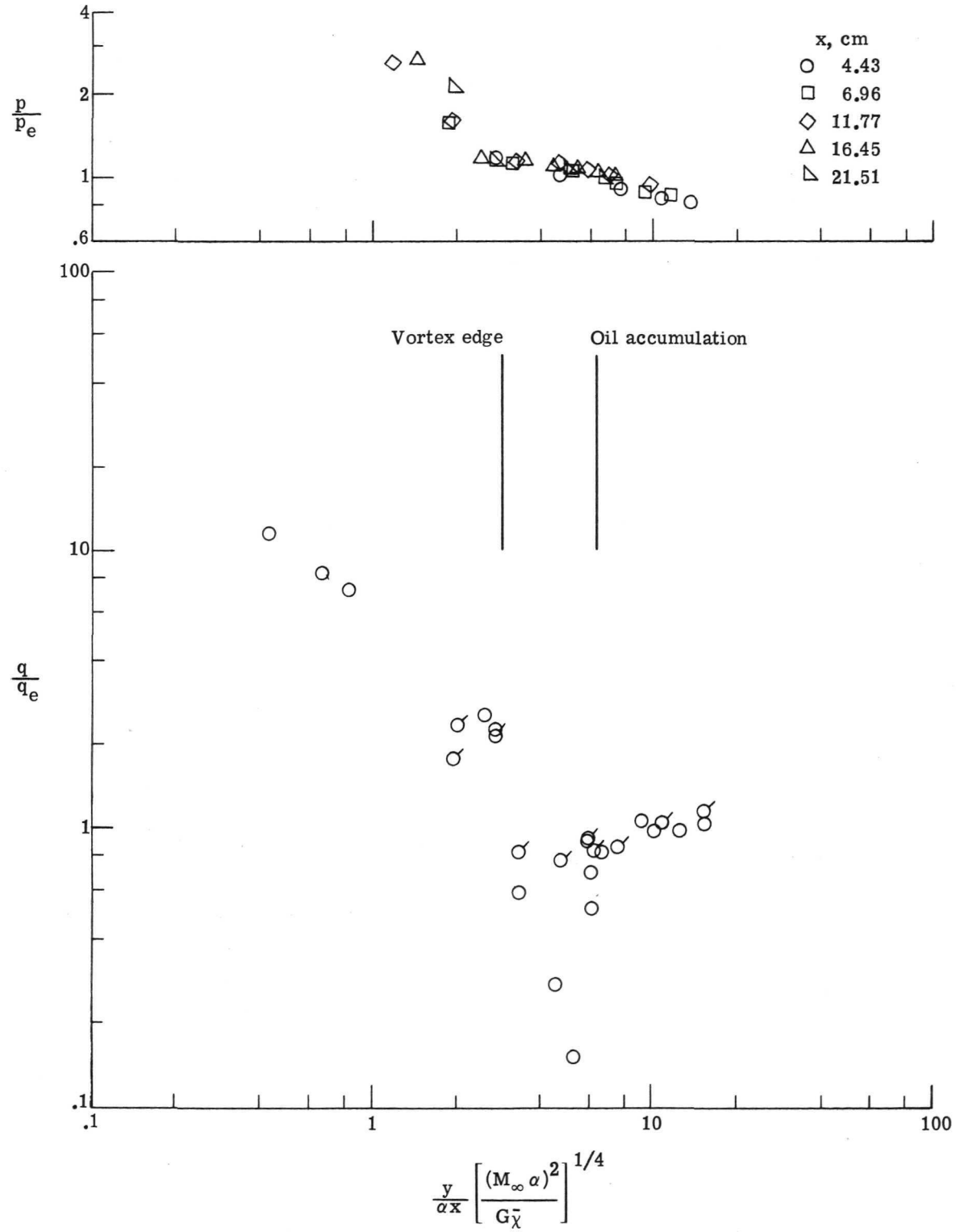

(b) Case 2; $\alpha = 5^{o}$; sharp nose.

Figure 15.- Continued.

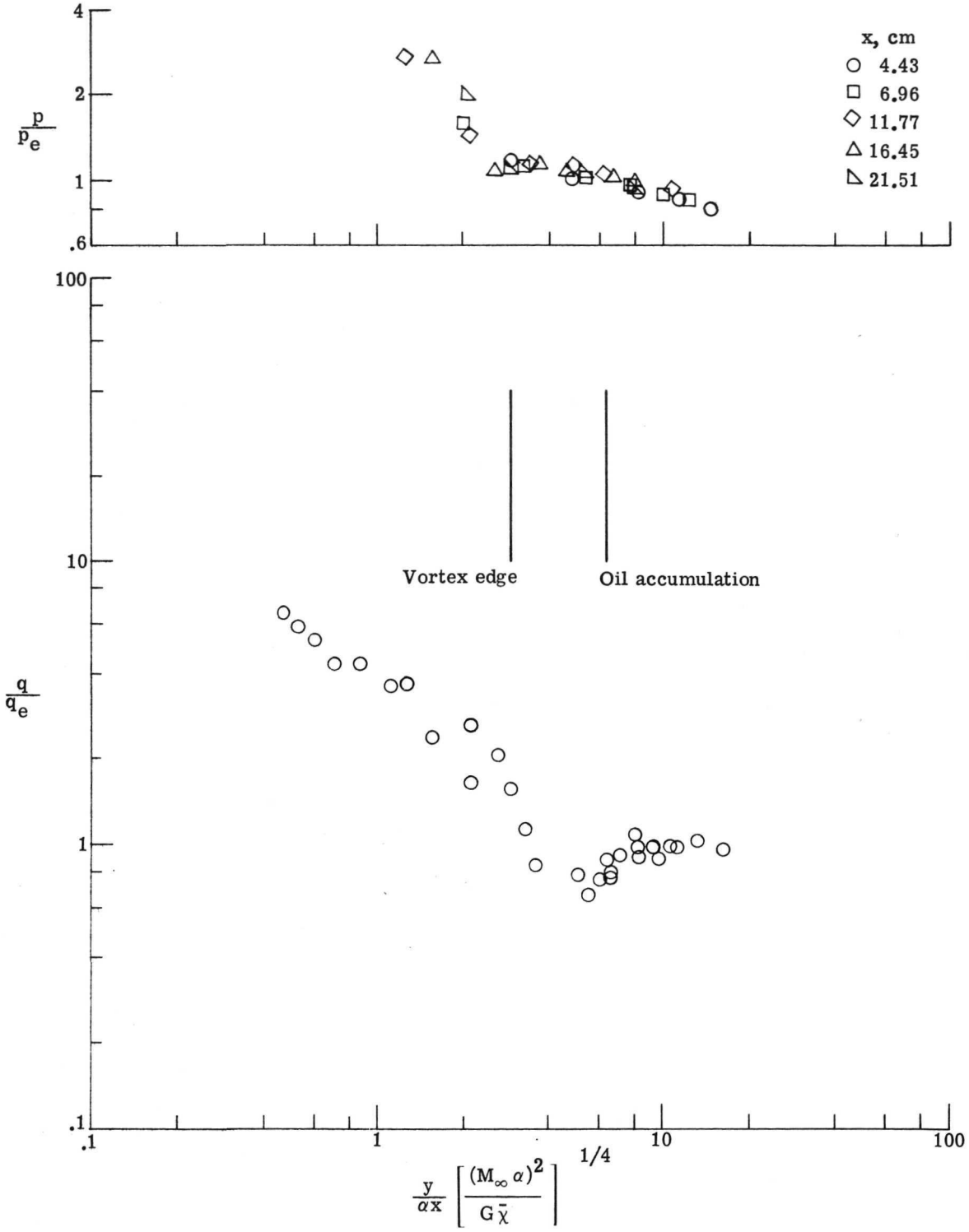

(c) Case 3; $\alpha = 5^{o}$; sharp nose.

Figure 15.- Continued.

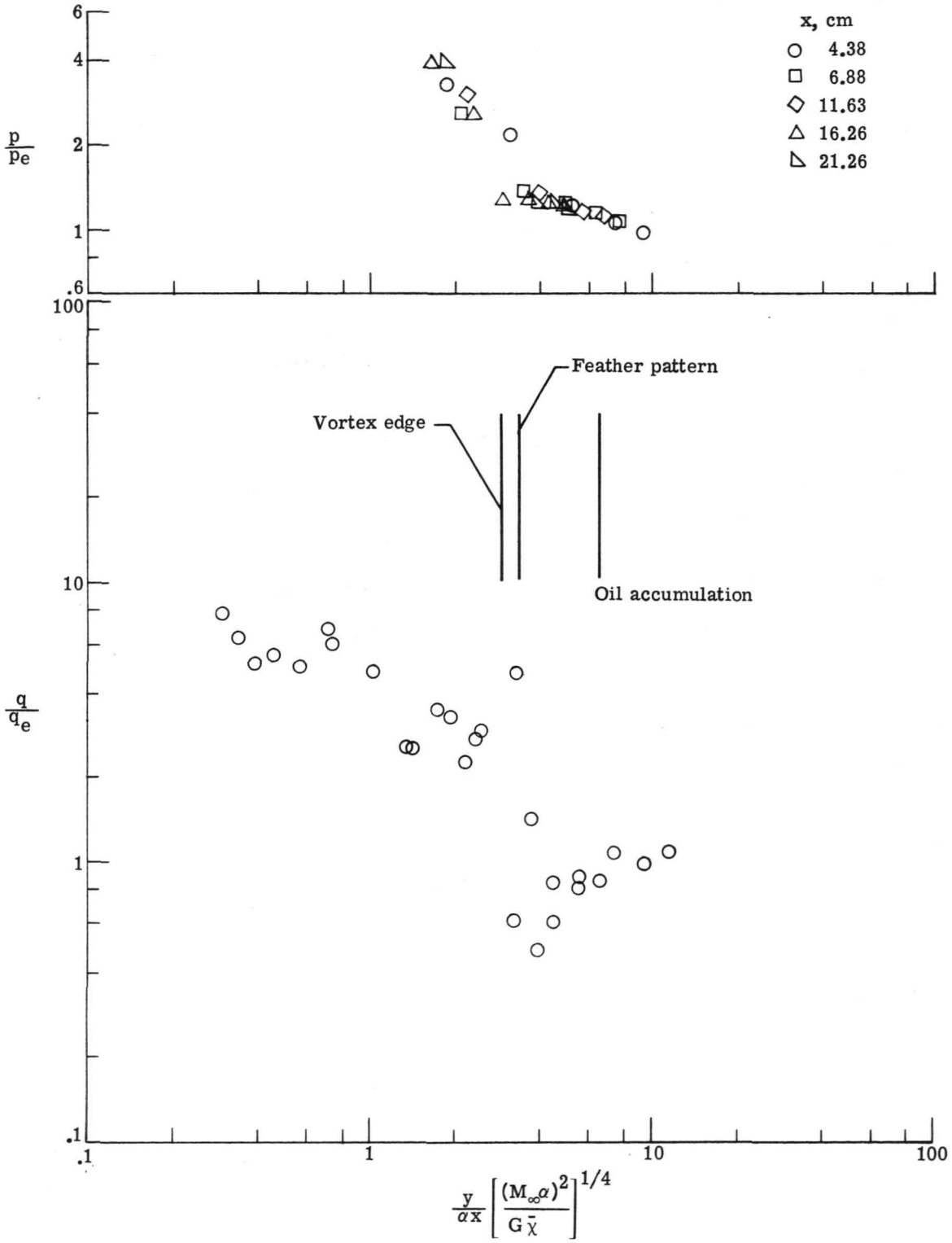

(d) Case 4; $\alpha = 10^{o}$; sharp nose.

Figure 15.- Continued.

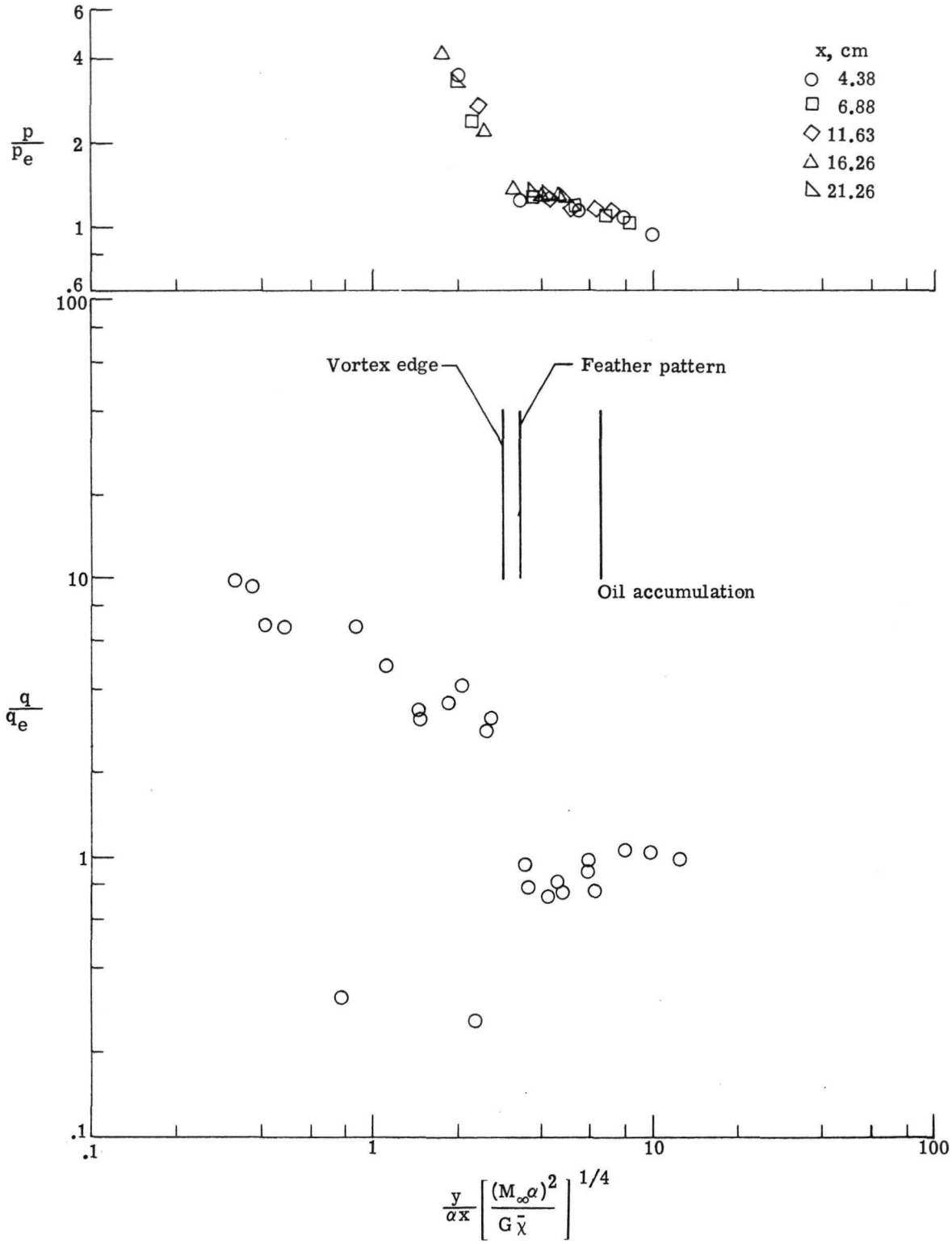

(e) Case 5; $\alpha = 10^{o}$; sharp nose.

Figure 15. - Continued.

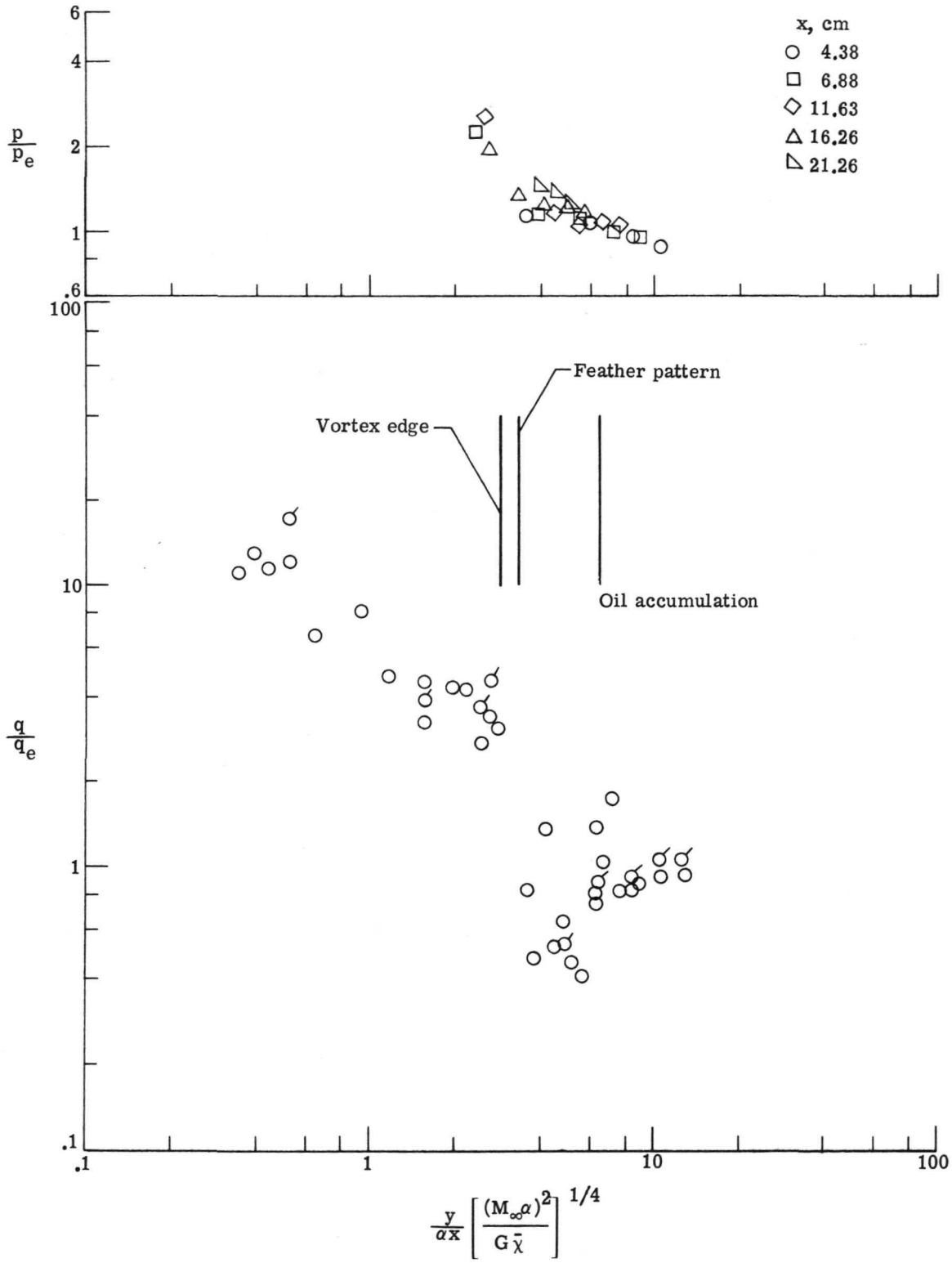

(f) Case 6; $\alpha = 10^{o}$; sharp nose.

Figure 15.- Concluded.

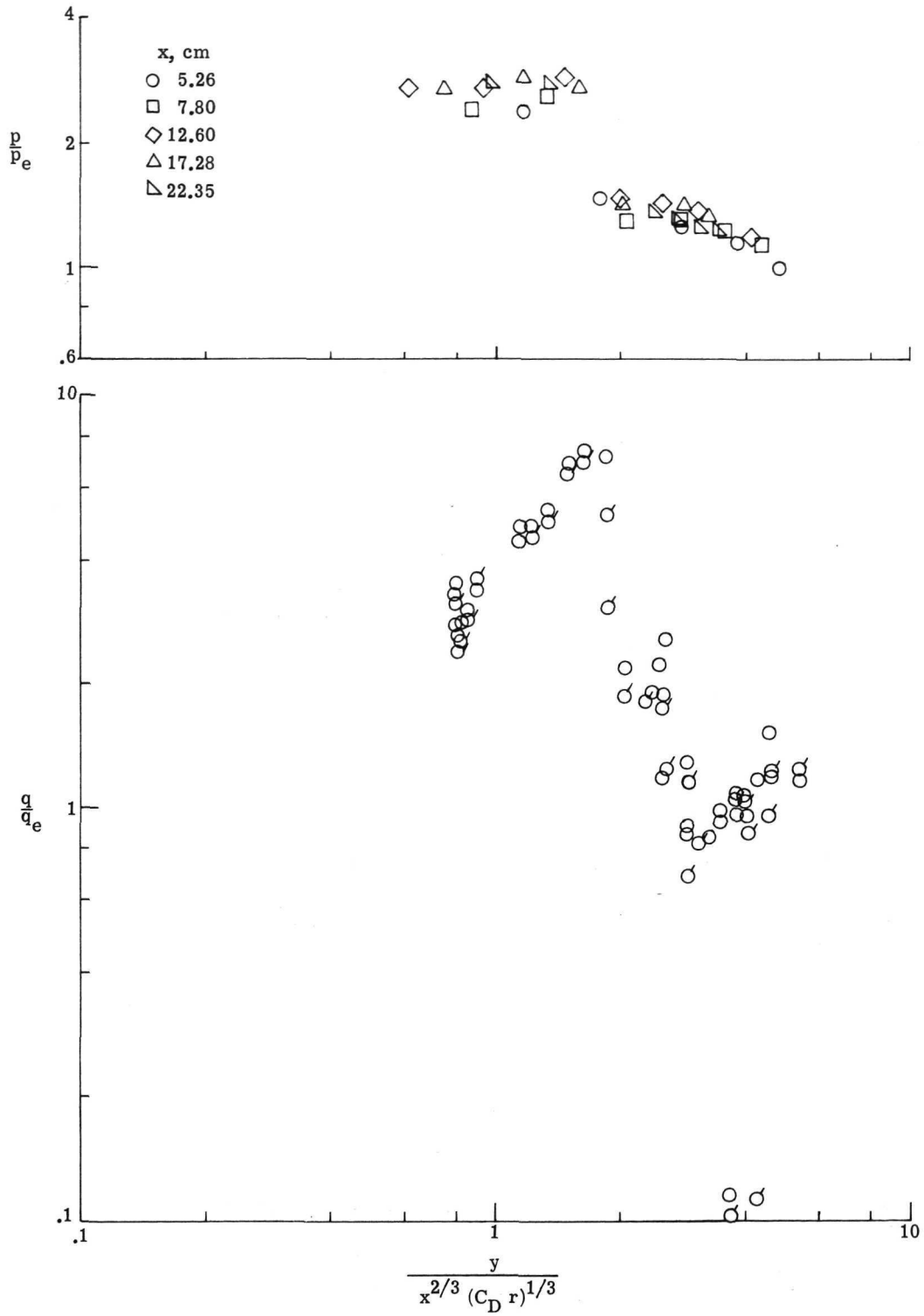

(a) Case 7; $\alpha = 5^{o}$; 20^{o} nose.

Figure 16.- Pressures and heat transfer on blunt-wedge corners. (Flagged symbols denote reruns.)

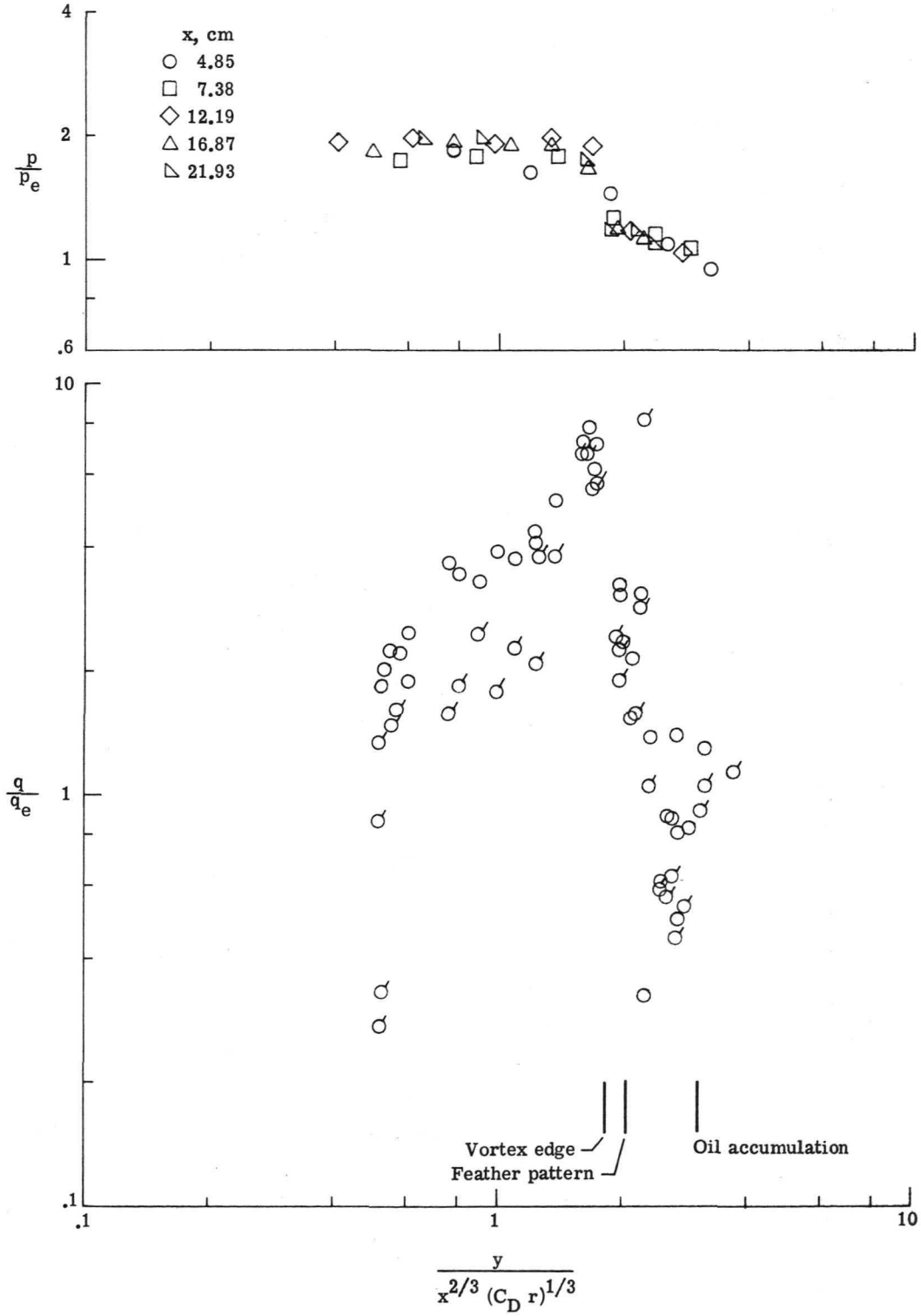

(b) Case 8; $\alpha = 5^{o}$; 36^{o} nose.

Figure 16.- Continued.

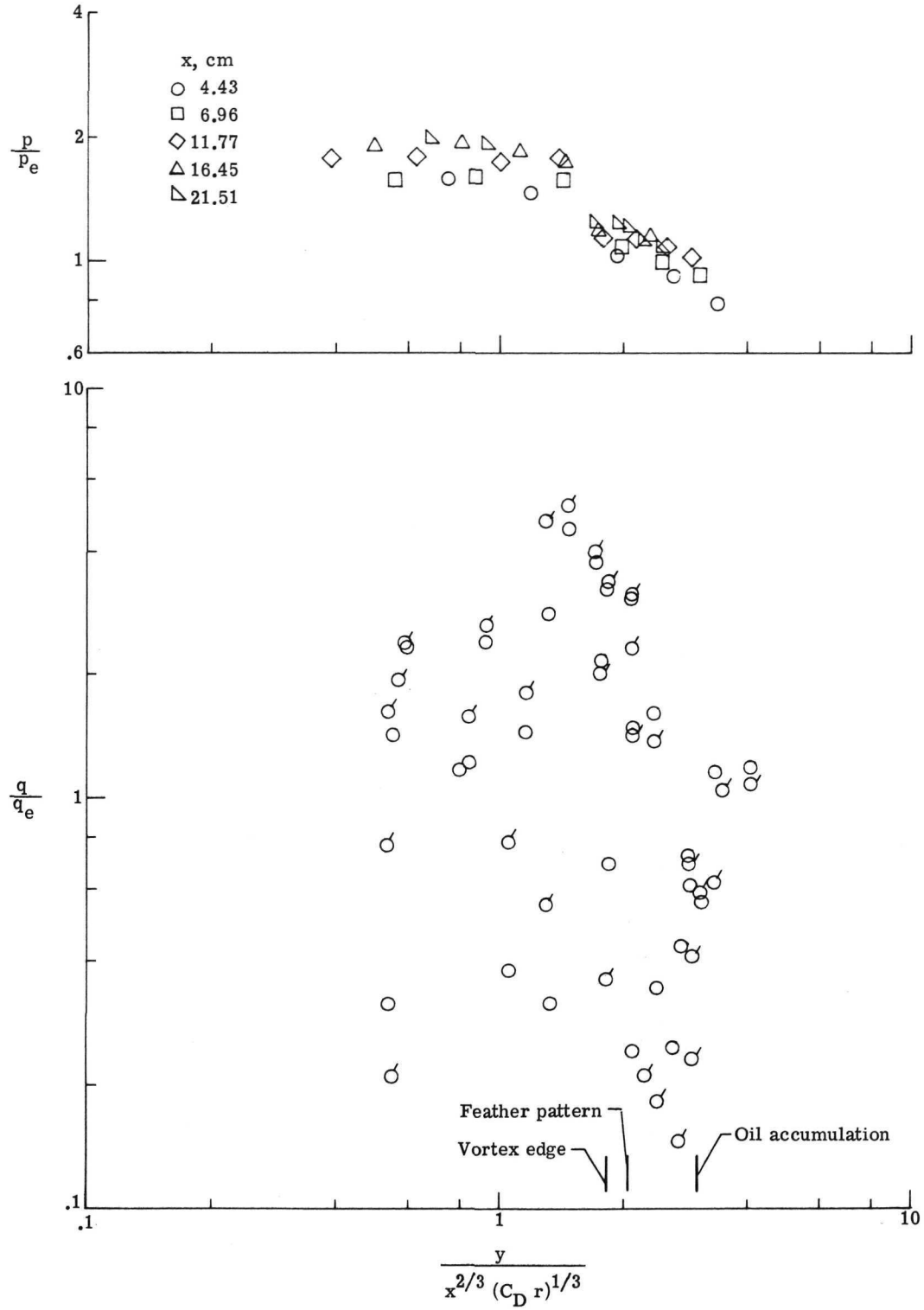

(c) Case 9; $\alpha = 5^{o}$; flat nose; r = 0.15 cm.

Figure 16.- Continued.

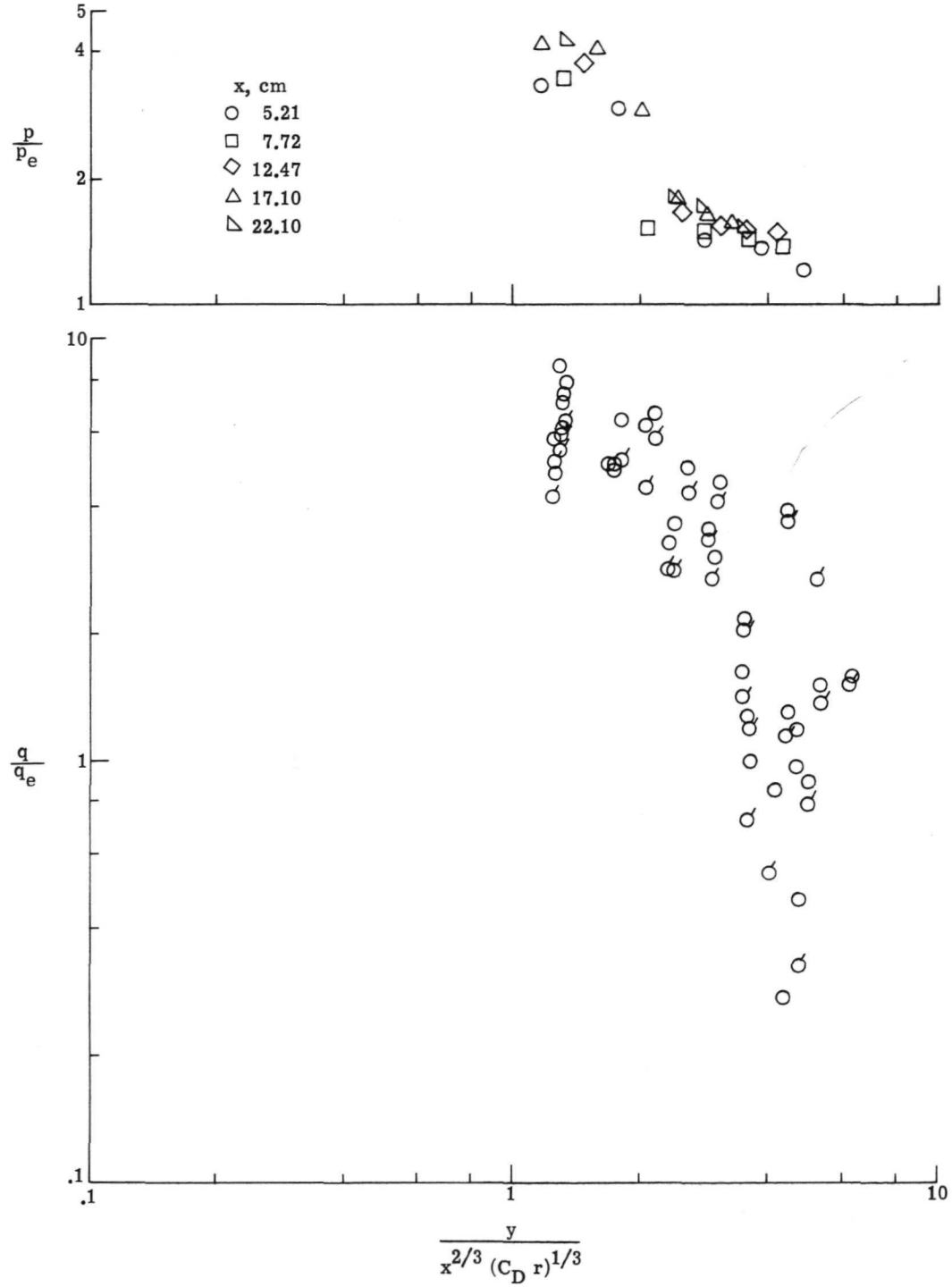

(d) Case 10; $\alpha = 10^{o}$; 20^{o} nose.

Figure 16.- Continued.

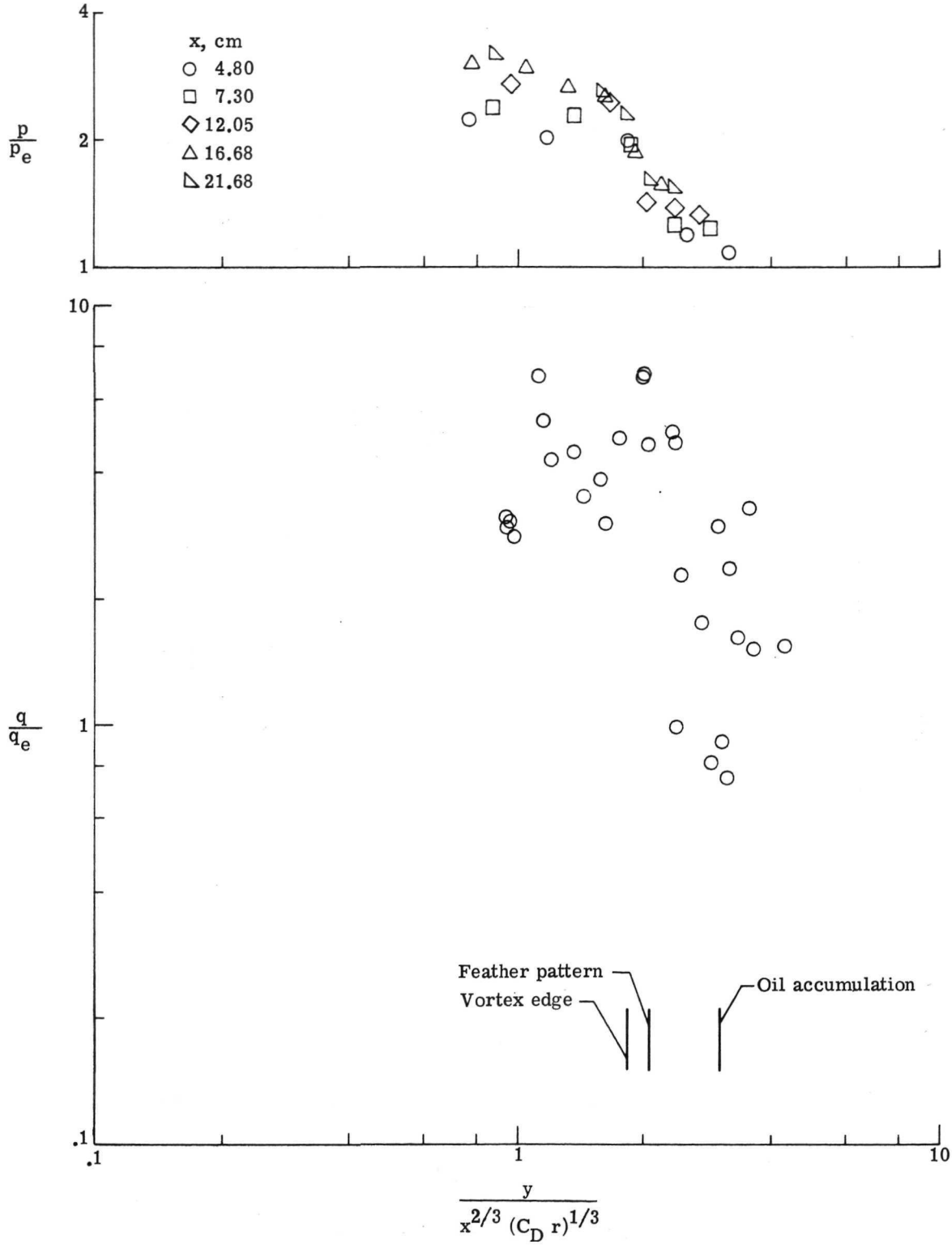

(e) Case 11; $\alpha = 10^{o}$; 36^{o} nose.

Figure 16.- Continued.

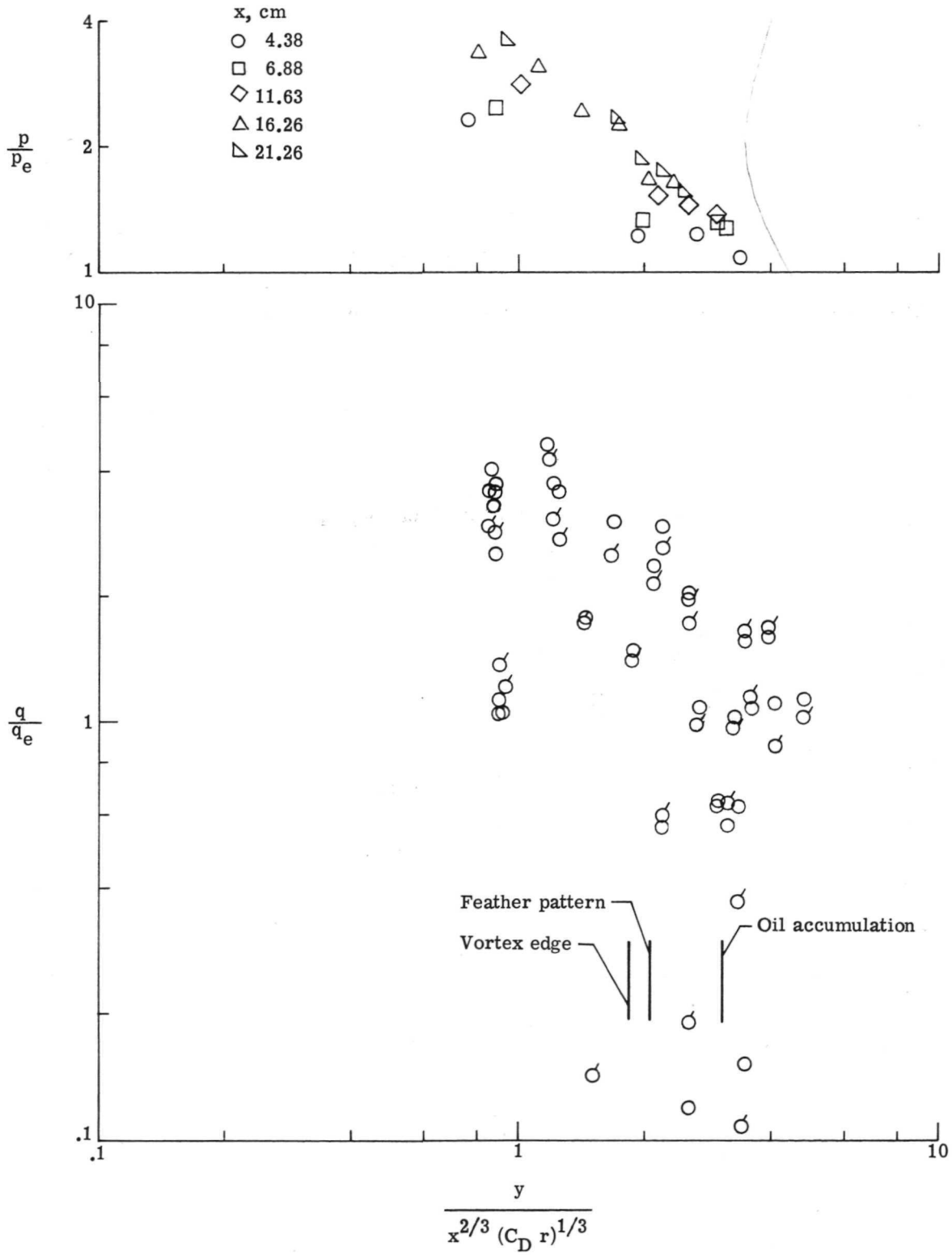

(f) Case 12; $\alpha = 10^{o}$; flat nose; r = 0.15 cm.

Figure 16.- Concluded.

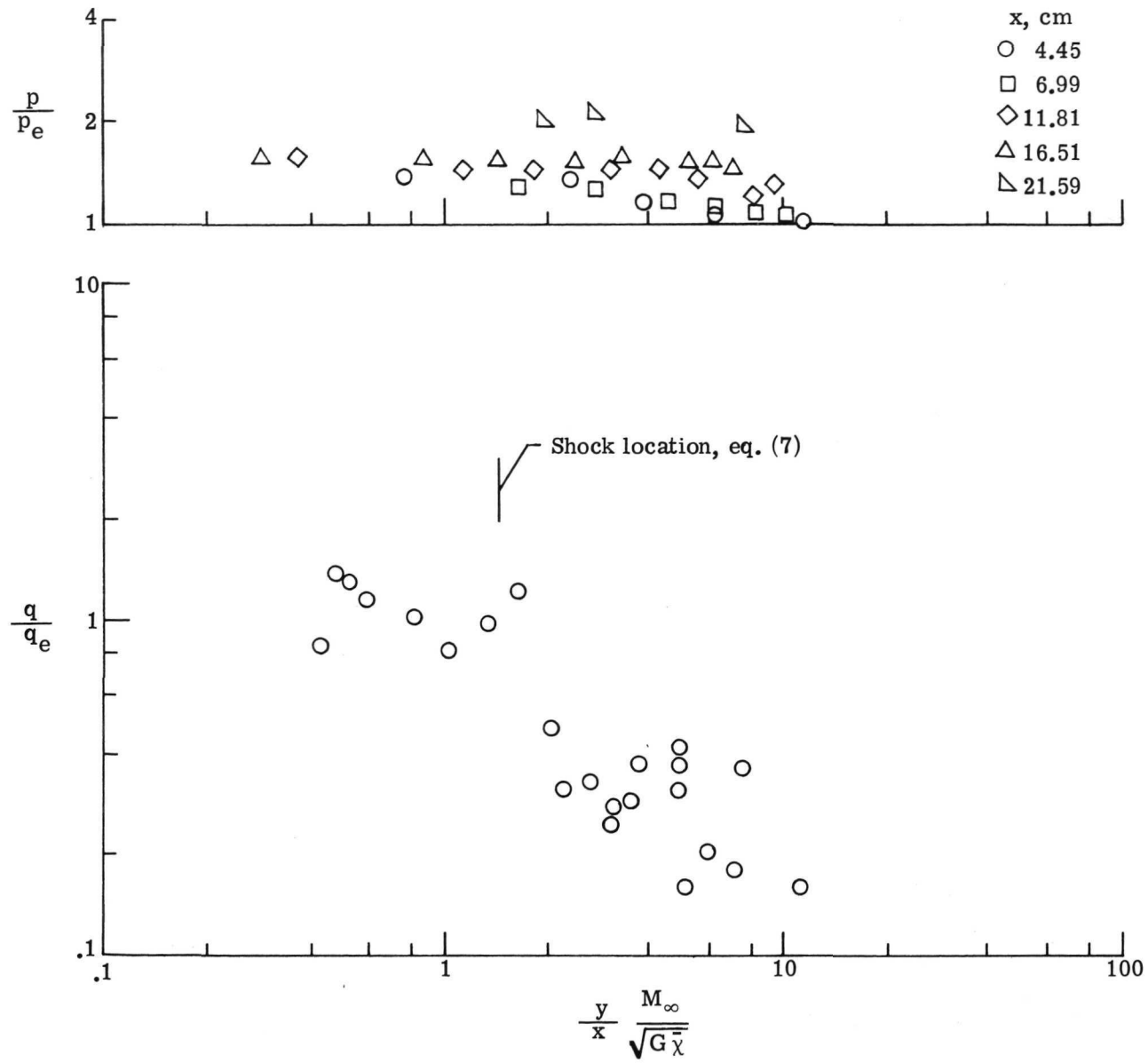

(a) Case 13; $\alpha = 0^{o}$; sharp nose.

Figure 17.- Pressures and heat transfer on sharp-plate corners.

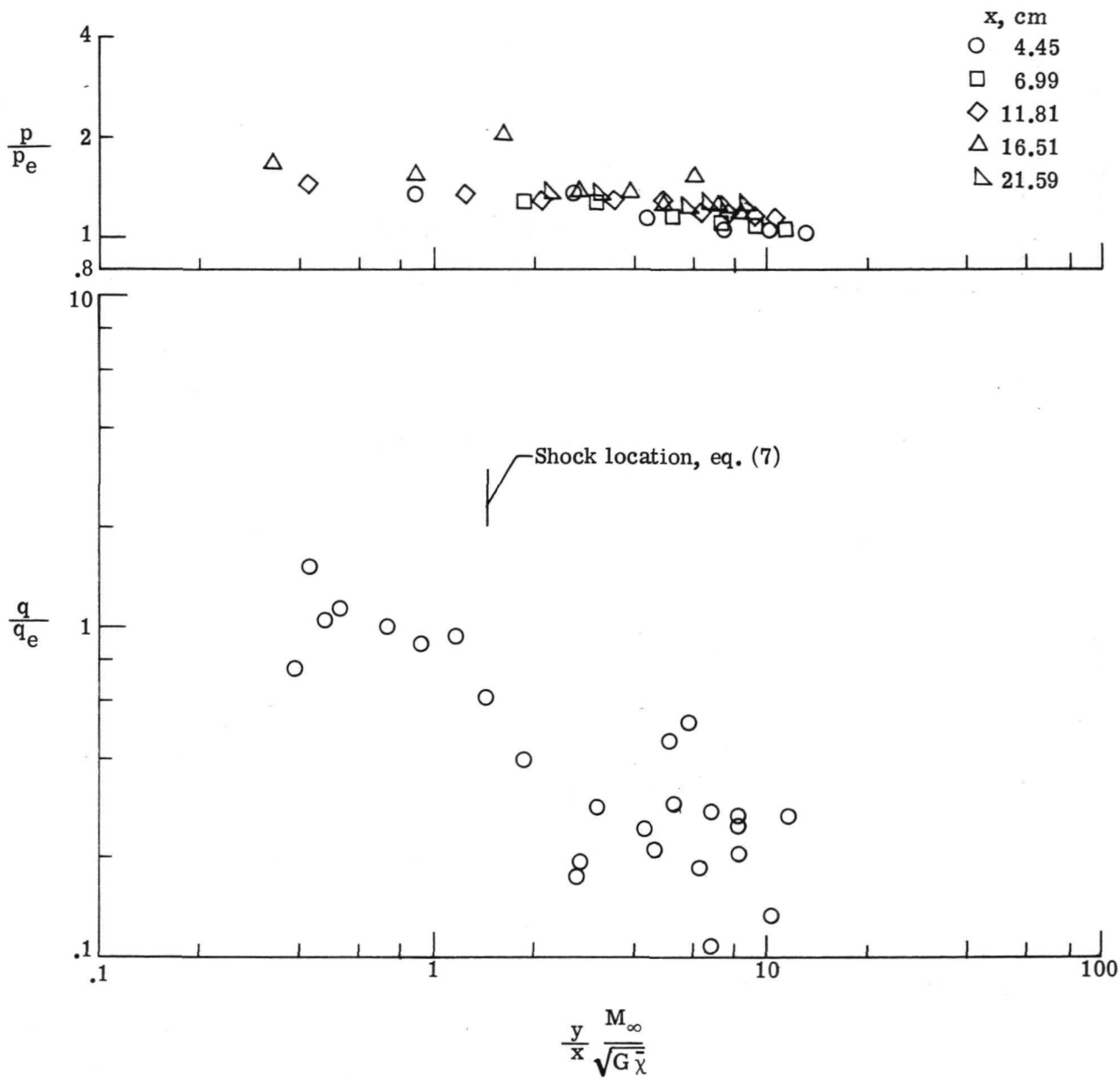

(b) Case 14; $\alpha = 0^{o}$; sharp nose.

Figure 17.- Continued.

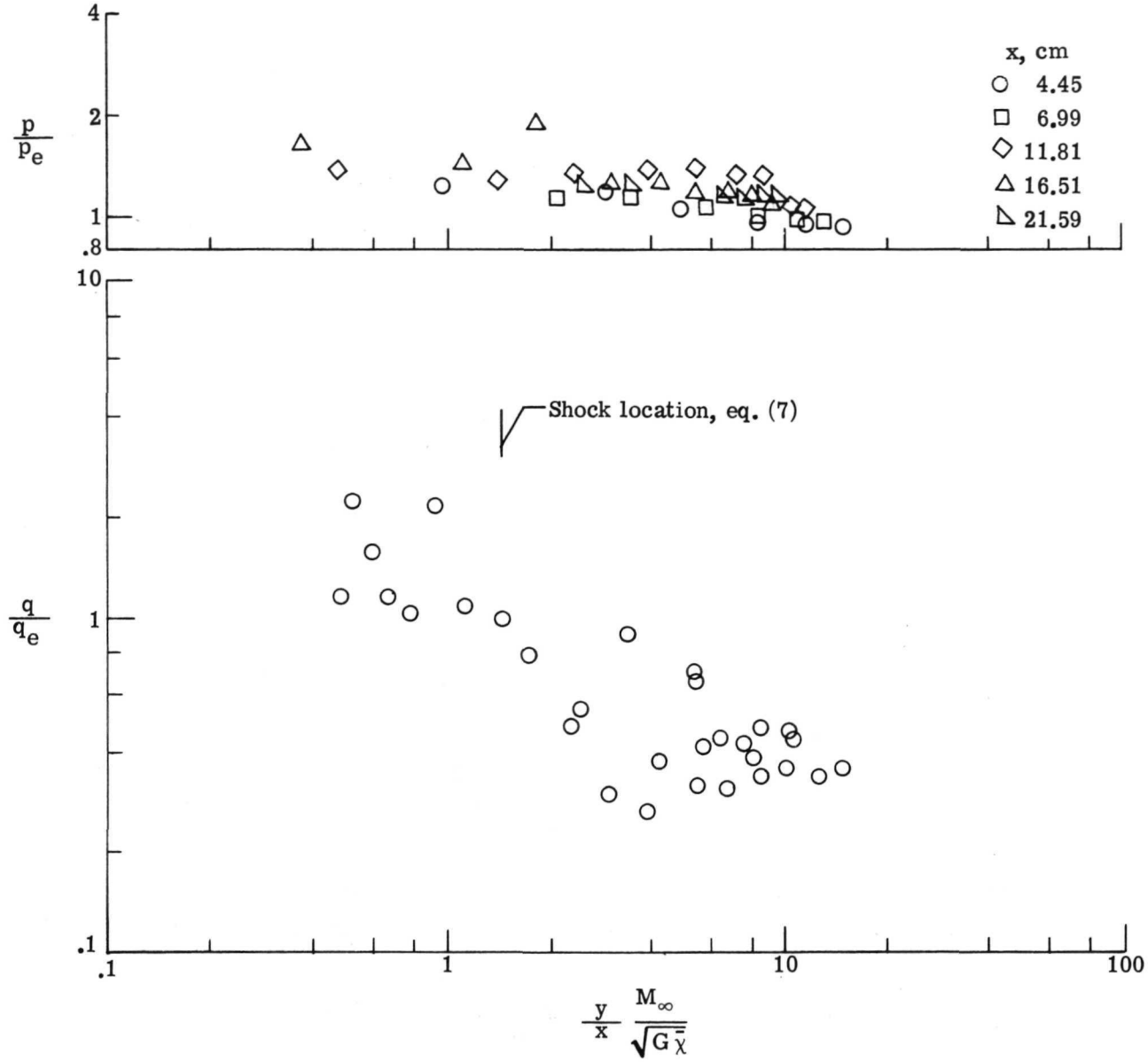

(c) Case 15; $\alpha = 0^{o}$; sharp nose.

Figure 17.- Concluded.

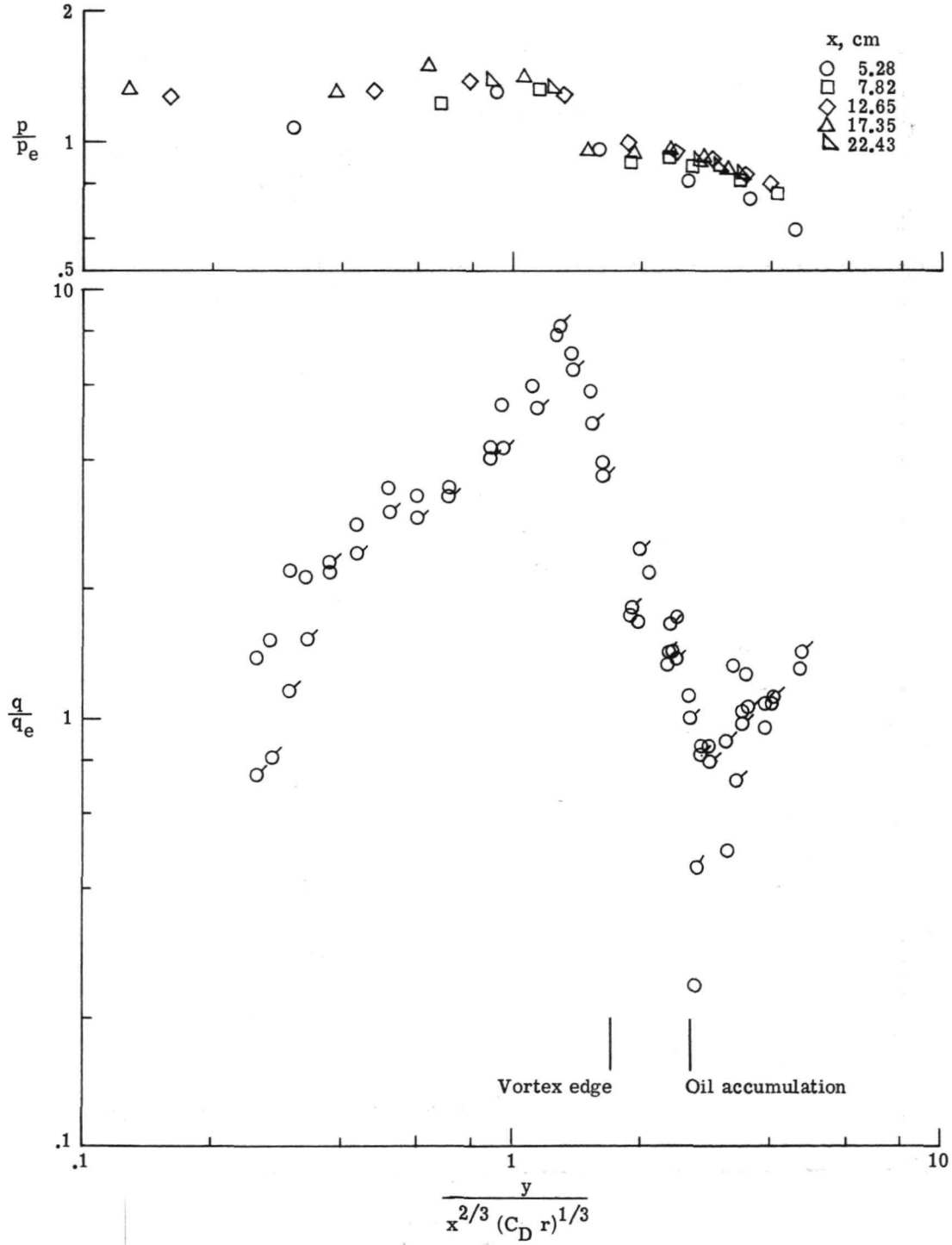

(a) Case 16; $\alpha = 0^{o}$; 20^{o} nose.

Figure 18.- Pressures and heat transfer on blunt-plate corners. (Flagged symbols denote reruns.)

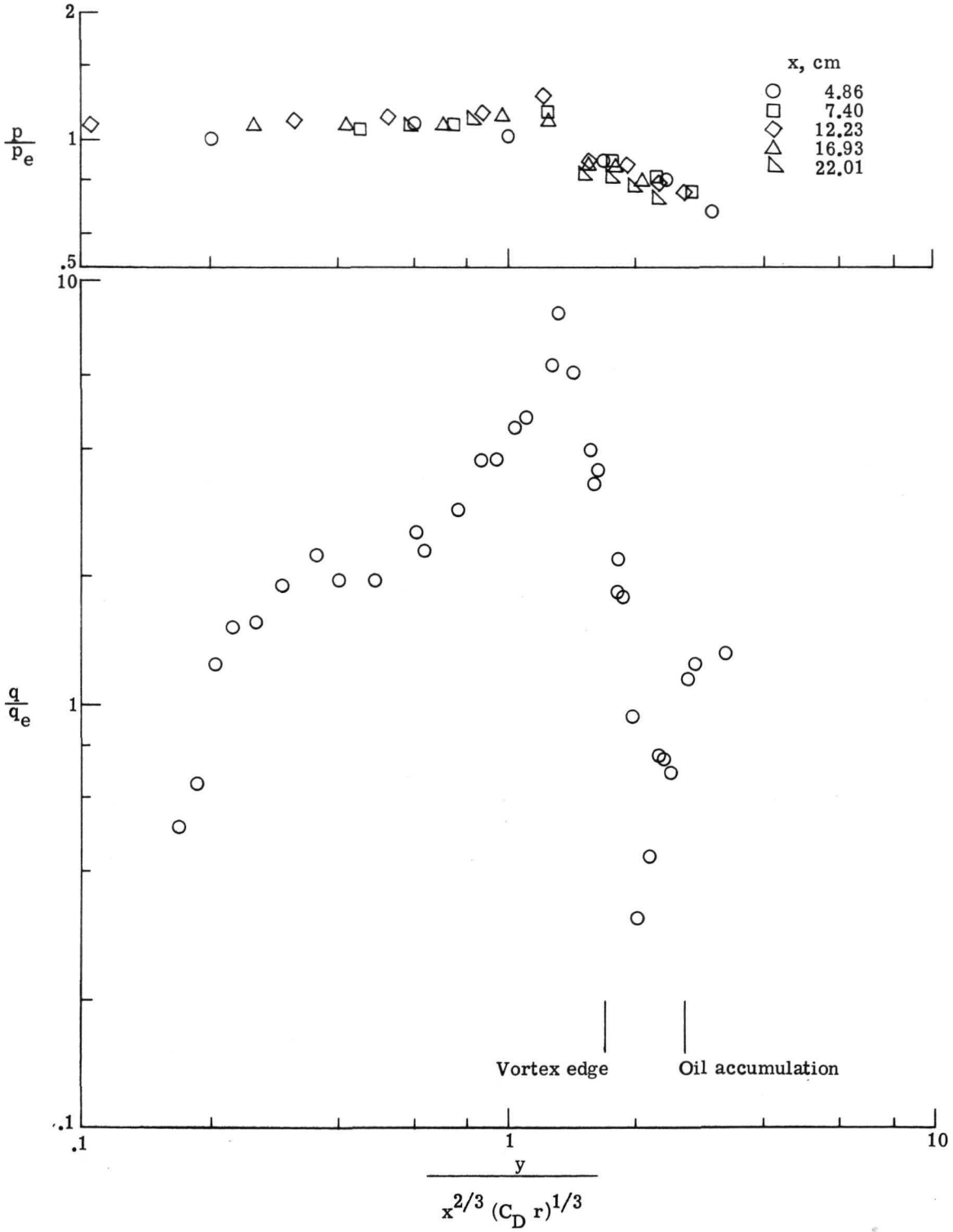

(b) Case 17; $\alpha = 0^{o}$; 36^{o} nose.

Figure 18.- Continued.

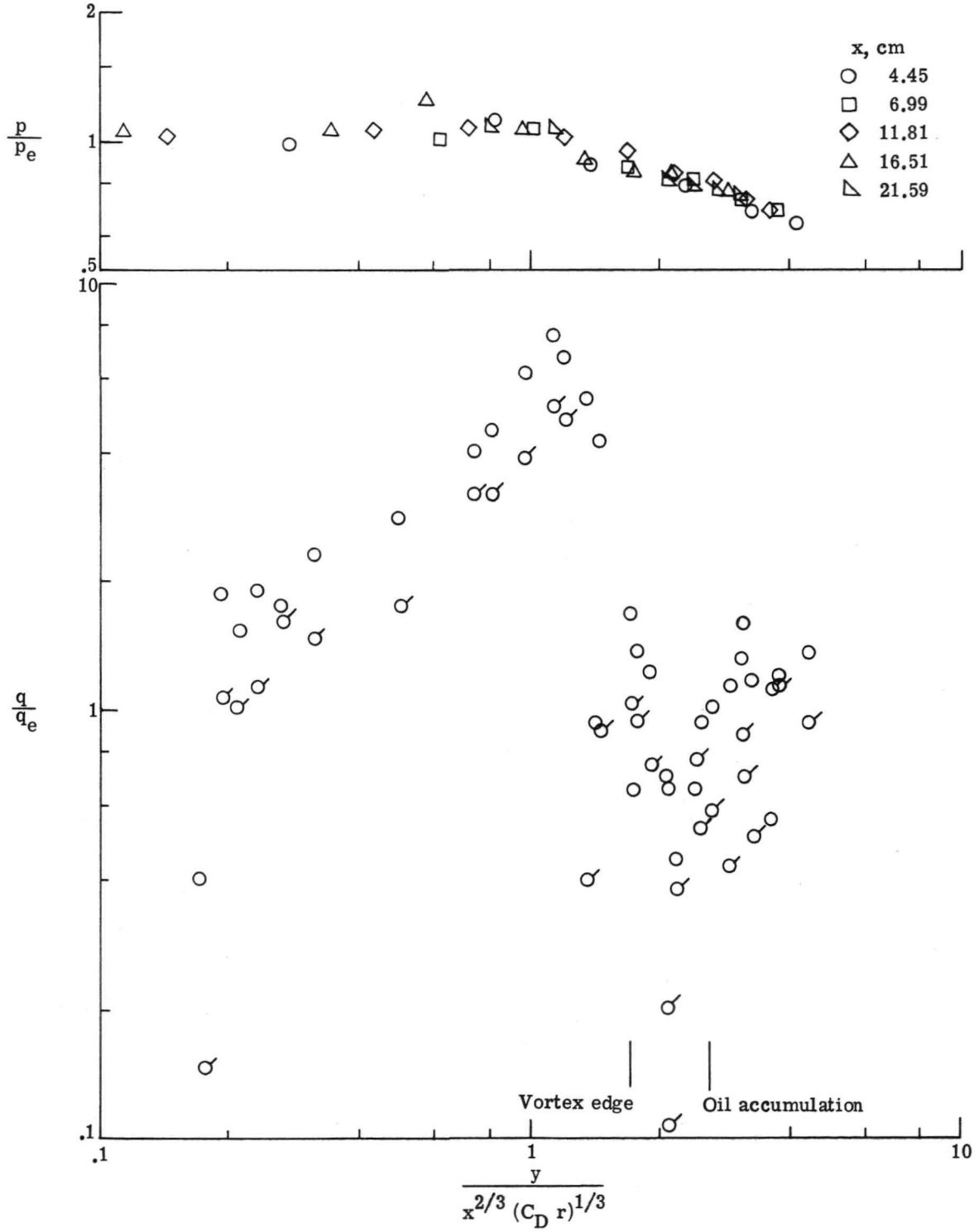

(c) Case 18; $\alpha = 0^{o}$; flat nose; r = 0.08 cm.

Figure 18.- Continued.

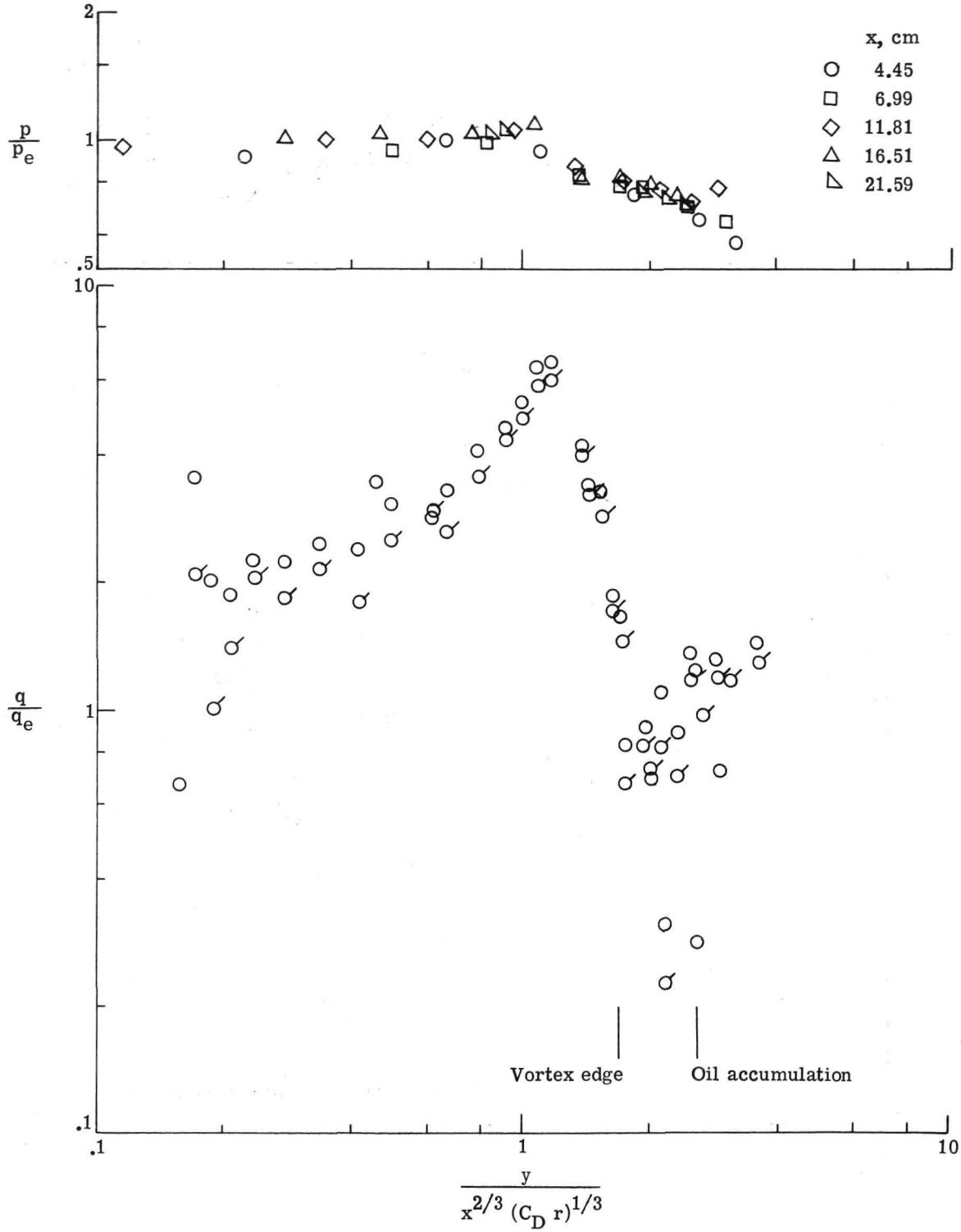

(d) Case 19; $\alpha = 0^{o}$; flat nose; r = 0.15 cm.

Figure 18.- Concluded.

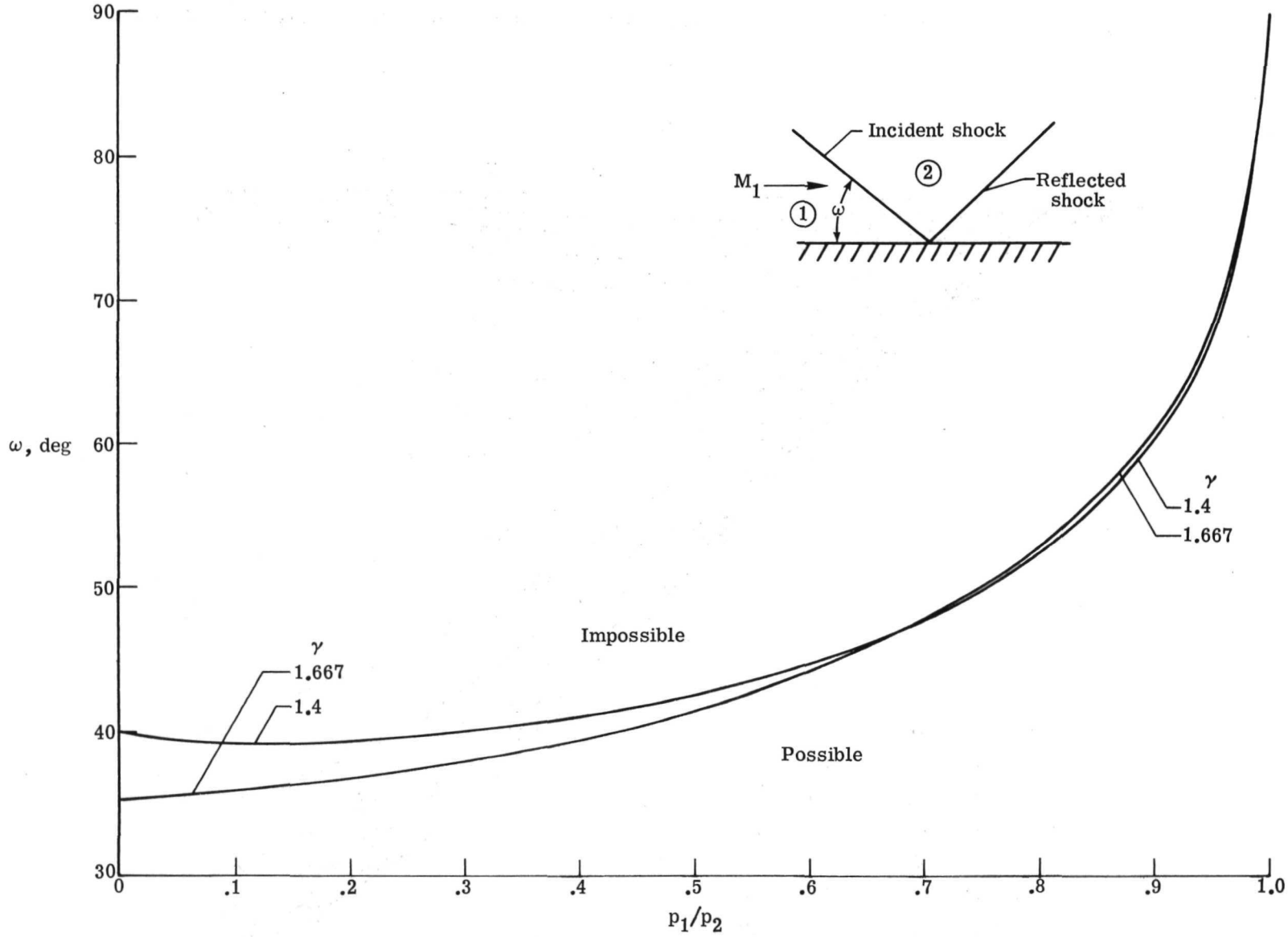

Figure 19.- Incident angle for which reflection is possible as a function of pressure ratio.

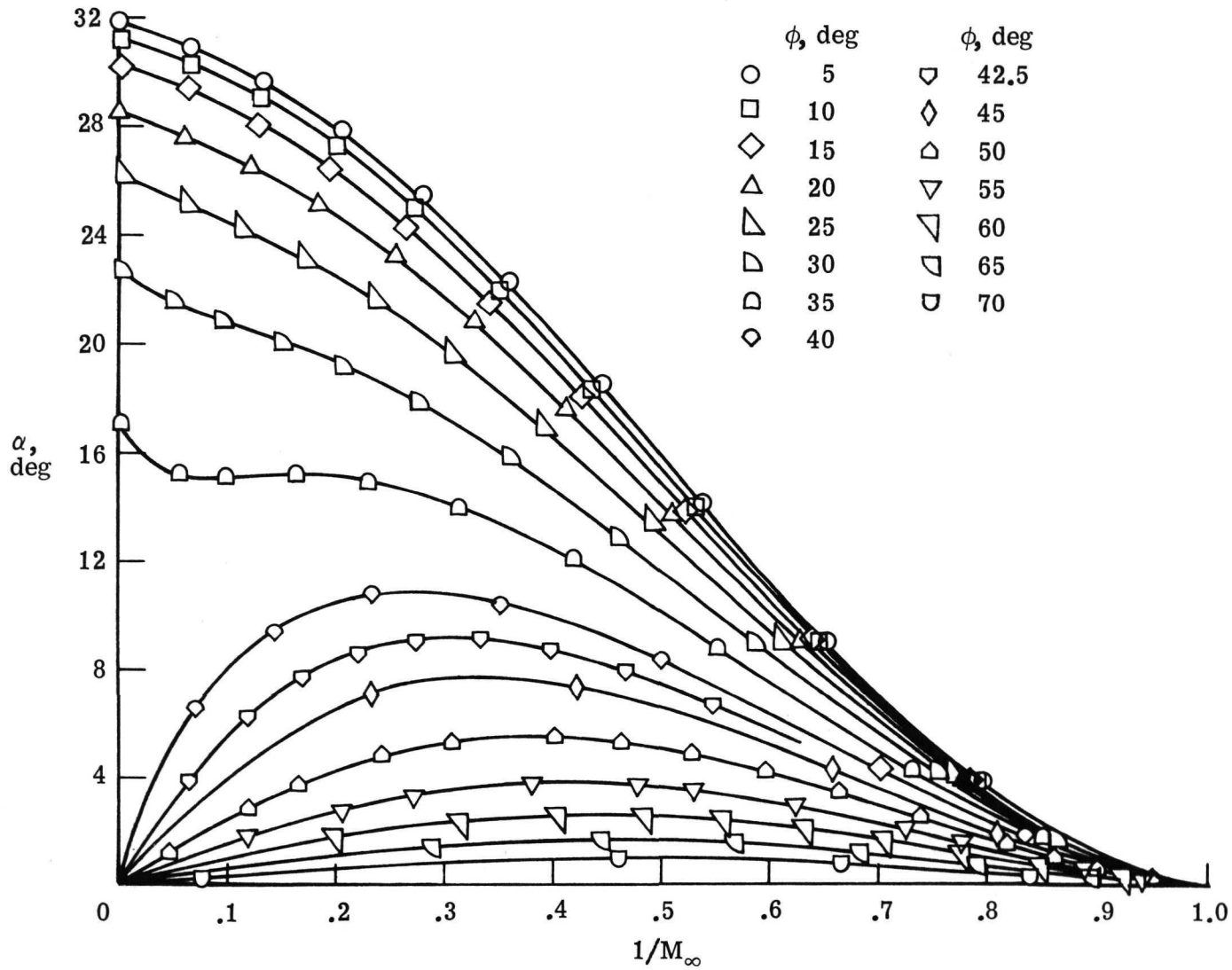

(a) $\gamma = 1.4$.

Figure 20.- Limiting conditions for shock intersection on symmetrical sharp streamwise corners.

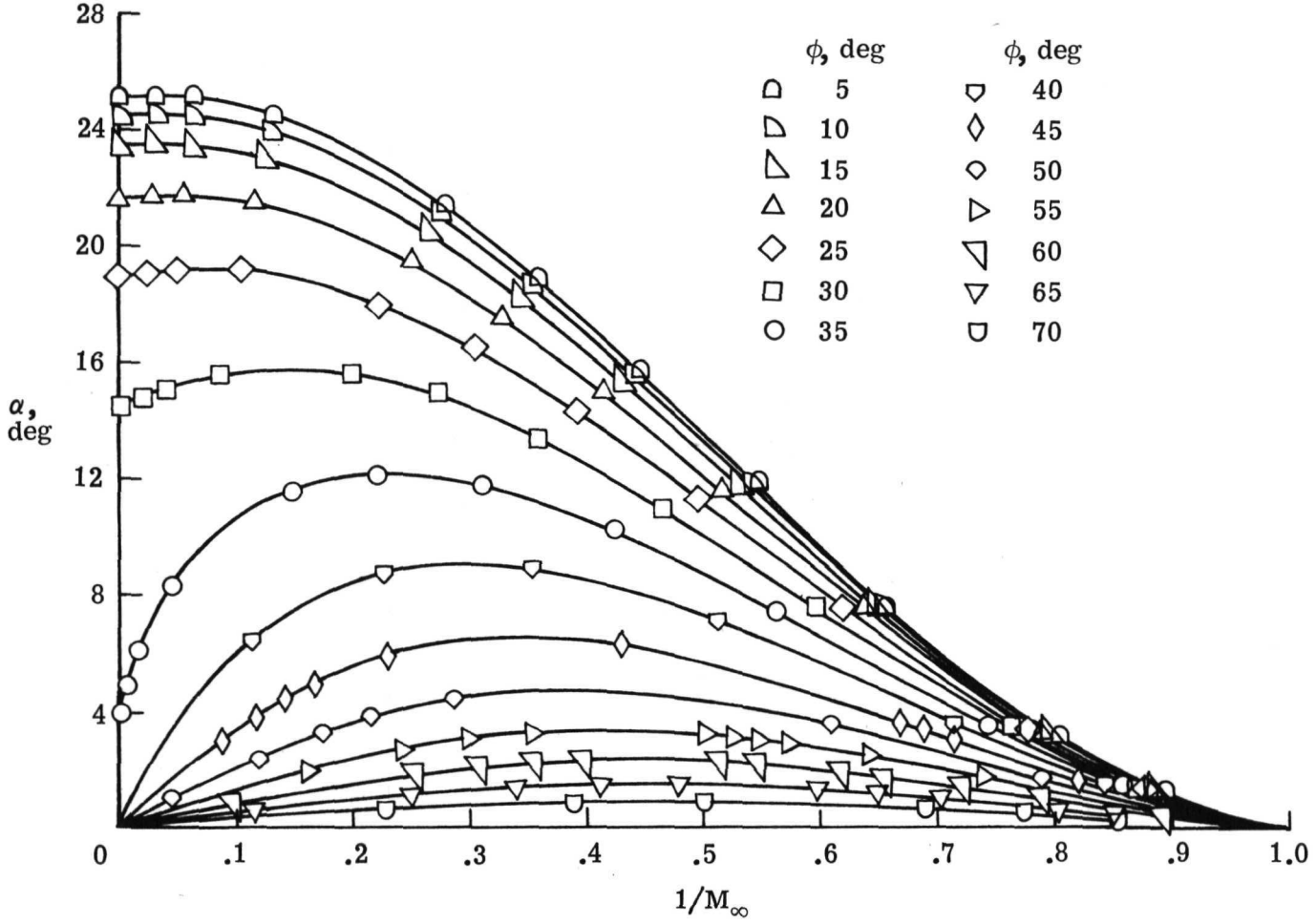

(b) $\gamma = 1.667$.

Figure 20.- Concluded.

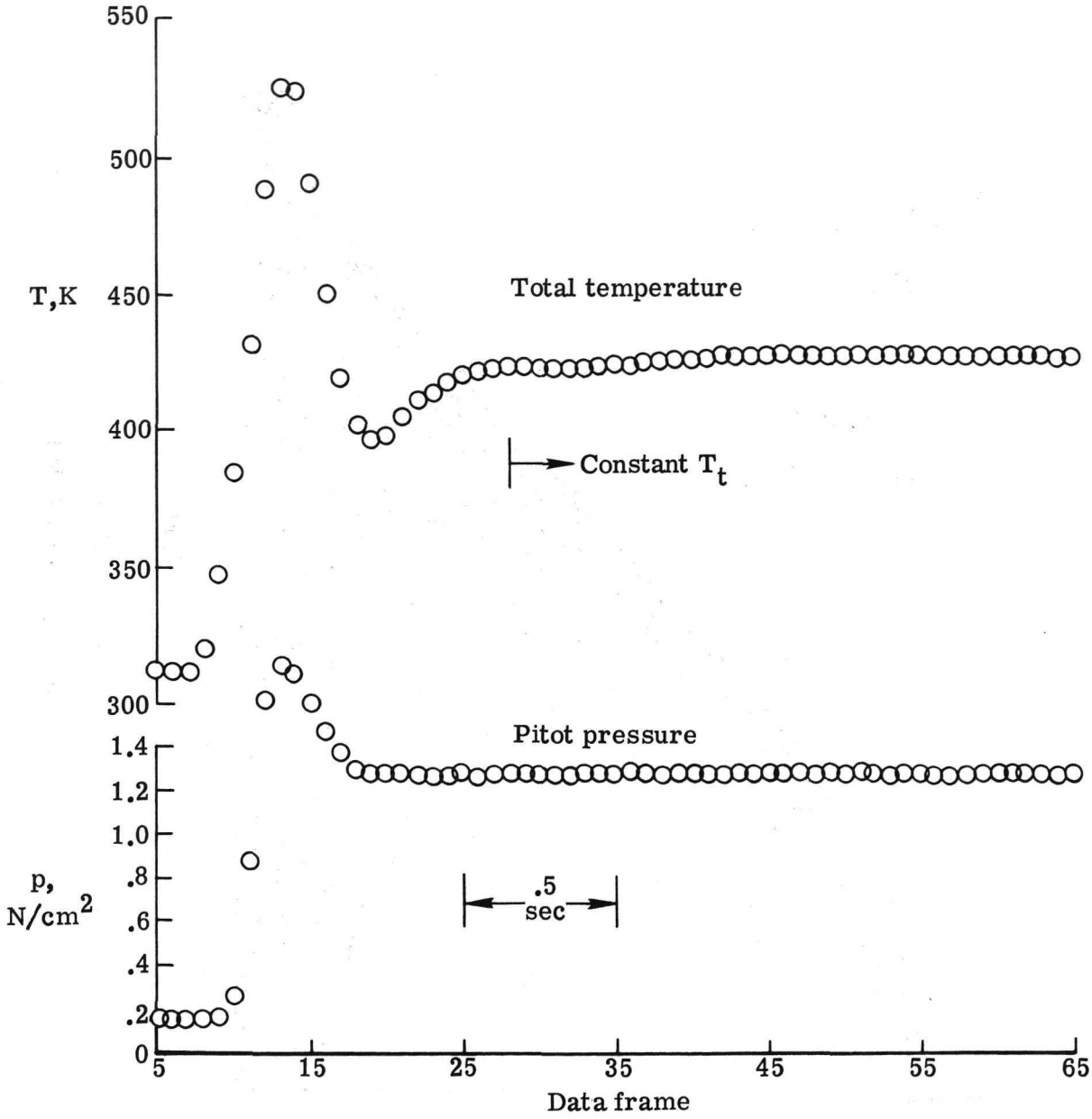

Figure 21.- Starting transients in Langley 22-inch helium tunnel. Test 327, run 5.

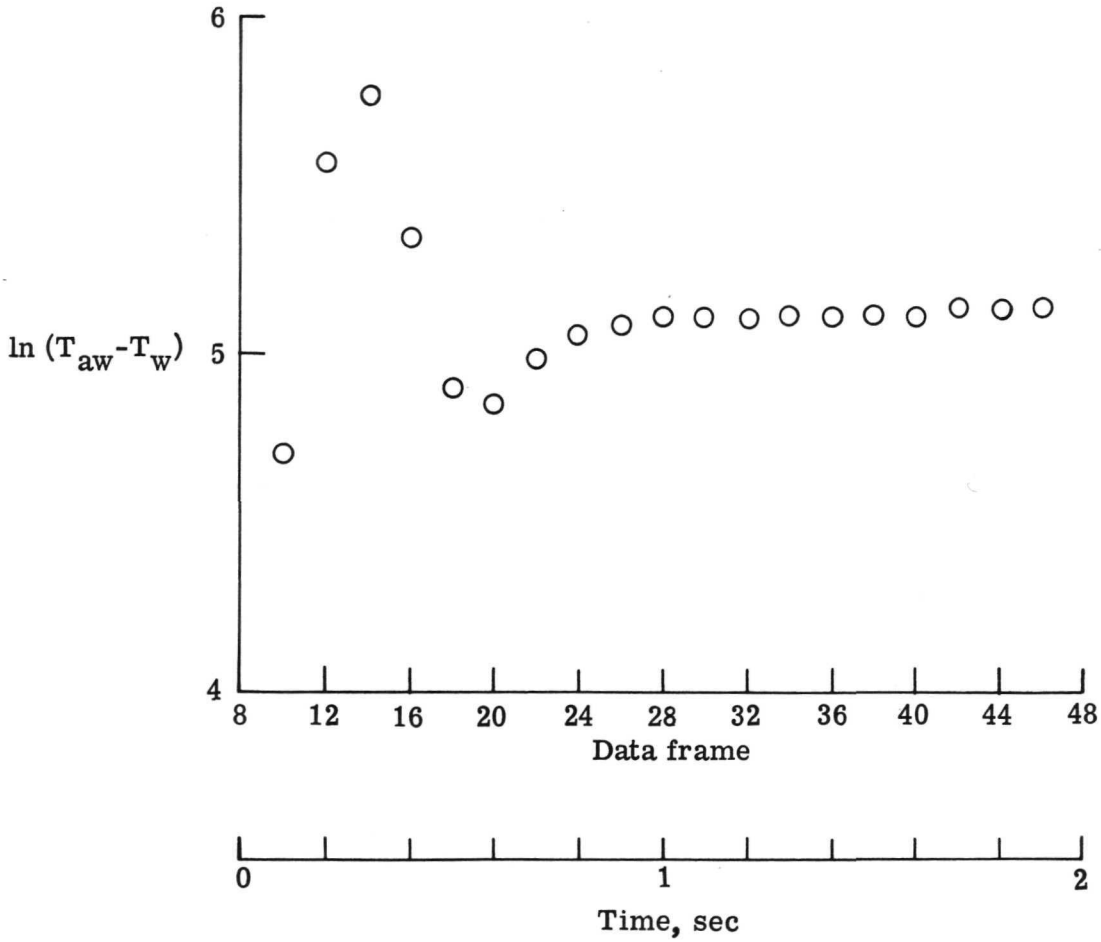

Figure 22.- Typical heat-transfer trace. Test 327, run 5; $\alpha = 0^{o}$; sharp nose.

"The aeronautical and space activities of the United States shall be conducted so as to contribute . . . to the expansion of human knowledge of phenomena in the atmosphere and space. The Administration shall provide for the widest practicable and appropriate dissemination of information concerning its activities and the results thereof."

—NATIONAL AERONAUTICS AND SPACE ACT OF 1958

NASA SCIENTIFIC AND TECHNICAL PUBLICATIONS

TECHNICAL REPORTS: Scientific and technical information considered important, complete, and a lasting contribution to existing knowledge.

TECHNICAL NOTES: Information less broad in scope but nevertheless of importance as a contribution to existing knowledge.

TECHNICAL MEMORANDUMS: Information receiving limited distribution because of preliminary data, security classification, or other reasons. Also includes conference proceedings with either limited or unlimited distribution.

CONTRACTOR REPORTS: Scientific and technical information generated under a NASA contract or grant and considered an important contribution to existing knowledge.

TECHNICAL TRANSLATIONS: Information published in a foreign language considered to merit NASA distribution in English.

SPECIAL PUBLICATIONS: Information derived from or of value to NASA activities. Publications include final reports of major projects, monographs, data compilations, handbooks, sourcebooks, and special bibliographies.

TECHNOLOGY UTILIZATION PUBLICATIONS: Information on technology used by NASA that may be of particular interest in commercial and other non-aerospace applications. Publications include Tech Briefs, Technology Utilization Reports and Technology Surveys.

Details on the availability of these publications may be obtained from:

SCIENTIFIC AND TECHNICAL INFORMATION OFFICE

NATIONAL AERONAUTICS AND SPACE ADMINISTRATION

Washington, D.C. 20546